A search for $\mathbf{ZH} \rightarrow \boldsymbol{\mu\mu}\mathrm{b}\bar{\mathrm{b}}$ production at the Tevatron

A search for $\mathbf{ZH \rightarrow \mu\mu b\bar{b}}$ production at the Tevatron

Een wetenschappelijke proeve op het gebied van
Natuurwetenschappen, Wiskunde en Informatica

Proefschrift

ter verkrijging van de graad van doctor
aan de Radboud Universiteit Nijmegen
op gezag van de rector magnificus prof. mr. S.C.J.J. Kortmann,
volgens besluit van het College van Decanen
in het openbaar te verdedigen op dinsdag 20 april 2010
om 10.30 uur precies

door

Lucian-Ştefan Ancu

geboren op 26 december 1981
te Târgu Secuiesc (Roemenië)

Promotor:	Prof. dr. S. J. de Jong	
Copromotor:	Dr. F. Filthaut	
Manuscriptcommissie:	Prof. dr. D. Froidevaux	
	Prof. dr. N. de Groot	Radboud Universiteit
	Prof. dr. E. Laenen	Nikhef/Universiteit van Amsterdam/ Utrecht Universiteit
	Dr. M. Kirby	Northwestern University
	Dr. I. van Vulpen	Universiteit van Amsterdam/Nikhef

ISBN: 978-90-9025258-2

Cover designed by: Ideeal communicatie, Apeldoorn. Concept and front cover photograph by Lucian-Ştefan Ancu.

The work described in this thesis is part of the research program of the National Institute for Subatomic Physics (Nikhef) in Amsterdam, the Netherlands. The author was financially supported by the Foundation for Fundamental Research on Matter (FOM).

Contents

Introduction **9**

1 Theory **11**
1.1 The Standard Model 11
1.2 Higgs mechanism 16
1.3 Direct and indirect constraints on the Higgs mass 19
1.3.1 Constraints from theory 19
1.3.2 Experimental constraints 20
1.4 Higgs production at the Tevatron 23

2 The Tevatron and the DØ detector **27**
2.1 The Tevatron 27
2.1.1 Luminosity and beam lifetime 30
2.2 The DØ detector 32
2.2.1 Detector coordinate system 33
2.2.2 Central tracking detectors 34
2.2.3 Calorimetry 39
2.2.4 Muon system 42
2.2.5 Luminosity monitor 45
2.2.6 Trigger and DAQ 47

3 Object identification **53**
3.1 Muons 53
3.1.1 Efficiency 55
3.1.2 Muon momentum smearing 55
3.2 Jets 56
3.2.1 Jet finding algorithm 56
3.2.2 Noise reduction 58
3.2.3 Jet identification 58
3.2.4 Jet energy scale 58
3.2.5 Jet energy resolution 60

3.2.6 Shifting, smearing and removing of simulated jets - JSSR . . 60
3.3 Missing E_T . . . 62
3.4 Tracks . . . 62
3.5 Primary Vertices . . . 62
3.6 B-tagging . . . 63

4 Event Selection 67
4.1 Data . . . 67
4.2 Monte Carlo . . . 67
4.3 Event selection . . . 68
4.4 Corrections to MC . . . 71
4.4.1 Z+jets cross section . . . 71
4.4.2 Luminosity reweighting . . . 73
4.4.3 Primary vertex reweighting . . . 73
4.4.4 Z p_T reweighting . . . 73
4.4.5 Jet corrections . . . 74
4.5 Multijet background . . . 74
4.6 Specific reweightings . . . 76
4.6.1 Trigger modeling . . . 76
4.6.2 Leading jets $\Delta\phi$ reweighting . . . 77
4.7 B-tagging . . . 78

5 Analysis 81
5.1 Kinematic fit . . . 81
5.2 Spin related variables . . . 83
5.3 Boosted decision trees . . . 84
5.3.1 Why use decision trees . . . 84
5.3.2 What are decision trees . . . 84
5.3.3 Training . . . 85
5.3.4 Pruning . . . 86
5.3.5 Boosting . . . 87
5.3.6 Implementation of BDTs for the search . . . 88

6 Limits on Higgs production 101
6.1 Limit setting procedure . . . 101
6.2 Systematics . . . 103
6.2.1 Scale systematics . . . 104
6.2.2 Shape systematics . . . 104
6.3 Results . . . 107

7 Conclusions and outlook 111

Bibliography **115**

Summary **123**

Samenvatting **125**

Acknowledgements **129**

Curriculum vitae **131**

Introduction

The history of smashing things together starts, maybe, with the discovery of seeds inside of nuts. The idea of "inside" and finding the hidden structure of things has to be as old as this culinary habit. At first, the ancestor of man was using as a smashing tool whatever hard object he could find around. It had to be at least as hard as the nut he was going for and probably that was the time of the realization that the result of a collision depends on the objects collided. When realizing that the results of these collisions can be used with the purpose of making better tools, the first stone hammers were made. And the rest can be considered history.

The happiness of "cracking a case" has been part of our daily life for centuries. The curiosity of finding what is within the shell is also one of the driving forces of the mankind. Proof of the importance of the shell and curiosity for what it is inside the shell is most easily seen when considering the process of giving a present. The biggest present, that we all humans share, is the nature around us. The start of understanding the nature is having an theoretical model, i.e. how we think that it works. The second important factor is our ability to test that nature works the way we imagined it to do.

The first theory on the structure of matter seems to be the atomistic theory developed by Leucippus and Democritus in the 5th Century BC. It considered that the world is composed of two different substances: atoms and void. Atoms mean things that cannot be cut into smaller pieces, they represent the point up to which cracking can be done. And this meant that the idea of making sure that something is an atom (or elementary as we name it today) would develop into a race of "cracking" things into smaller and smaller pieces. One interesting idea of that time is that the sensations produced in organisms are due to the scatterings and packing of the atoms in the void.

Later the Greeks thought that all objects are made from the combination of air, water, fire and earth. At that time, this was not the only theory on the market as the Chinese thought that there is an extra element: metal. But the principle of everything in the world being made out of combinations of elements was present in both cultures. It is interesting to note that, in this later theory, the elements are considered to have a continuous structure. This second theory actually was

considered the right one for many years.

The quest for understanding the sub-structure of matter continued through ages and through successive experiments the current view of matter was reached. Today we consider matter to be constructed from quarks and leptons and the interactions between these particles are mediated by boson particles. A detailed description of the quantum field theory developed to describe the interaction of these particles, the so called Standard Model, is given in Chapter 1. However one piece of the Standard Model is not yet discovered, the Higgs boson. It plays a key role in explaining the origin of mass of other elementary particles. If no Higgs particle exists then other particles and forces are necessary to explain our current knowledge of elementary particles.

Even if the Standard Model predicts that a Higgs boson should exist, no exact prediction on the mass of the Higgs boson is made. Direct limits have been set on the Higgs mass by experiments at the LEP and Tevatron colliders, but a large region of possible Higgs masses is not ruled out. In Chapter 1 general considerations on the topic of Higgs physics are described. Two of the promising search channels at the Tevatron are the ones in which the Higgs boson is produced together with a W or Z boson. For this thesis the choice was made to search the Higgs boson in associated production with a Z boson decaying into two muons. The clean signature of the Z boson combined with the signature of the Higgs decay make this channel one of the best search channels for the Higgs at DØ detector and at the Tevatron.

The DØ detector records collisions of protons and anti-protons produced by the Tevatron accelerator. The Tevatron has been running since 1985 producing collisions first at a lower center of mass energy of 1.8 TeV and at the beginning only one detector was present, namely CDF. In 1992 the DØ detector was commissioned and this marks the start of the run period that is known as RunI. Then in 2001, after upgrades to the detectors and accelerators, starts what is known as RunII at a higher center of mass energy of 1.96 TeV. RunII is split into two periods a and b; the end of RunIIa and beginning RunIIb is marked at DØ by the upgrade of the detector in the year 2005. The DØ detector and the Tevatron accelerator are described in Chapter 2.

Chapter 3 describes the reconstruction algorithms that are used to transform the raw recorded by the detector into physics objects that later are used to characterize the collisions. Chapters 4 to 5 detail the search for the Higgs particle in the ZH channel where the Z decays into two muons. In Chapter 6 the results of the search are presented and Chapter 7 presents a discussion of the results.

Chapter 1

Theory

1.1 The Standard Model

The Standard Model (SM) is the theory of the electromagnetic, weak and strong interactions. At the base of the Standard Model stands the principle of symmetry invariance. By symmetry invariance it is understood that the action of a theory does not change under a symmetry transformation. One of the key concepts in the SM is the concept of local symmetry and, as a consequence, gauge theories are central to the model. In contrast to general symmetry invariance, where the same symmetry transformation holds in every space-time point, in local invariance the transformation is space-time point dependent. The particles are viewed in the theory as excitations of a quantum field. Imposing that the action that describes the particle is invariant under a symmetry transformation gives a conserved quantity under Noether's theorem [1]. To restore the invariance of the Lagrangian, which is broken by the introduction of local symmetry transformation, gauge fields are added. These fields are the source of the force carriers.

The SM is based on the gauge group $SU(3)_C \otimes SU(2)_L \otimes U(1)_Y$. The SM has two sectors: Quantum Chromodynamics (QCD) described by the $SU(3)_C$ gauge symmetry, and the Electroweak sector (EW) described by the $SU(2)_L \otimes U(1)_Y$ gauge group.

Matter particles are described by theory as spin $\frac{1}{2}$ fermions. To every matter particle corresponds an antiparticle, an anti-fermion, having the same mass as the particle but differing from its counterpart by having opposite sign quantum numbers. The interaction between these particles is mediated via force carriers which are spin 1 gauge bosons. All particles of the SM are listed in Table 1.1 and the force carriers in Table 1.2 .

To illustrate the ideas described above we are going to sketch the building of the Quantum Electrodynamics (QED) Lagrangian. (A detailed description can be

	Generation			Quantum number			
	1st	2nd	3rd	Q	T	T_3	Y
leptons	$\begin{pmatrix} \nu_e \\ e \end{pmatrix}_L$	$\begin{pmatrix} \nu_\mu \\ \mu \end{pmatrix}_L$	$\begin{pmatrix} \nu_\tau \\ \tau \end{pmatrix}_L$	0	1/2	+1/2	−1
				−1	1/2	−1/2	−1
	e_R	μ_R	τ_R	−1	0	0	−2
quarks	$\begin{pmatrix} u \\ d \end{pmatrix}_L$	$\begin{pmatrix} c \\ s \end{pmatrix}_L$	$\begin{pmatrix} t \\ b \end{pmatrix}_L$	+2/3	1/2	+1/2	+1/3
				−1/3	1/2	−1/2	+1/3
	u_R	c_R	t_R	+2/3	0	0	+4/3
	d_R	s_R	b_R	−1/3	0	0	−2/3

Table 1.1: The fermion fields of the Standard Model arranged in $SU(2)_L \otimes U(1)_Y$ multiplets and their quantum numbers; electrical charge Q, weak isospin T, the third component of the weak isospin T_3, and hypercharge Y. The "color" quantum number of the strong force is not included.

Symmetry	Gauge boson	Field	Interaction	Q	Mass[GeV]	Width[GeV]
$SU(2)_L \otimes U(1)_Y$	Photon γ	A_μ	electromagnetic	0	0	–
	Z boson	Z_μ	electroweak	0	91.2	2.5
	$W^\pm$ boson	$W_\mu^\pm$	weak	±1	80.4	2.1
$SU(3)_C$	Gluon g	g_μ^a	strong	0	0	–

Table 1.2: The gauge bosons of the Standard Model and their electrical charge Q, mass and width.

found in [2, 3].) QED is the theory that describes the interactions of electrons and photons. The field associated in QED with the electron and positron is given by a complex Dirac spinor, ψ, having 4 components. The Lagrangian for a free Dirac field is given by:

$$\mathcal{L}_{\text{Dirac}} = \bar{\psi}\left(i\gamma^{\mu}\partial_{\mu} - m\right)\psi, \tag{1.1}$$

where m is the mass of the electron, $\bar{\psi} = \psi^{\dagger}\gamma^{0}$, and γ^{μ} are 4×4 matrices satisfying the anti-commutation rules $\{\gamma^{\mu}, \gamma^{\nu}\} = 2g^{\mu\nu}$.

If we impose a local $U(1)$ gauge transformation we have the following transformation for the Dirac fields:

$$\psi \rightarrow \psi' = U(x)\psi(x) = e^{i\theta(x)}\psi(x), \tag{1.2}$$
$$\bar{\psi} \rightarrow \bar{\psi}' = \bar{\psi}(x)U^{\dagger}(x) = \bar{\psi}(x)e^{-i\theta(x)}, \tag{1.3}$$

where $\theta(x)$ is a function of space-time co-ordinates. If we rewrite the Lagrangian with the transformed fields we see that the Dirac Lagrangian in Equation 1.1 is not invariant under the transformations 1.2:

$$\mathcal{L}_{\text{Dirac}} \rightarrow \mathcal{L}'_{\text{Dirac}} = \mathcal{L}_{\text{Dirac}} - \bar{\psi}\gamma^{\mu}(\partial_{\mu}\theta(x))\psi. \tag{1.4}$$

In order to regain the invariance of the Lagrangian a real gauge field A_{μ} is introduced. We define the covariant derivative D_{μ} as:

$$D_{\mu} \equiv \partial_{\mu} + igA_{\mu} \tag{1.5}$$

and the gauge field transforms as:

$$A_{\mu} \rightarrow A'_{\mu} = A_{\mu} - \frac{1}{g}\partial_{\mu}\theta(x). \tag{1.6}$$

This ensures that the newly defined Lagrangian:

$$\mathcal{L}^{\text{inv}}_{\text{Dirac}} = \bar{\psi}\left(i\gamma^{\mu}D_{\mu} - m\right)\psi \tag{1.7}$$

is invariant under the U(1) transformation, the previous problem terms being canceled:

$$\begin{aligned}\mathcal{L}^{\text{inv}}_{\text{Dirac}} \rightarrow \mathcal{L}^{\text{inv'}}_{\text{Dirac}} &= \bar{\psi}'\left(i\gamma^{\mu}D'_{\mu} - m\right)\psi' \\ &= \bar{\psi}'(i\gamma^{\mu}(\partial_{\mu} + igA'_{\mu}) - m)\psi' \\ &= \mathcal{L}^{\text{inv}}_{\text{Dirac}}.\end{aligned} \tag{1.8}$$

To have the full QED Lagrangian we need to add to the above Lagrangian the kinetic term for the gauge field:

$$\mathcal{L}^{\text{K.E.}} = -\frac{1}{4}F_{\mu\nu}F^{\mu\nu}, \tag{1.9}$$

where $F_{\mu\nu} = \partial_\mu A_\nu - \partial_\nu A_\mu$. A mass term of the form $m^2 A_\mu A^\mu$ cannot be added to the Lagrangian as it is not invariant under the $U(1)$ transformation.

In this way by imposing invariance under $U(1)$ we got from the free Dirac field to an interacting system with the full Lagrangian written as

$$\begin{aligned}\mathcal{L}_{\text{QED}} &= \bar{\psi}\left(i\gamma^\mu D_\mu - m\right)\psi - \frac{1}{4}F_{\mu\nu}F^{\mu\nu} \\ &= \bar{\psi}(i\gamma^\mu\partial_\mu - m) - \underbrace{g\bar{\psi}\gamma^\mu A_\mu\psi}_{\text{Interaction term}} - \frac{1}{4}F_{\mu\nu}F^{\mu\nu}.\end{aligned} \tag{1.10}$$

It is worthwhile to notice that the A_μ field introduced corresponds to the photon. Hence, because the mass term for A_μ is not allowed by invariance, we naturally obtained the massless photon. Also in the interaction term we can identify the coupling constant g with the charge of the electron. In view of Noether's theorem the quantity that is conserved in QED is the electrical charge.

Using the same concept of local invariance we will obtain QCD asking for invariance of the Lagrangian under $SU(3)$. The 8 generators of $SU(3)$[1] will give the 8 gluons that are the force carriers for the strong interaction. The conserved quantity corresponding to this transformation is the quantum number called color, hence the notation $SU(3)_C$. The quarks come in 3 colors but due to color confinement only "uncolored" combinations of quarks are observed.

To describe the electroweak interactions we need to merge $SU(2)_L$ invariance which characterizes the weak interaction and $U(1)$ which characterizes quantum electrodynamics. In this sector a left-handed Weyl neutrino has to be incorporated with a Dirac electron (which can be viewed as the sum of a left-handed and a right-handed Weyl spinor). The left-handed electron and neutrino form an isodoublet under $SU(2)_L$:

$$L_L = \begin{pmatrix} \nu_e \\ e \end{pmatrix}_L, \tag{1.11}$$

while the right handed sector is formed out of isosinglets under $SU(2)_L$, the right

[1] If in $U(1)$ the transformation reads $e^{i\theta(x)}$, in the case of an $SU(N)$ group the transformation will read $e^{i\alpha_a(x)T_a}$, where T_a, $a = 1, N^2 - 1$ are the generators of $SU(N)$.

handed electron[2]:

$$R = e_R. \tag{1.12}$$

We do not consider here a right handed neutrino as it has never been observed.

These lepton sectors transform differently under $SU(2)$:

$$\begin{aligned} L &\to e^{(i/2)\theta^a \sigma_a} L, \\ R &\to R, \end{aligned} \tag{1.13}$$

where σ_a are the Pauli matrices, a specific representation of the generators of SU(2).

The electroweak sector of the Standard Model is hence described by $SU(2)_L \otimes U(1)_Y$, where the generators of $SU(2)$ correspond to the three components of the weak isospin T_i and the $U(1)_Y$ generator to the weak hypercharge Y. These are related to the electric charge by:

$$Q = T_3 + \frac{Y}{2}. \tag{1.14}$$

The Lagrangian describing the electroweak interaction for the left handed fermion doublets ψ_{Lj} is :

$$\mathcal{L}_{\text{EW}} \quad = i\bar{\psi}_{Lj}\gamma^\mu D_\mu \psi_{Lj},$$

ψ_{Lj} being here a left handed doublet of fermions. The covariant derivative for the weak interactions is given by:

$$D_\mu = \partial_\mu + ig\frac{\sigma_a}{2}W^a_\mu + ig'\frac{Y}{2}B_\mu, \tag{1.15}$$

where the index $a = 1, 2, 3$ varies over the degrees of freedom for the weak interactions and the field strength tensors are:

$$W^{\mu\nu}_a = \partial^\mu W^\nu_a - \partial^\nu W^\mu_a + g\epsilon_{abc}W^{b\mu}W^{c\nu}, \tag{1.16}$$

$$B^{\mu\nu} = \partial^\mu B^\nu - \partial^\nu B^\mu. \tag{1.17}$$

The right handed particles do not see the weak interaction and hence for them the Lagrangian is :

[2]In the case of quarks the doublet will be $Q_L = \begin{pmatrix} u_L \\ d_L \end{pmatrix}$ and two singlets u_R and d_R.

$$\mathcal{L}_{\mathrm{EW}} \quad = i\bar{\psi}_{Rj}\gamma^{\mu}D_{\mu}\psi_{Rj},$$

with

$$D_{\mu} = \partial_{\mu} + ig'\frac{Y}{2}B_{\mu} \tag{1.18}$$

and now ψ_{Rj} are the right handed fermion singlets.

The left handed and right handed fields are obtained by using the chiral projectors on the fermion fields

$$P_L = \tfrac{1}{2}(1-\gamma^5), \qquad P_R = \tfrac{1}{2}(1+\gamma^5). \tag{1.19}$$

Thus the left handed fermion field is $\psi_L = P_L\psi$ while the right handed fermion field is $\psi_R = P_R\psi$. For massless particles the chirality corresponds to the helicity[3]. In the case of massive particles the helicity depends on the frame of reference, one being always able to boost a right-handed particle in a frame in which it is left-handed. One should notice that chirality remains an observer independent quantity.

We can also notice here that $SU(2)_L \otimes U(1)_Y$ is not really a unification as there are two different gauge couplings introduced, respectively g and g'.

1.2 Higgs mechanism

So far all the non-abelian gauge fields and fermions are massless. The simplest way to generate masses for the non-abelian gauge fields and fermions is through the Higgs mechanism via spontaneous symmetry breaking [4]. The SM is defined with the simplest realization of the Higgs mechanism, adding to the theory one complex scalar doublet with appropriate hypercharge $Y(\Phi) = 1$:

$$\Phi = \begin{pmatrix} \phi^+ \\ \phi^0 \end{pmatrix} = \frac{1}{\sqrt{2}}\begin{pmatrix} \phi_1 + i\phi_2 \\ \phi_3 + i\phi_4 \end{pmatrix}, \tag{1.20}$$

with gauge kinetic term and self interaction:

$$\mathcal{L}_{\mathrm{Higgs}} = (D^{\mu}\Phi)^{\dagger}(D_{\mu}\Phi) - V(\Phi^{\dagger}\Phi), \tag{1.21}$$

[3]Helicity is defined as the sign of the projection of the spin of a particle onto its momentum direction.

where

$$V(\Phi^\dagger\Phi) = \frac{\mu^2}{2}\Phi^\dagger\Phi + \frac{\lambda}{4}(\Phi^\dagger\Phi)^2. \tag{1.22}$$

The parameter λ has to be positive such that the Higgs potential $V(\Phi^\dagger\Phi)$ is not negative for arbitrarily large values of the field Φ. The Higgs potential has one trivial minimum in the case $\mu^2 > 0$, but in the case $\mu^2 < 0$ non trivial minima exist. The set of non-trivial minima forms a surface given by the equation (see Figure 1.1):

$$\phi^2_{1,min} + \phi^2_{2,min} + \phi^2_{3,min} + \phi^2_{4,min} = v^2, \tag{1.23}$$

with

$$v = \sqrt{\frac{-\mu^2}{\lambda}}, \tag{1.24}$$

where $v \approx 246$ GeV is the vacuum expectation value.

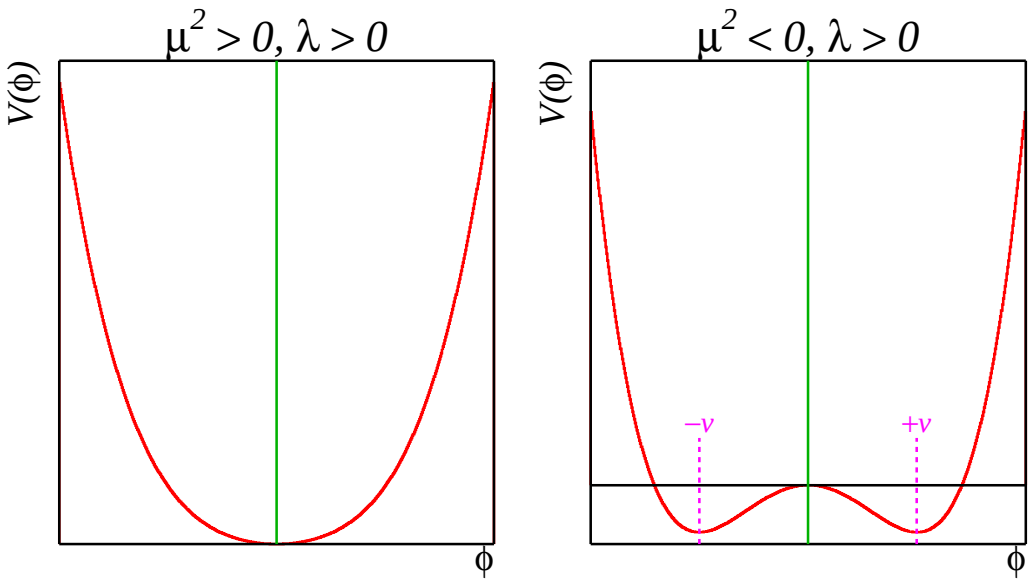

Figure 1.1: Higgs potential $V(\Phi^\dagger\Phi) = \frac{\mu^2}{2}\Phi^\dagger\Phi + \frac{\lambda}{2}(\Phi^\dagger\Phi)^2$.

In the case $\mu^2 < 0$ the minimum of the field would be at $|\phi| = v$ (see Figure 1.1). The vacuum is broken by choosing one of the minima. In order to break only $SU(2)$ and not break $U(1)$, the first component of the field has to be zero $\phi_1 + i\phi_2 = 0$.

We choose a minimum such that $\phi_4 = 0$ and we can expand the scalar field around the minimum of the potential $\phi_3(x) = v + h(x)$,

$$\Phi(x) = \frac{1}{\sqrt{2}} \begin{pmatrix} 0 \\ v + h(x) \end{pmatrix}. \tag{1.25}$$

Due to the spontaneous breaking of $SU(2)_L \otimes U(1)_Y$, the massless gauge fields, forming an isotriplet under $SU(2)_L$, absorb three of the degrees of freedom introduced by the Higgs field and form the real $W^{\pm}$ fields:

$$W^{\pm}_{\mu} = \frac{1}{\sqrt{2}}(W_1 \mp iW_2)_{\mu}. \tag{1.26}$$

The photon and respectively the Z-boson become mixtures of the neutral W_3 component with the abelian gauge field B

$$A_{\mu} = -\sin\theta_W W^3_{\mu} + \cos\theta_W B_{\mu}, \tag{1.27}$$

$$Z_{\mu} = \cos\theta_W W^3_{\mu} + \sin\theta_W B_{\mu}, \tag{1.28}$$

with $\tan\theta_W = g'/g$ the weak mixing angle and the electric charge $e = g\ \sin\theta_W$.

Rewriting the Lagrangian in terms of v and $h(x)$ we obtain the masses for the gauge bosons:

$$m_{\mathrm{W}^{\pm}} = \tfrac{g}{2}v, \quad m_{\mathrm{Z}} = \tfrac{v}{2}\sqrt{g^2 + g'^2}, \quad m_{\gamma} = 0. \tag{1.29}$$

The fermions acquire mass via Yukawa couplings to the Higgs field. The Yukawa part of the Lagrangian reads for each fermion:

$$\mathcal{L}_{\mathrm{Yukawa}} = -\lambda_f \bar{L}\Phi R - \lambda_f \bar{R}\Phi^{\dagger} L. \tag{1.30}$$

The constant terms in front of the $\bar{L}R$ are identified with the fermion masses $m_f = \lambda_f v/\sqrt{2}$. One should bear in mind that the left-chiral eigenstates d' of the down quarks are mixed combinations $\mathrm{d}'_{\mathrm{i}} = \sum_{\mathrm{j}} \mathrm{V}_{\mathrm{ij}}\mathrm{d}_{\mathrm{j}}$, where V_{ij} is the Cabibbo-Kobayashi-Maskawa matrix (V_{CKM}). The off diagonal terms in V_{CKM} give rise to family-changing charged weak interactions and hence, for example, a b-quark can decay into a c-quark.

The Higgs particle mass itself is not predicted by theory, even if the Lagrangian contains a mass term for the Higgs $M^2_{\mathrm{H}} = 2\lambda v^2$. However, constraints on the Higgs mass can be derived from theory and inferred from high precision electroweak measurements.

1.3 Direct and indirect constraints on the Higgs mass

1.3.1 Constraints from theory

Higher order processes in the SM can be viewed as perturbative expansions in coupling constants. Based on the assumptions on the scale up to which the SM is assumed to be valid before perturbation theory breaks down one can derive constraints on the mass of the Higgs boson.

Any process considered in the theory has to be unitarity bound. That is similar to saying that the probability of any outcome of a specific process is at most equal to 1. If one considers the scattering of charged bosons $\mathrm{W^+W^-} \to \mathrm{W^+W^-}$ in the high energy limit $s \gg M_{\mathrm{W}}^2$, the limit where the heavy W bosons behave as massless bosons, the amplitude of this process can be written as [5]:

$$A(\mathrm{W^+W^-} \to \mathrm{W^+W^-}) \sim -\left[2\frac{M_{\mathrm{H}}^2}{v^2} + \left(\frac{M_{\mathrm{H}}^2}{v}\right)^2 \frac{1}{s - M_{\mathrm{H}}^2} + \left(\frac{M_{\mathrm{H}}^2}{v}\right)^2 \frac{1}{t - M_{\mathrm{H}}^2}\right]. \tag{1.31}$$

The unitarity condition for this process translates into a direct constraint on the Higgs mass :

$$\frac{M_{\mathrm{H}}^2}{8\pi v^2} < \frac{1}{2} \text{ in the limit } M_{\mathrm{H}}^2 \ll s, \tag{1.32}$$

which gives an upper bound on the Higgs mass:

$$M_{\mathrm{H}} \lesssim 870 \text{ GeV}. \tag{1.33}$$

If one adds more channels (ZZ, HH, ZH, WH, WZ) the above condition becomes more stringent and the unitarity in the SM would be violated for Higgs masses higher than about 700 GeV.

The theory is a perturbative theory and hence the quartic coupling of the Higgs field λ needs to be finite at all energy scales. Considering all 1-loop corrections to the Higgs quartic couplings, one can write using the Renormalization Group Equations the variation of the quartic Higgs coupling with the energy scale Q [5]:

$$\frac{\mathrm{d}}{\mathrm{d}\log Q^2}\lambda(Q^2) = \frac{3}{4\pi^2}\lambda^2(Q^2) + \text{higher orders} \tag{1.34}$$

and the solution for this equation taking as reference point the electroweak symmetry breaking point $Q_0 = v$:

$$\lambda(Q^2) = \lambda(v^2)\left[1 - \frac{3}{4\pi^2}\lambda(v^2)\log\frac{Q^2}{v^2}\right]^{-1}. \tag{1.35}$$

One can see that for very small values of $Q \ll v$, much smaller than the electroweak symmetry breaking scale, λ goes to zero and the theory becomes trivial. In the opposite limit $Q \gg v$ the quartic coupling grows and becomes infinite at the Landau pole:

$$\Lambda_c = v \exp\left(\frac{4\pi^2}{3\lambda}\right) = v \exp\left(\frac{4\pi^2 v^2}{M_{\mathrm{H}}^2}\right). \tag{1.36}$$

This can be turned into a condition on the Higgs mass by asking that the quartic coupling remains finite up to the scale where the SM is valid, and that scale is set to the Landau pole Λ_c. This is an extension from the triviality argument in ϕ^4 theories that requires that the quartic coupling is identically zero in order for the theory to remain perturbative at all scales. This limit on the Higgs boson mass is called the triviality bound.

If in addition one takes into account contributions from the fermions and gauge bosons in the running of the quartic coupling, a new bound on the Higgs mass can be derived. Because the Higgs couplings are proportional to the mass of the particles, only the contributions from the top quarks and massive gauge bosons have a considerable contribution. Considering that the quartic coupling satisfies $\lambda \ll \lambda_{\mathrm{t}}, g, g'$ (λ_{t} is the Yukawa coupling of the top quark $\lambda_{\mathrm{t}} = \sqrt{2}m_{\mathrm{t}}/v$) and requiring that $\lambda(Q^2)>0$ one gets a condition on the Higgs mass:

$$M_{\mathrm{H}}^2 > \frac{v^2}{8\pi^2}\left[-12\frac{m_{\mathrm{t}}^4}{v^4} + \frac{3}{16}(2g^4 + (g^2+g'^2)^2)\right]\log\frac{Q^2}{v^2}. \tag{1.37}$$

This condition is known as the vacuum stability bound. If $\lambda(Q^2)<0$ the scalar potential $V(Q)<V(v)$ and the vacuum has no minimum anymore. Hence in order to have a scalar potential that is bounded from below one needs to ask that condition 1.37 holds.

The bounds on the Higgs boson mass as a function of the scale Λ up to which the SM is valid (or at which energy "New Physics" is expected) can be seen in Figure 1.2.

1.3.2 Experimental constraints

Direct searches for the Higgs boson have been conducted at LEP and Tevatron. During LEP1 when the center of mass energy was close to the Z boson mass, the Higgs could be produced in association with a Z boson. The Higgs main decay channel at LEP is into two b quarks. The topologies in which the Higgs search was done at LEP1 are:

- Z decays into neutrinos and the Higgs into two b-jets;

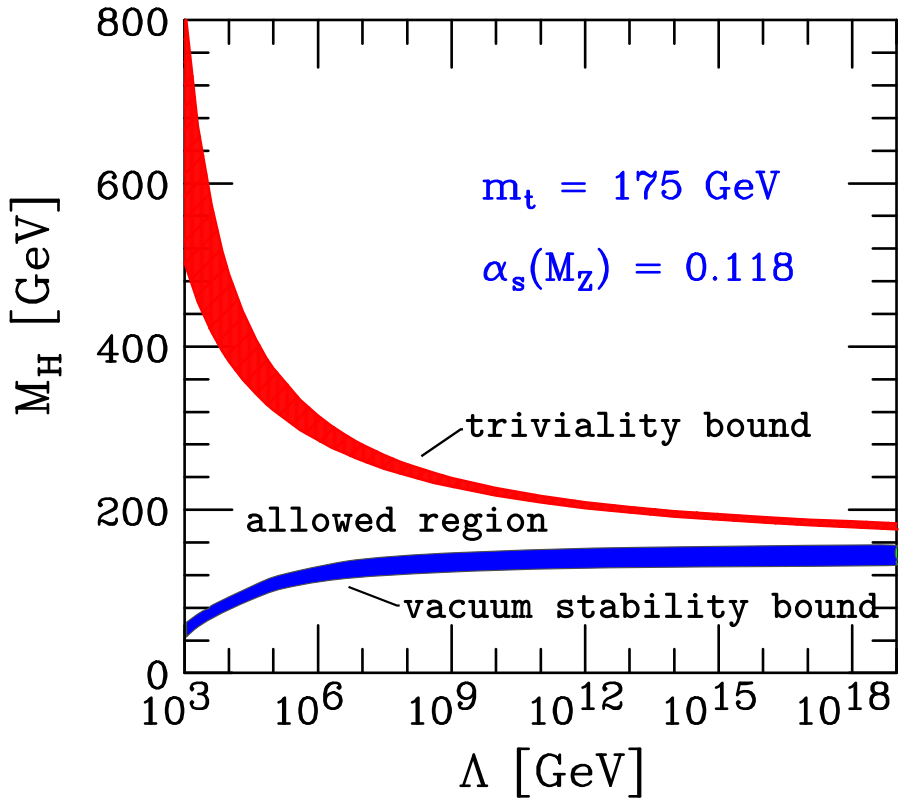

Figure 1.2: The triviality bound and the vacuum stability bound on the Higgs boson mass as a function of the cut-off scale Λ; the allowed region lies between the two bands [6]. The bands indicate the theoretical uncertainty on the curves.

- Z decays into two isolated leptons (electrons or muons) and the Higgs into two b-jets.

In the absence of any signal in all 4 LEP experiments a combined exclusion of a Higgs mass below 60 GeV at 95% Confidence Level was set.

At LEP2 when the center of mass energy went up to $\sqrt{s} = 209$ GeV the Higgs is produced via Higgs-strahlung where an off-shell Z boson splits into a real Z boson and the Higgs. The topologies considered were:

- topologies considered during LEP1;
- Z decays into two tau leptons and the Higgs into two b-jets;
- Z decays into two jets and Higgs into two tau leptons;
- Z decays into two jets and Higgs into two b-jets.

Combining the results of all 4 LEP experiments, no excess over the Standard Model was observed and values of M_{H} below 114.4 GeV were excluded at 95% Confidence Level.

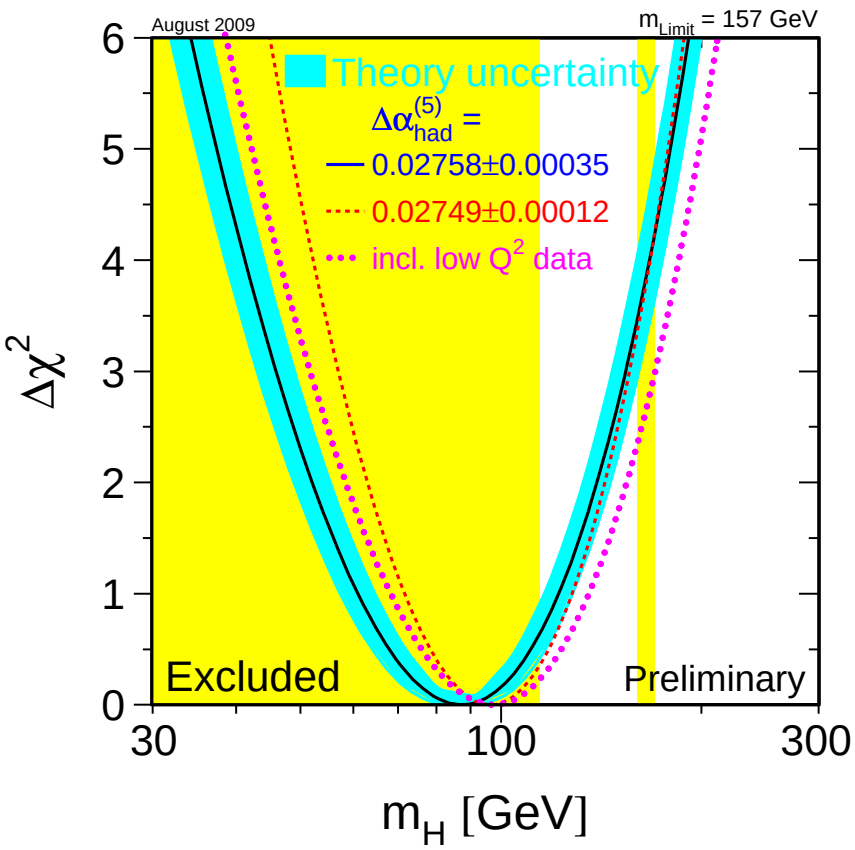

Figure 1.3: The $\Delta\chi^2$ of the fit to the electroweak parameters and the Higgs mass as a function of the Higgs mass [7].

Because most electroweak parameters are sensitive to the Higgs mass as the Higgs contributes to these parameters through loop corrections, one can place indirect constraints on the Higgs mass. Precision measurements of 18 electroweak parameters, such as the mass and width of the W boson and of the Z boson, mass of the top quark, etc. have been combined in a global fit with the Higgs mass, using data from LEP, SLC and the Tevatron. The $\Delta\chi^2(m_{\mathrm{H}}) = \chi^2_{\mathrm{min}}(m_{\mathrm{H}}) - \chi^2_{\mathrm{min}}$ of the fit as a function of the Higgs mass is shown in Figure 7.3. The Higgs mass corresponding to the minimum of this fit is $m_{\mathrm{H}} = 84^{+35}_{-26}$ GeV. The fit $\chi^2/\mathrm{d.o.f.} =$

17.3/13 [7] corresponds to a 18% probability. The largest uncertainty in this fit is due to the mass of the W boson and to a lesser extent the mass of the top quark.

1.4 Higgs production at the Tevatron

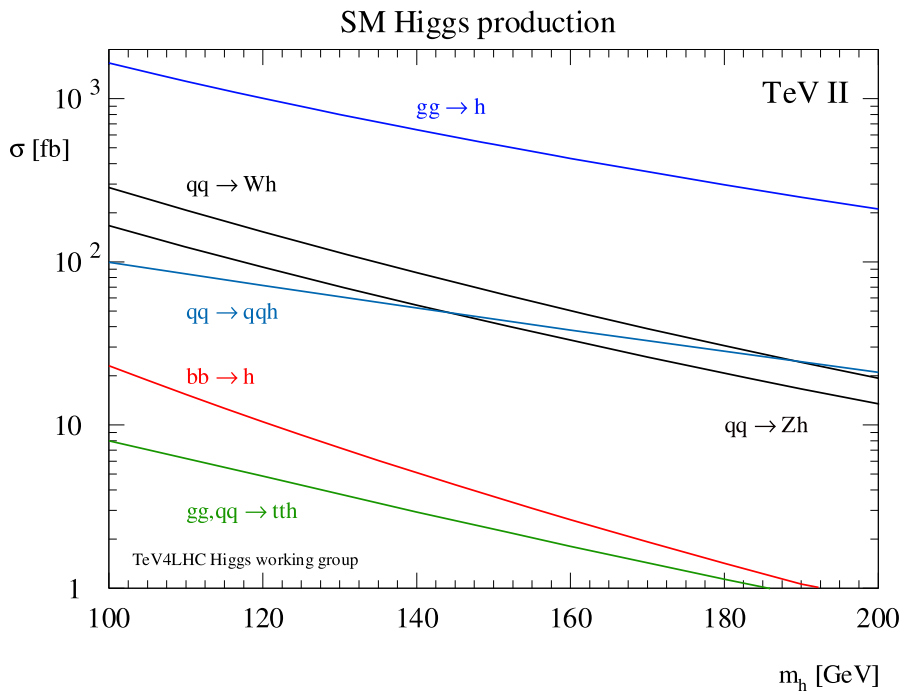

Figure 1.4: The production cross section for the SM Higgs boson in proton-antiproton collisions at $\sqrt{s} = 1.96$ TeV [8].

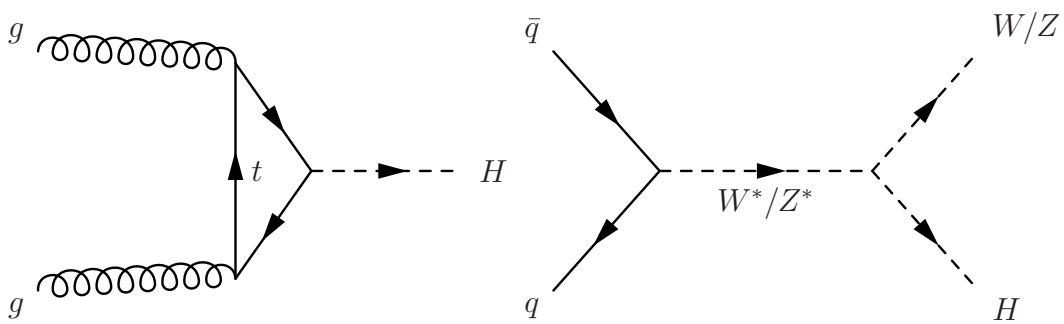

Figure 1.5: Higgs production processes at the Tevatron: gluon fusion through a top loop (left), and Higgs-strahlung of a $W^{\pm}$ or a Z boson (right).

The cross sections for the main production channels of the Higgs at the Tevatron can be seen in Figure 1.4. The main production channels can be divided into two categories depending on the process that gives rise to the Higgs: the gluon fusion channel and the associate production channel.

The highest cross section at Tevatron is for the gluon fusion channel, where the Higgs is produced via a top quark loop (see Figure 1.5). The cross section for this channel is 1657 (211) fb for a 100 (200) GeV mass Higgs and is much higher than either of the associated production channels. Associated production occurs when the Higgs is radiated off a W or Z produced from a $q\bar{q}$ interaction. This process can be seen as a Drell-Yan production of an offshell W/Z that radiates a Higgs. The cross section for these channels varies from 286 to 19.3 fb for WH production and from 167 to 13.5 fb for ZH production when going from a 100 GeV to a 200 GeV mass Higgs.

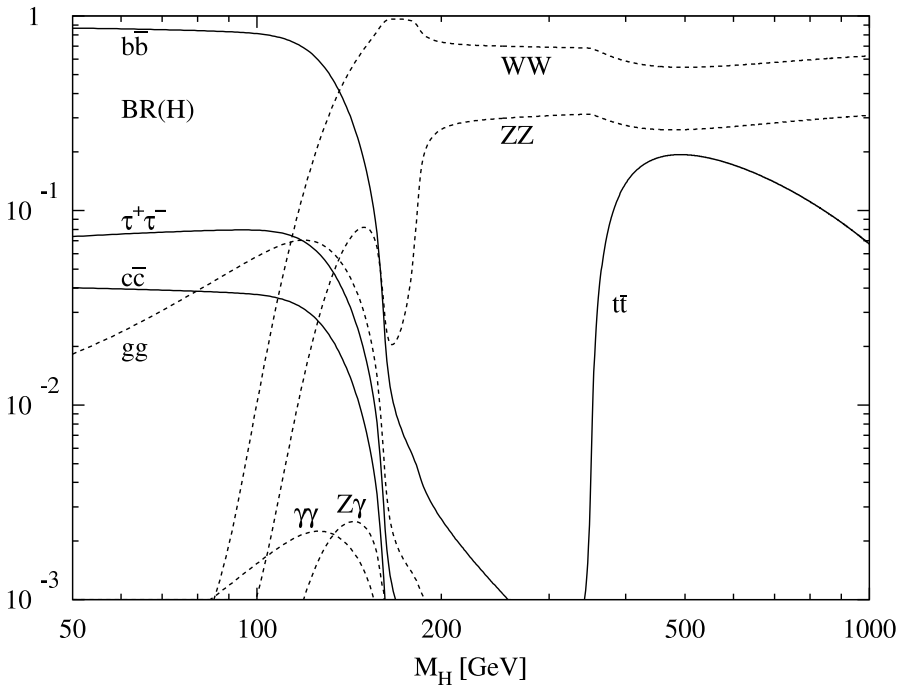

Figure 1.6: The branching ratios for the SM Higgs boson as a function of m_{H}, calculated using the HDECAY program [9].

The Higgs will decay mostly into the highest mass fermion or boson pair available. This is due to the coupling of the Higgs with the other particles, which is proportional to the mass of those particles. In Figure 1.6 the branching ratios of the Higgs decay into different channels as a function of Higgs mass can be seen. Based on the highest branching ratio we can divide the Higgs mass range into two regions: a low-mass region, $m_{\mathrm{H}} < 140$ GeV, where the Higgs decay is predomi-

nantly into a pair of b-quarks; and a high-mass region, $m_{\mathrm{H}} > 140$ GeV, where the Higgs decays predominantly into a W boson pair.

The cross sections and the decay branching ratios interplay and give two search strategies at the Tevatron. At low Higgs masses the production $\mathrm{gg} \rightarrow \mathrm{H} \rightarrow \mathrm{b}\bar{\mathrm{b}}$ is hard to put into evidence as it is engulfed by the huge multijet production. The only channels that can be accessed in the low-mass region at Tevatron are the associated production channels where leptonic decays of the W or the Z are used to reduce the multijet backgrounds. In the high mass region the $\mathrm{gg} \rightarrow \mathrm{H} \rightarrow \mathrm{W}^{+}\mathrm{W}^{-}$ is the most performant channel as it benefits from the highest production cross-section and the highest branching ratio and the W bosons can be readily identified in their leptonic decays.

Chapter 2

The Tevatron and the DØ detector

2.1 The Tevatron

In order to study the properties of the interactions between elementary particles these interactions need to be produced in a controlled environment. Such a place is the Tevatron, the collider at Fermi National Accelerator Laboratory (or Fermilab).

The Fermilab complex consists of a series of eight accelerators as shown in Figure 2.1. The biggest of them is the Tevatron. Here the protons and antiprotons, produced and accelerated in the previous seven accelerators, are accelerated to the final energy of 980 GeV and then put into collision in two specific regions.

The Fermilab accelerator complex delivers beams also to other experiments. Further on we will refer only to the segments that are used to provide the proton and antiproton beams used in the Tevatron [10].

The Pre-accelerator is the first stage in the complex. Here hydrogen gas is transformed into ionized hydrogen gas H^- and then accelerated to 750 keV by a Cockcroft-Walton generator. From the pre-accelerator the hydrogen ions are transferred into a 150 m linear accelerator (Linac). The Linac consists of 11 radio frequency (RF) cavities and here the ion beam is accelerated to 400 MeV.

Next the beam is transferred to the Booster. During this transfer the H^- beam is passed through a thin carbon foil that strips off all the electrons and the remaining protons are accelerated in the Booster to a final energy of 8 GeV. This is the first circular accelerator in this chain. It has a radius of 75 m and the acceleration is achieved using 18 RF cavities.

The next step in acceleration is the Main Injector. The Main Injector can work in several modes, two of which are of interest in this context. In the first mode the protons are accelerated to 150 GeV and then transferred to the Tevatron. In the second mode the protons are accelerated to 120 GeV, transferred to the Antiproton Source where they are focused onto a nickel target. A series of secondary particles is

Accelerator	Initial kinetic energy (GeV)	Final kinetic energy (GeV)	Size[a] (m)	Destination of beam
Preacc	~ 0	$7.5 \cdot 10^{-4}$	15	Linac
Linac	$7.5 \cdot 10^{-4}$	0.4	120	Booster
Booster	0.4	8	75	Main Injector
Main Injector	8	120	529	Antiproton source
		150	529	Tevatron
Tevatron	150	980	1000	Stays in Tevatron
				$\bar{p}$ to Recycler
Antiproton source	8	8	75	Main Injector
Recycler	8	8	529	Main Injector

[a] for linear accelerators the length and for circular ones the average radius

Table 2.1: Fermilab accelerator parameters.

produced and then passed through a Lithium lens that converges them into a more parallel beam. This beam is passed through a magnet which selects negatively charged particles with momenta around 8 GeV. The particles that survive this selection are antiprotons. They are injected into the Debuncher.

The Debuncher is a rounded triangular-shaped synchrotron and its purpose is to capture the high momentum spread antiprotons and to decrease this momentum spread. This is achieved by using RF manipulation and beam-cooling. The beam cooling is achieved by stochastic cooling (a signal from the circulating antiprotons is picked up on one side of the ring and then applied to another part of the ring).

From the Debuncher the antiproton beam is transferred to the Accumulator. The Accumulator is a storage ring housed in the same tunnel as the Debuncher. Here the antiprotons are further cooled and accumulated. The antiproton production process is quite inefficient: from 10^5 protons hitting the target only 1-2 antiprotons are captured and stored [11]. Having in mind that the quality of collisions achieved in Tevatron and the duration of one store is highly dependent on the number of antiprotons and the quality of the antiproton beam, it means that the antiproton production is a bottleneck for Tevatron operation.

At this moment the particles needed for producing collisions are obtained and available. All that remains to be done is injection into the Tevatron. The Tevatron is a superconducting magnet synchrotron with a radius of 1 km that accelerates

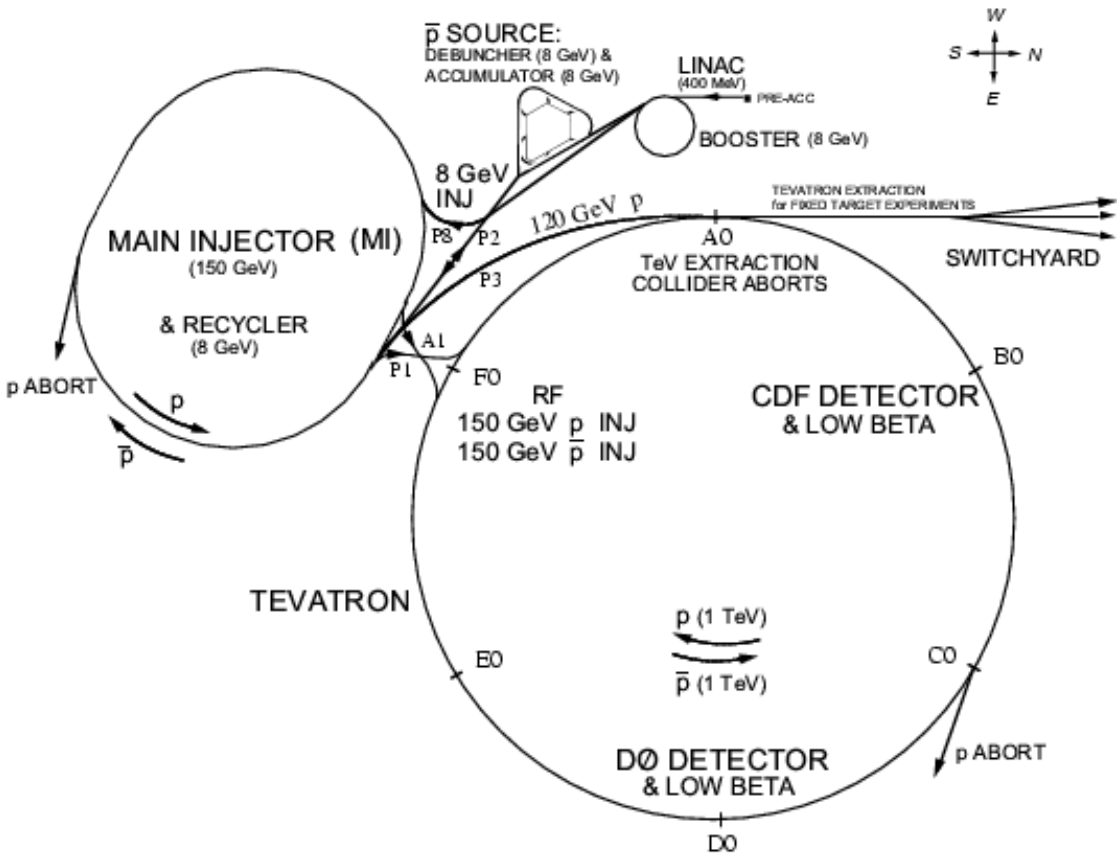

Figure 2.1: Fermilab accelerator complex.

protons and antiprotons in opposite directions to a final energy of 0.98 TeV. Because the particles accelerated are one the antiparticle of the other only one beam pipe is required, the beams cycling in circular trajectories. The Tevatron is split into six sections labeled A to F, each section being split into 6 subsections labeled Ø to 6. Each Ø subsection is a straight section and some of them are special. FØ is the location of the Tevatron 8 RF cavities and the transfer lines to the Main Injector. BØ is the home of the CDF detector, while DØ is the home of the detector with the same name.

The Tevatron loading process is briefly described below. The 8 GeV antiprotons from the Accumulator are transferred into the Main Injector and accelerated to 150 GeV. Then after being coalesced (4 Accumulator bunches are transformed into a single bunch) they are injected into the Tevatron. This is repeated until the antiprotons are arranged inside the Tevatron into 3 trains each containing 12 bunches. The trains are separated by 2.617 μs intervals and the bunches are separated by 396 ns intervals. The proton beam injection into the Tevatron and

beam structure inside the Tevatron are the same also for the proton with the only difference that 7 Booster bunches are coalesced into one bunch. After the protons are loaded into the Tevatron both beams are accelerated from 150 GeV to 980 GeV and then brought into collision at sections BØ and DØ where focusing quadrupoles are placed (the so called low β quadrupoles) [12].

Under normal working conditions there will be 36×36 bunches in the Tevatron colliding at 35 cm long interaction regions at the BØ and DØ sections providing $p\bar{p}$ collisions to both experiments.

In order to increase the rate of accumulation of the antiprotons in the Accumulator, the Recycler is used to collect antiprotons transferred from the Accumulator. In the Recycler the antiprotons are cooled and when needed for a new store are injected to the Main Injector. The cooling in the Recycler is achieved through stochastic and electron beam cooling.

2.1.1 Luminosity and beam lifetime

Luminosity is a measure of the rate of interactions

$$R = \sigma_{int} L \tag{2.1}$$

where σ_{int} is the interaction cross-section and L the luminosity. The luminosity depends on the number of bunches, the revolution frequency and the area of the beams:

$$L = \frac{f n N_p N_{\bar{p}}}{A} \tag{2.2}$$

where N_p and $N_{\bar{p}}$ are the number of particles in each bunch, f is the revolution frequency, n is the number of bunches in either beam and A is the cross-sectional area of the beams. For Gaussian shaped beams A can be defined in terms of the Gaussian width and hence the Tevatron luminosity is defined as:

$$L = \frac{f n N_p N_{\bar{p}}}{2\pi(\sigma_p^2 + \sigma_{\bar{p}}^2)} \cdot F\left(\frac{\sigma_l}{\beta^*}\right) \tag{2.3}$$

where σ_p and $\sigma_{\bar{p}}$ are measures of the width of the bunch, $F(\sigma_l/\beta^*)$ is a form factor decreasing the luminosity due to the longitudinal extent of the bunches and is dependent on the bunch length σ_l and the beta function at the interaction point β^* [12].

The luminosity delivered by the Tevatron to DØ is of the order of $2{\cdot}10^{32}$ cm^{-2}s^{-1}, exceeding usually at the beginning of the store $3 \cdot 10^{32}$ cm^{-2}s^{-1}. Stores are usually terminated when the luminosity goes down to $0.4 \cdot 10^{32}$ cm^{-2}s^{-1}. In Figure 2.2 one can see the evolution of the instantaneous luminosity as a function of time during

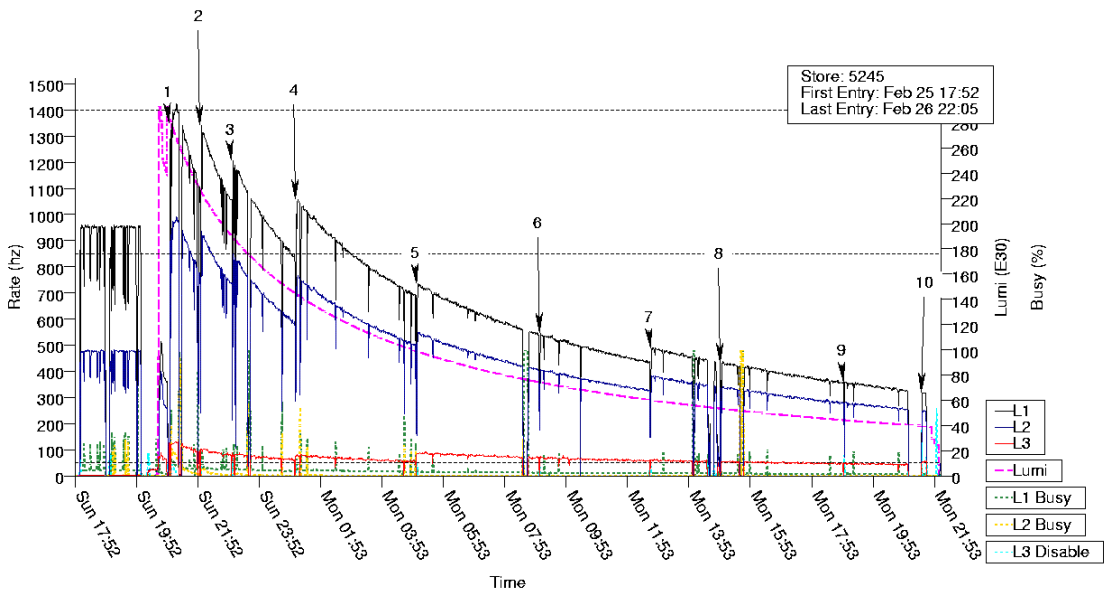

Figure 2.2: Physics store 5245. The dashed line refers to the instantaneous luminosity, $2.88 \cdot 10^{32}$ cm^{-2}s^{-1} at the beginning. The solid lines are the trigger Level 1, Level 2, and the Level 3 output rates. Each run, referred to by numbers, is ended after two or four hours and the set of triggers is changed to account for the change in luminosity. DØ recorded 7.44 pb^{-1} in this store with a data taking efficiency of 89% [14].

a store and can notice that it has an exponential decay. The beam depletion is predominantly due to particle collisions at high luminosities and due to beam-beam interactions and intra-beam scattering at low luminosities [13]. In Figure 2.3 one can see the integrated luminosity delivered by the Tevatron to the DØ experiment and the recorded luminosity. The fact that the recorded luminosity is smaller than the delivered luminosity is due to: deadtimes of the detector, subdetectors not functioning properly, and special runs that are taken for calibration purposes that are not included in the recorded luminosity. The data taking efficiency of the DØ detector exceeds 90% on a regular basis.

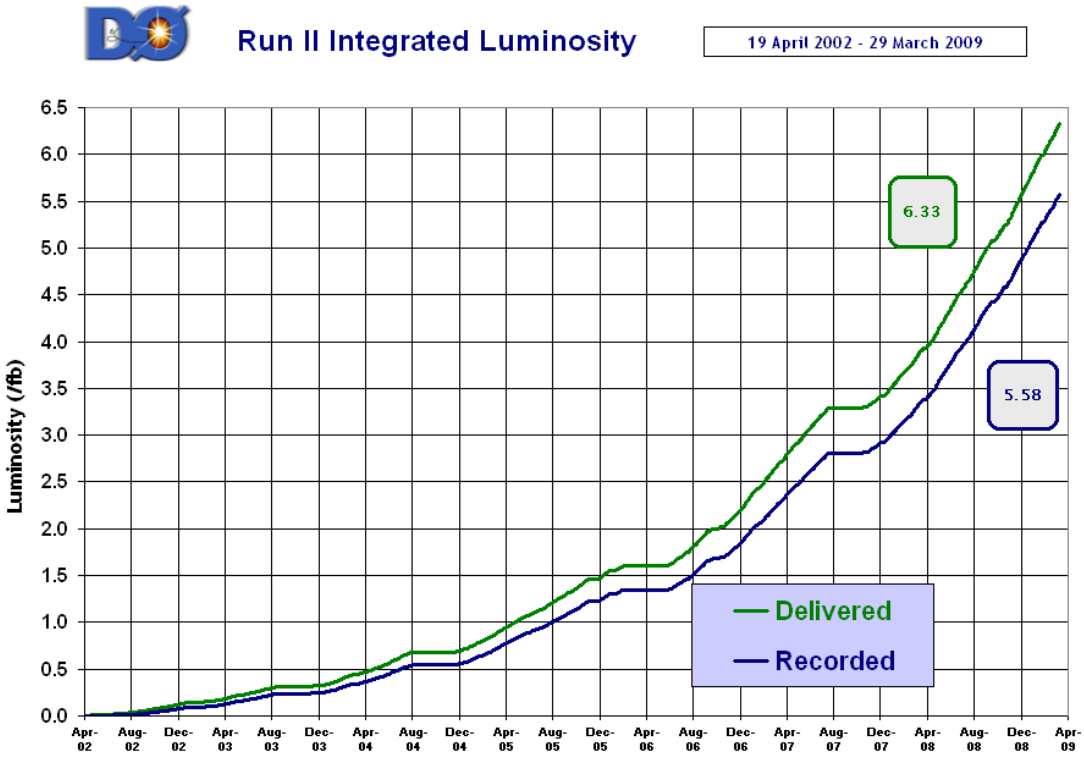

Figure 2.3: Total integrated DØ luminosity. The upper curve represents the delivered luminosity, the lower curve the recorded luminosity.

2.2 The DØ detector

The DØ Detector is a general purpose detector that has a layered structure and approximate axial symmetry. The purpose of the detector is to identify the particles produced in the $p\bar{p}$ collisions and to measure their momenta and energy. The detector consists of four major subsystems: central tracking detectors, calorimeters, a muon spectrometer and a trigger and data acquisition system. Besides the systems named above there are also other support subsystems used for data storage, luminosity monitoring, radiation monitoring and other control and monitoring systems. The detector has passed through a series of upgrades over time, the last one being in 2006. A brief description of the detector as it is after 2006 is given below. A full and extensive description of the DØ detector can be found in [15, 16].

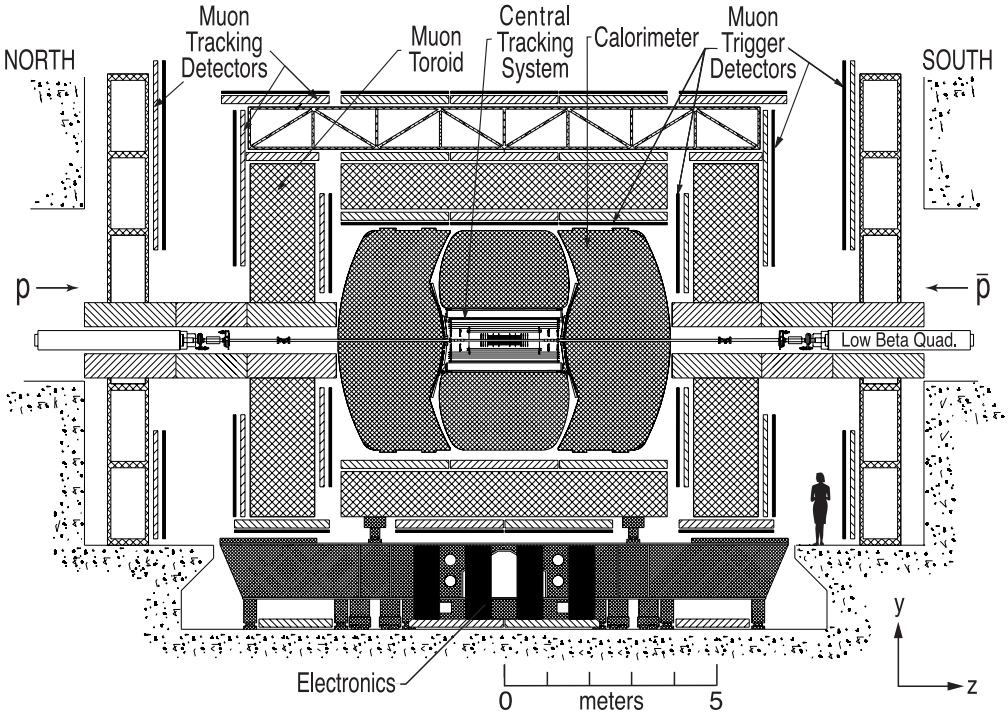

Figure 2.4: DØ Detector axial cut view from inside the Tevatron ring.

2.2.1 Detector coordinate system

In describing the detector and data analysis, we use a right-handed cartesian coordinate system (x, y, z) in which the z-axis is along the proton direction in the detector, the y-axis points upward and the x-axis points toward the center of the Tevatron (Figure 2.1 and Figure 2.4). Cylindrical (r, ϕ, z) and spherical (r, θ, ϕ) coordinate systems are also used and are defined in the following way: the polar angle θ is measured with respect to the positive z axis, the azimuthal angle ϕ is measured with respect to the positive x axis. Instead of the polar angle θ, often pseudorapidity is used when referring to physics objects with the following definition:

$$\eta = -\ln \tan(\theta/2) \tag{2.4}$$

For particles with high energy, for which the mass of the particle can be neglected, pseudorapidity is a good approximation of true rapidity:

$$y = \frac{1}{2} \ln \left[\frac{E + p_z}{E - p_z} \right] \tag{2.5}$$

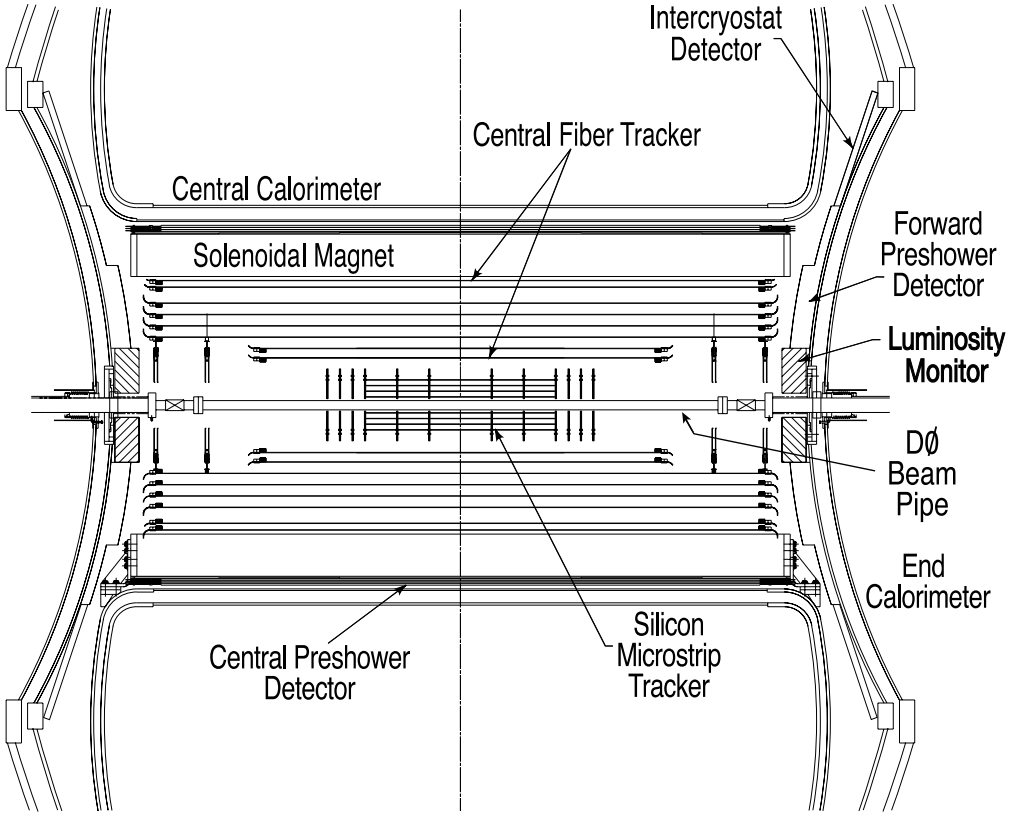

Figure 2.5: Cross-section view of the central tracking system in the $x - y$ plane. Also seen in the picture are the solenoid, the preshower detectors, luminosity monitor and the calorimeters.

2.2.2 Central tracking detectors

The central tracking detectors are the Silicon Microstrip Tracker (SMT) and Central Fiber Tracker (CFT). They are situated right at the heart of the DØ detector, being bordered by the beryllium beampipe on the inner side and the solenoidal magnet on the outer side. Because they need to be fitted together with the solenoidal magnet inside the calorimeter their total size is limited to the inner space of the calorimeter as shown in Figure 2.5.

The purpose of the solenoidal magnet is to provide a uniform axial magnetic field in the central tracking system. The charged particles produced in the collisions will have a curved trajectory and their momenta and charge can be determined. The DØ solenoidal magnet is 2.73 m in length, 1.42 m external diameter and $\sim$ 1.08 m internal diameter. It is a superconducting magnet and in nominal working conditions provides a uniform 2 T magnetic field in the central region.

Silicon Microstrip Tracker

The Silicon Microstrip Tracker (SMT) is at the center of the DØ detector and its purpose is to provide good tracking and momentum measurement for charged particles produced in the interaction. Tracking and momentum measurements are of great importance in finding secondary vertices that signal long lived particles such as B-hadrons. The size of the SMT was driven by the length of the interaction region at DØ.

The SMT consists of about 900 silicon sensors that have doped regions called strips, with a pitch between 50 μm and 135 μm depending on the position in the SMT and type of sensor. An electrical potential difference is applied over the thickness to deplete the sensor of free carriers. When charged particles cross the bulk of the silicon, electrons and holes are created and a signal is read out at the end of the strip. These signals representing "hits" of strips and they are reconstructed into tracks in the SMT using a tracking algorithm.

The SMT is composed of sensors parallel and perpendicular to the beam direction. The parallel sensors are arranged into concentric layers and form units called barrels. There are 6 barrels in the SMT detector. The perpendicular sensors are arranged into disks, 12 smaller size disks called F-disks and 2 bigger H disks (in RunIIa there were 4 H disks). Views of the SMT in RunII can be seen in Figures 2.6 and 2.7.

The sensors in Layer 2 and 4 of the SMT barrels are double sided, having strips and readout on both sides, with a stereo angle of 2° while all other wafers (except Layer Zero) are glued in pairs, back to back with a stereo angle of: 90° in the barrels Layer 1 and 3, 30° for the F-disks and 15° in the H-disks. Due to this arrangement a hit has a well determined measurement in 2 of the 3 directions. We will note here that the most important measurement is in the $r - \phi$ plane because this is the plane in which the charged particles are bent and the momentum of the particles is measured. Dimensions and characteristics of the silicon wafers used are listed in Table 2.2.

During the 2006 upgrade the two outermost H-disks were removed and a new layer of silicon was installed between the first layer of the barrels and the beam pipe called the Layer Zero [17]. The reason for adding this new layer of silicon is that under radiation exposure the silicon wafers impurities concentrations will change and as a consequence the bias voltage needed to deplete the wafer becomes larger, up to the point where the silicon wafer cannot be used anymore. The original SMT was designed with an expected lifetime for the first layer of about 4.9 fb^{-1} [18] and in order to maintain the performance of the silicon detector for longer the new layer of silicon was considered in the upgrade. It was computed that the loss of Layer 1 without the addition of a new layer would degrade the b-quark tagging

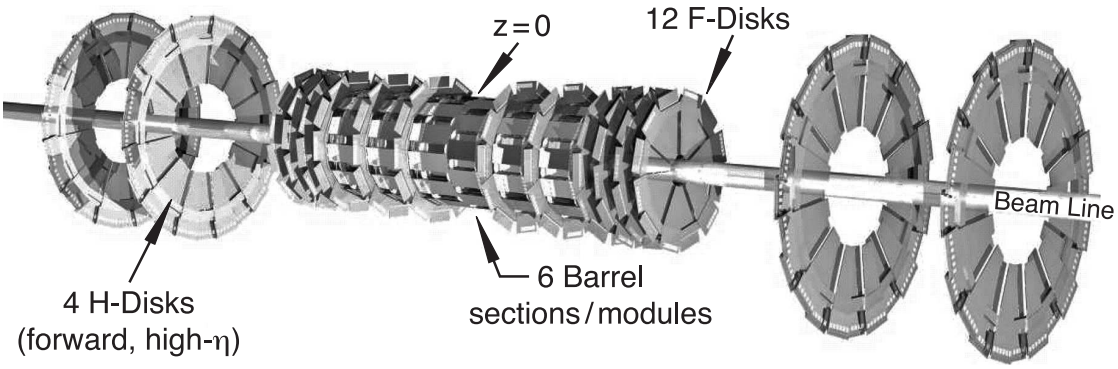

Figure 2.6: Isometric view of the Silicon Microstrip Tracker. The 2 outermost H-Disks were removed to allow the installation of the Layer Zero.

efficiency[1] by 20% [19]. By now the first layer already went through type inversion but there is no indication for lost channels due to the radiation damage. Besides being an insurance for the moment when the first layer will be unusable, the new layer of silicon (Layer Zero) also provides a closer measurement to the interaction point, which is very important for identifying secondary vertices.

The doses of radiation seen by the SMT can be measured by using the Radiation Monitor System which consists of 8 Beam Loss Monitors (BLMs) [20] and 12 silicon diodes placed on the outer F-disks [21]. The BLMs are large argon filled gas counters with a large diameter anode cylinder. They are operated at 2 kV with no amplification to ensure a fast response time. They are placed at each end of the detector, just outside the calorimeter end caps and are integrated in the Tevatron beam monitoring system and can provide an abort signal to the Beam Division in case of high radiation levels.

Central Fiber Tracker

The central fiber tracker (CFT) consists of scintillating fibers which are mounted in eight concentric cylinders with radii from 20 to 52 cm from the center of the beampipe. The outer six cylinders are 2.52 m long while the two inner ones are 1.66 m long to accommodate the SMT H-disks as seen in Figure 2.5. This corresponds to a coverage up to $|\eta| \sim 1.7$ for the outside layers. Each cylinder has two layers of scintillating fibers: one of them parallel to the beampipe (axial layer), and one that has a small stereo angle ϕ of $+3°$ or $-3°$ with respect to the beampipe (stereo layer). The scintillating fibers are 835 μm in diameter.

The scintillation light caused by charged particles traversing the fibers is read out only at one end of the fiber, the other end being made reflective with aluminum

[1]See Section 3.6 for a detailed description of b-quark tagging.

Module	Type	Layer	Pitch(μm) p/n	Length (cm)	Inner radius (cm)	Outer radius (cm)
F-disks	double-sided	-	50/62.5	7.93	2.57	9.96
H-disks	single-sided	-	40	7.63	9.5	26
			80 readout	6.33		
Central	double-sided	1,3	50/153.5	12.0	2.715	7.582
barrels		2,4	50/62.5	6.0	4.55	10.51
Outer	single-sided	1,3	50	6.0	2.715	7.582
barrels	double-sided	2,4	50/62.5	6.0	4.55	10.51
Layer 0		0	81 and 71[a]	7.0 and 12.0[b]	1.6	2.2

[a] in the same barrel the pitch alternates between two sensors

[b] the outer sensors have 12cm in length while the inner ones have 7cm

Table 2.2: Dimensional parameters of the Silicon Microstrip Tracker.

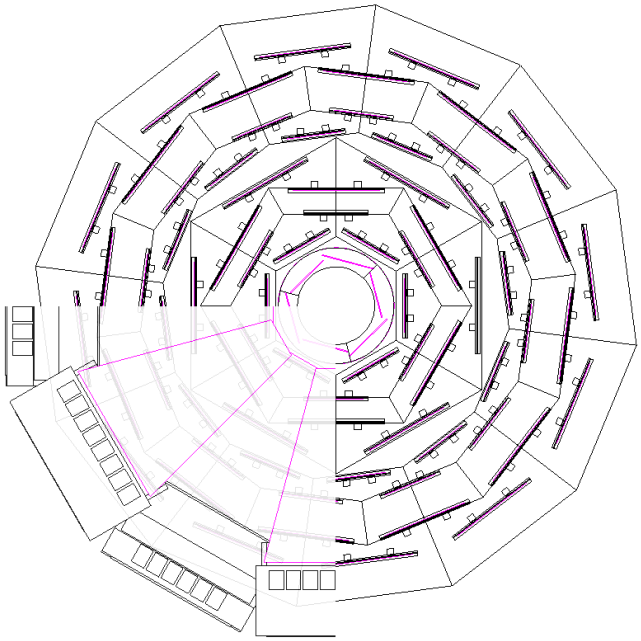

Figure 2.7: Cross section view of one of the SMT barrels.The F-disk sensors can be seen in the lower-left side of the figure.

coating that provides a reflectivity of about 90%. Clear fiber waveguides are coupled to the scintillating fibers and the scintillation light is carried to visible light photon counters (VLPCs). VLPCs are silicon based avalanche photodetectors that operate at 9 K and are capable of detecting single photons. They are characterized by fast response, excellent quantum efficiency ($\geq$ 75%) and a high gain (22,000 to 65,000 electrons produced at the end of the cascade per incoming photon). At this stage the light signal coming from the scintillating fiber is transformed into an electrical signal. The CFT requires 76,800 VLPCs for readout (one for each fiber).

2.2.3 Calorimetry

The present D0 calorimeter system is the same as installed in RunI. During the upgrade to RunII the readout electronics was changed in order to cope with the new beam crossing time. The calorimeter system consists of three sampling calorimeters (primarily uranium/liquid-argon). The calorimeters were designed to provide energy measurement for electrons, photons and jets, and to assist in the identification of electrons, photons, jets and muons. The three calorimeters are: the central calorimeter (CC) with a pseudorapidity coverage $|\eta| \lesssim 1$ and the two end cap calorimeters North (ECN) and South (ECS), which extend the coverage to $|\eta| \lesssim 4$. Each calorimeter is housed in its own cryostat. In order to improve the energy measurement in the gap between the three cryostats an intercryostat detector consisting of sampling layers was designed to improve the calorimetry coverage in the pseudorapidity region $0.8 < |\eta| < 1.4$. Central and forward pre-shower detectors made out of scintillators are placed in front of the calorimeter as seen in Figure 2.5 to improve electron identification.

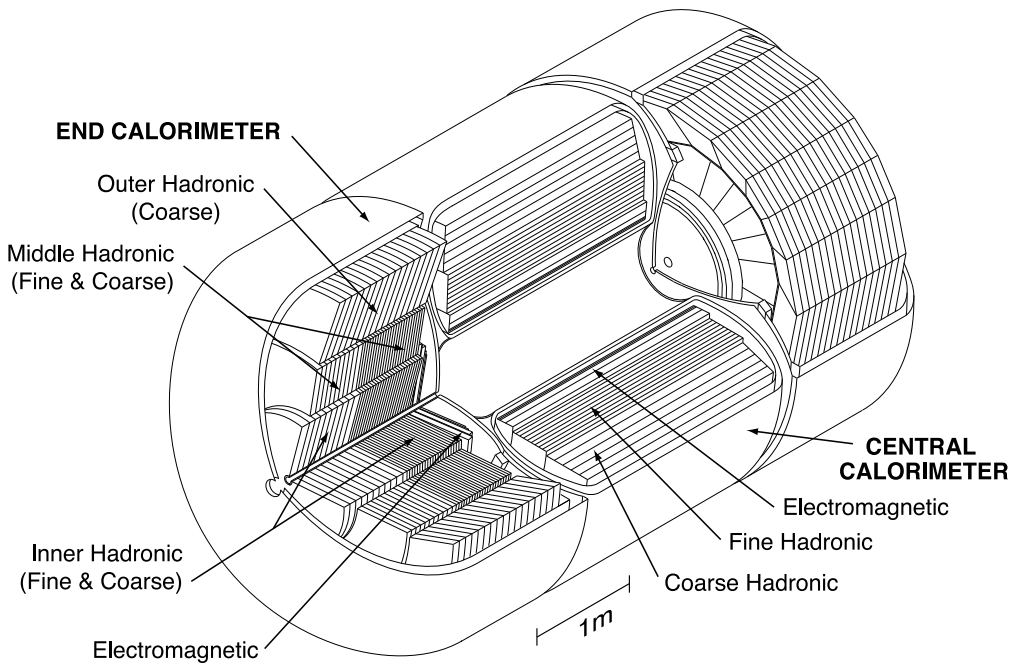

Figure 2.8: Isometric view of the central and two end cap calorimeters.

Calorimeters

The calorimeters are devices that measure the total energy deposited by a particle or a group of particles. Sampling calorimeters consist of layers of absorber material

(that induce showering) and active material. There are two major types of sampling calorimeters: electromagnetic and hadronic, sensitive to the electromagnetic and hadronic induced showers respectively.

Electromagnetic showers are produced by high energy electrons, positrons or photons. The electrons and positrons emit photons via bremsstrahlung. These photons produce pairs of electrons and positrons, which emit more photons via bremsstrahlung. This process continues until the energy of the resulting electrons and positrons is below 10 MeV, where the energy loss is mainly via ionization. These ionizing particles are detected in the active material.

Hadronic showers are induced by hadronic particles which interact with the nuclei predominantly via the strong force. They produce secondary particles with decreasing energy that form a shower. In the DØ liquid argon calorimeter the charged low energy secondary particles ionize the argon and can be detected. The average distance traveled by the particles in a hadronic shower before interaction is longer, on average, than in an electromagnetic shower, hence the hadronic showers penetrate deeper into the calorimeter. This explains the granularity and construction of the calorimeters and also the names of different calorimeter modules (see Figure 2.8).

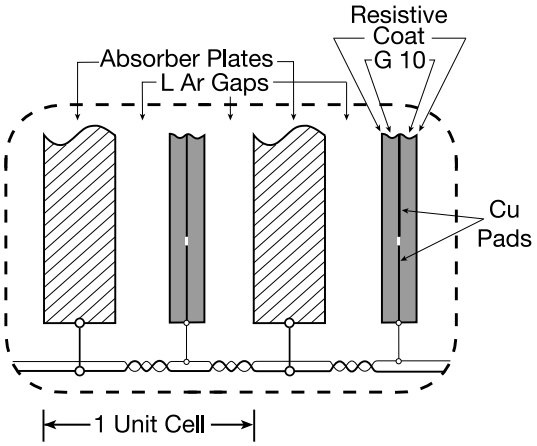

Figure 2.9: Schematic view of the liquid-argon gap and signal board unit cell for the calorimeter.

The cryostats maintain the calorimeter temperature at $\sim$ 90 K. There are different absorber plates used in different parts of the calorimeter. In the electromagnetic sections thin plates (3 mm in CC , 4 mm in EC) of nearly pure depleted uranium are used. In the fine hadronic sections 6 mm thick uranium-niobium (2%) plates are used, while in the coarse hadronic sections 46 mm of copper (CC) and stainless steel plates (EC) are used. The D0 calorimeters are divided into readout cells. The transverse size of the readout cells is comparable to the transverse size

of the showers: $\sim 1-2$ cm for the electromagnetic showers and ~ 10 cm for the hadronic showers.

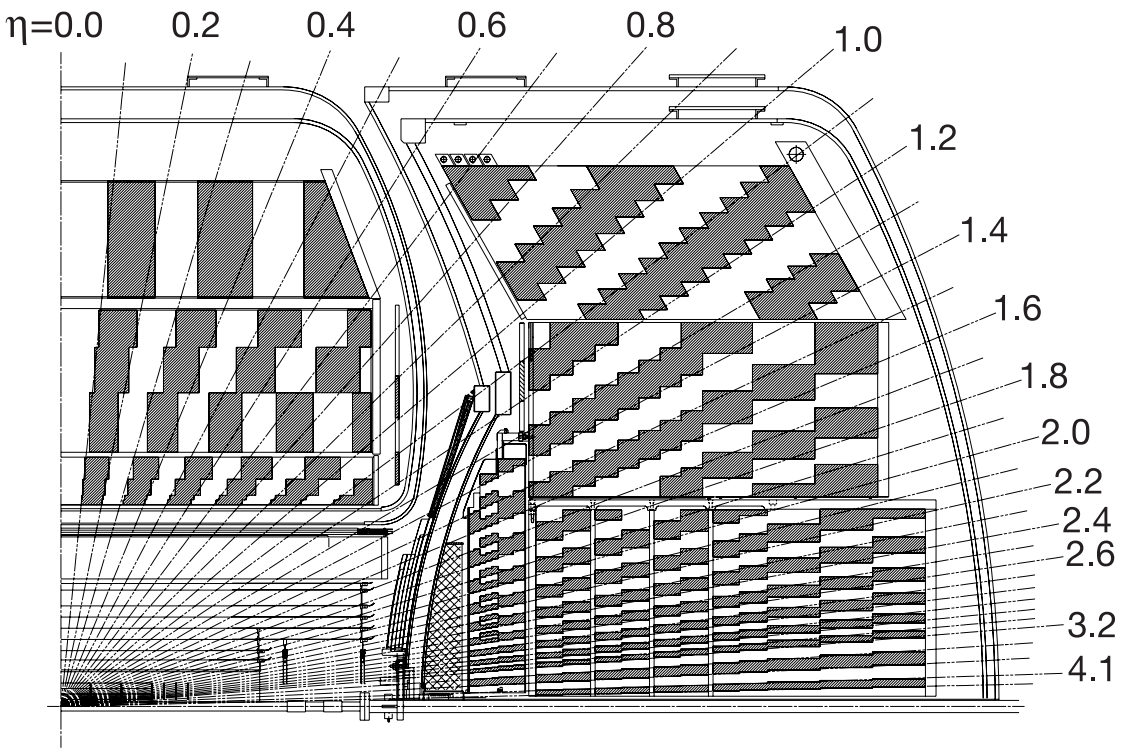

Figure 2.10: Schematic view of a portion of the DØ calorimeters showing the transverse and longitudinal segmentation pattern. The shading indicates groups of cells ganged together for signal readout. The rays indicate pseudorapidity intervals from the center of the detector.

The typical calorimeter cell is shown in figure 2.9. The electric field is established by grounding the metal absorber plate, while the signal boards are connected to positive high voltage (~ 2 kV). The electron drift time across the 2.3 mm liquid-argon gap is approximately 450 ns. Several readout pads at approximately the same η and ϕ are linked together in depth to form a readout cell. The calorimeter readout cells form pseudo-projective towers as shown in figure 2.10, with each tower segmented in depth. The term "pseudo-projective" is used because the centers of cells of increasing shower depth lie on rays projecting from the center of the interaction region, but the cell boundaries are aligned perpendicular to the absorber plates.

The performance of the calorimeter depends on the its thickness and the ma-

terial in front of it. The tracking system and the solenoid magnet have a thickness equivalent to 2-4 radiation lengths (the radiation length is defined as the distance traveled in the material by an electron in which the electron reaches the energy $(1/e)\cdot E$ of the initial energy E). The electromagnetic part of the calorimeter adds up to about 20 radiation lengths. The total thickness of the hadronic calorimeter is about six nuclear interaction lengths in the CC and up to nine in the EC.

The energy resolution of the DØ calorimeter was studied before RunI started in a test beam with pions, electons and muons [22]. However, these energy resolutions are different from the Run II ones. The Run II upgrades introduced modifications that are responsible for energy resolution degradation compared to RunI. The main reasons for this degradation are: the higher beam crossing frequency which leads to a shorter time for the signal charge to be integrated; the additional material from the tracking and calorimeter; and the new amplifiers which were found to increase noise. More detailed information on the DØ Run II jet energy scale is found in Section 3.2.4.

2.2.4 Muon system

The muon system is designed to act both as a muon identification detector and a muon spectrometer. It consists of proportional and mini drift tube detectors, scintillation detectors and toroidal magnets. The central muon system provides coverage for $|\eta| \lesssim 1.0$ and the forward muon system extends this coverage to $|\eta| \lesssim 2.0$.

Muons are minimum ionizing particles. They penetrate the full D0 detector without losing much of their energy and without producing a shower in the calorimeter. Hence, because the calorimeter is big enough to contain the full showers produced, everything that gets to the muon system is most likely a muon. The muon system has one layer of detectors inside the toroid and two outside. The toroid acts effectively as an absorber to stop low energy particles leaking out of the calorimeter.

The central toroid is a square annulus 109 cm thick, with the inner surface at approximately 318 cm from the beam line, and covers the region $|\eta| \lesssim 1$. The two end toroids are located at $454 \leq |z| \leq 610$ cm, each of them having a 183 cm square hole centered on the beamline. The magnet toroids are operated at a current of 1500 A producing a magnetic field of about 1.79 T. This is lower than the RunI field, but in RunII the momentum of the muons is primarily measured in the central tracker.

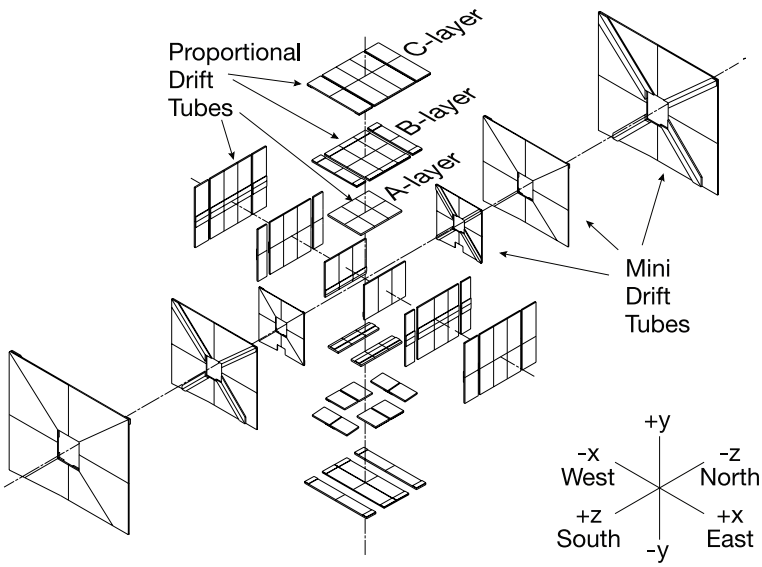

Figure 2.11: Exploded view of the muon wire chambers.

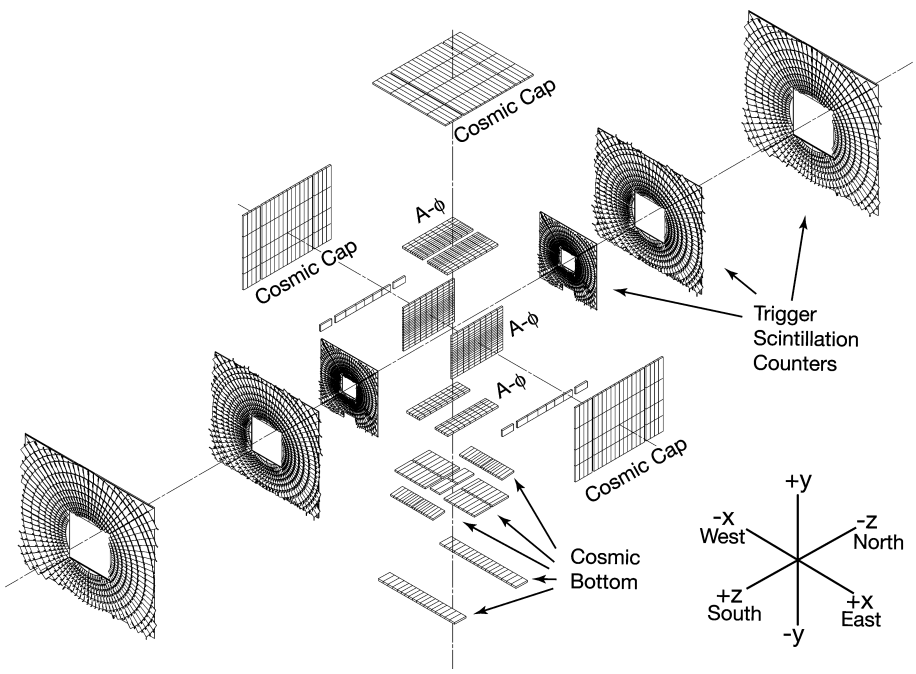

Figure 2.12: Exploded view of the muon scintillation detectors.

Central muon system

The central muon system consists out of the central toroidal magnet, drift chambers, the cosmic cap and bottom scintillation counters, and the $A\phi$ scintillation counters.

The proportional drift tubes (PDTs) are arranged into chambers. PDTs are gas filled containers with an anode wire through the center and cathode pads placed at the top and bottom of the container. When a charged particle traverses the volume it ionizes the gas and gives rise to avalanches of electrons that are read out as signal. There are three layers of chambers: layer A inside the toroid and layer B and C outside the toroid. The distance between layers B and C is bigger than 1 m so a good direction measurement of the muon after the magnet can be made. There are 4 PDT planes in the A layer chambers (except the bottom layer A where there are 3 layers) and 3 in the layer B and C chambers. The structure of all chambers is the same, they differ only in the cell depth (3 or 4 layers) and width (between 14 and 24 PDTs) and their length (between 191 and 579 cm). All PDTs are 10.1 cm wide and 5.5 cm tall. Approximately 55% of the central region is covered by three layers of PDTs; close to 90% is covered by at least two layers. The PDTs are filled with a gas mixture consisting of 84% argon, 8% methane and 8% CF_4. The operating high voltage is 2.3 kV for the pads and 4.7 kV for the wires. In these operating conditions the drift velocity is approximately 10 cm/μs for a maximum drift time of about 500 ns. The readout of PDTs is in pairs and the resolution along the wire direction is between 10 cm and 50 cm depending if the hit is far, respectively, close to the readout end.

The cosmic cap and bottom scintillation counters are installed on the top, sides and bottom of the outer layer of the central PDTs. The cosmic cap consists of 240 counters placed in front of layer C of the PDTs on top and the two sides. The sizes of these scintillation counters are 63.5 cm $\times$ (207 $-$ 287) cm and they are positioned with their width along z and length along ϕ. The cosmic bottom counters are placed outside the bottom C PDT layer or outside layer B where layer C is non-existent. There are 132 of these counters, each 200 cm $\times$40 cm with the short dimension (40 cm) oriented along the ϕ direction, so that each counter covers approximately 4.5° in ϕ.

The $A\phi$ scintillation counters cover the A-layer PDTs and provide a fast detector for identifying muons and for rejecting out-of-time backscatters from the forward direction. The counters also provide the time stamp for low-p_T muons that do not penetrate the toroid and thus do not reach the cosmic cap or the bottom counters. In total there are 630 $A\phi$ counters of three different sizes, such that the segmentation in ϕ is approximately constant and equal to 4.5°, matching the central fiber tracker trigger segmentation.

Forward muon system

The forward muon systems extend the coverage of the central muon system to $|\eta| \lesssim 2.0$ on both sides of the detector. They consist of three layers of MDTs (mini drift tubes) and three layers of scintillation counters. MDTs were chosen for their short electron drift time (below 132 ns), good coordinate resolution (less than 1 mm), radiation hardness, high segmentation and low occupancy. The MDTs are arranged in three layers (A, B and C , with A inside the tororoid and C the outer most layer), each of them divided into eight octants (see Figure 2.11). Each layer consists of three (layer B and C) or four (layer A) planes of tubes mounted along the magnetic field lines (the field shape in the forward toroids is more "square" than "circular"). The entire MDT system contains 48,640 cells. Each cell is 9.4 mm $\times$ 9.4 mm, made out of aluminum with a central 50 μm W-Au wire; the maximum MDT length is 5830 mm in the C layer. The MDT system uses a $CF_4 - CH_4$ (90%-10%) gas mixture. The maximum drift time for tracks that are perpendicular to the detector plane is 40ns and for tracks that are inclined at 45° with respect to the detector plane 60 ns.

The forward scintillation counters are arranged into three layers (A to C) and are installed close to the MDTs. Each layer is divided into octants containing about 96 counters. The ϕ segmentation is 4.5° and matches the CFT trigger sectors (see Section 2.2.6). The η segmentation is 0.12 (0.07) for the first nine inner (last three) rows of counters. The counters are optimized to provide good time resolution and amplitude uniformity for background rejection and high muon detection efficiency.

In the forward region, shielding was installed to reduce background events coming from: i) scattered proton and antiproton fragments that interact with the end of the calorimeter or with the beampipe, ii) proton and antiproton fragments interacting with the Tevatron low-β quadrupole magnets, and iii) beam halo interactions from the tunnel. The position of the shielding can be seen in Figure 2.4. The shielding consists of layers of iron, polyethylene and lead in a steel structure surrounding the beam pipe and the low-β quadrupole magnets. Iron is used as hadronic and electromagnetic absorber, polyethylene is a good absorber of neutrons due to its high hydrogen content and lead is used to absorb gamma rays.

2.2.5 Luminosity monitor

The purpose of the luminosity monitor (LM) is to determine the Tevatron luminosity at the DØ interaction region. This is done by measuring the inelastic $p\bar{p}$ collisions with two arrays of 24 plastic scintillator detectors located at $z = \pm 140$ cm. The plastic scintillator detectors are 15 cm long and are arranged in a disk array. Each of them is read out by a photomultiplier tube. The coverage of the luminosity monitor corresponds to the pseudorapidity range $2.7 < |\eta| < 4.4$. The luminosity

monitor also serves to measure beam halo rates and to make a fast measurement of the z coordinate of the interaction vertex.

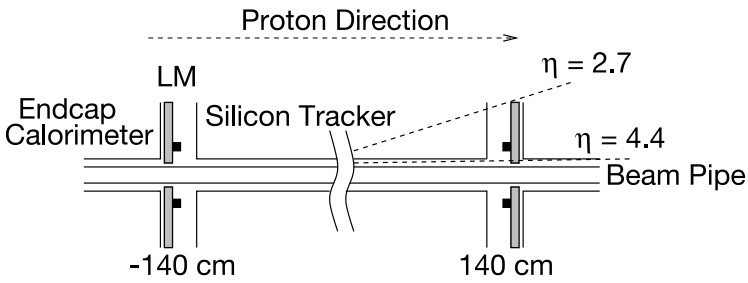

Figure 2.13: Schematic drawing showing the location of the luminosity monitor detector.

The luminosity $\mathcal{L}$ is determined from the average number of inelastic collisions per beam crossing $\bar{N}_{LM}$ measured by the luminosity monitor.

$$\mathcal{L} = \frac{f\bar{N}_{LM}}{\sigma_{LM}} \tag{2.6}$$

where f is the beam crossing frequency and σ_{LM} is the effective cross section for inelastic $p\bar{p}$ collisions at DØ and that takes into account the acceptance and efficiency of the LM detector. The effective cross section σ_{LM} is proportional to the total inelastic cross section $\sigma_{\text{inelastic}}(1.96\text{ TeV}) = 60.7 \pm 2.4$ mb [23, 24]. Since $\bar{N}_{LM}$ is typically greater than one, it is important to account for multiple $p\bar{p}$ collisions per beam crossing. This is done by counting the fraction of beam crossings with no collisions and using Poisson statistics to determine $\bar{N}_{LM}$.

In order to measure the luminosity accurately, it is important to distinguish between $p\bar{p}$ interactions and the beam halo background. The separation between these processes is obtained by making precise time-of-flight measurements of particles traveling at small angles with respect to the beams. First we assume that particles hitting the LM originate from a $p\bar{p}$ interaction and estimate the z coordinate of the interaction vertex z_v from the difference in time of flight:

$$z_v = \frac{c}{2}(t_- - t_+) \tag{2.7}$$

where t_- and t_+ are the times of flight measured for particles hitting the LM detector placed at ± 140 cm. Beam-beam interactions are selected requiring $|z_v| < 100$ cm, which includes nearly all $p\bar{p}$ collisions produced by the Tevatron (the interaction region at DØ is $\sigma_z \approx 30$ cm long). Beam halo particles traveling in the

$\pm z$ direction will have $z_v \approx \mp 140$ cm, and are eliminated by the $|z_v| < 100$ cm requirement.

2.2.6 Trigger and DAQ

The structure of the beams as described in section 2.1 gives rise to bunch crossings with an frequency of 1.7 MHz. During these bunch crossings collisions can occur. However, most of these collisions are not considered of interest and swamp the processes that are studied. In order to increase the signal to background ratio and also to increase the number of events of interest saved by the experiment a three stage event trigger system is used, the stages being named Level 1 (L1) to Level 3 (L3). At each level a fast reconstruction algorithm computes physical meaningful terms (energy deposition patterns, tracks, jets, etc.). The complexity of these terms increases with the trigger level and so does the time necessary to compute them. Each of the three layers reduces the number of events passed to the next level based on the physics terms. The three layers of the trigger reduce the 1.7 MHz of events input to L1 to about 100 Hz L3 output frequency. These events are recorded for offline reconstruction. An overview of the DØ trigger and data acquisition systems is shown in Figure 2.14.

The trigger system is closely integrated with the readout of data. Each event that satisfies successive L1 and L2 triggers is fully digitized, and all of the data blocks of the individual subdetectors for the event are transferred to L3. The L1 and L2 buffers play an important role in minimizing the experiment's deadtime by providing a FIFO storage to hold event data awaiting a L2 decision or awaiting transfer to L3.

The overall coordination and control of DØ triggering is handled by the COOR (main run control and detector configuration) package. COOR interacts directly with the trigger framework (for L1 and L2 triggers) and with the DAQ supervising system (in charge of L3 coordination). COOR receives requests from users (via text-based commands) to configure the detector, to start or stop runs and sends the necessary commands to the rest of the system to carry out the requests.

Level 1 trigger

The Level 1 trigger is implemented in specialized hardware and examines every event for interesting features. The L1 trigger receives data from all detector subsystems described above except the SMT. All events awaiting a L1 trigger decision are pipelined and thus make minimal contribution to the deadtime. In order to participate in the trigger decision, the L1 trigger decision must arrive at the trigger framework in 3.5 μs or less. The rate of L1 trigger accepts is limited by the maximum readout rates of the participating subsystems and by a desire to minimize

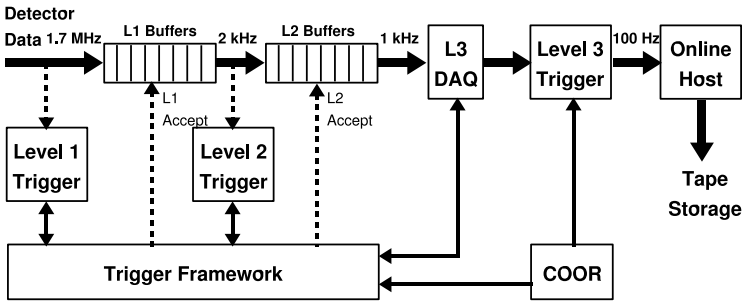

Figure 2.14: Overview of the DØ trigger and acquisition systems. The maximum output rate for each level is shown in the image.

the deadtime associated with the readout.

The core of the L1 trigger is the trigger framework (TFW) to which all L1 triggers report. The TFW gathers digital information from each of the specific L1 trigger devices and chooses whether a particular event is to be accepted for further examination. In addition, it coordinates various vetoes that can inhibit triggers, provides the prescaling of triggers too copious to pass on without rate reduction, correlates the trigger and readout functions, manages the communications tasks with the front-end electronics, and provides a large number of scalers that allow accounting of trigger frequencies and deadtimes. The TFW receives 256 "AND-OR" terms from various parts of the detector, which can be combined by programmable hardware into 128 triggers. The OR of all these 128 triggers determines whether a given crossing had a valid L1 trigger.

The L1CTT (Level 1 Central Track Trigger) reconstructs the trajectories of charged particles using fast discriminator data provided by the central fiber tracker detector and the central and forward preshower detector. The three detectors are divided into 80 ϕ sectors of 4.5° and the hits in each sector are compared with approximately 20,000 predefined track equations. There are 4 intervals for track searches with thresholds of 1.5, 3, 5, and 10 GeV. Tracks from each sector are sent to the L1Muon where the tracks are matched to hits in the muon system.

The L1Muon (L1 muon trigger) looks for patterns consistent with muons using hits from muon wire chambers, muon scintillation counters and tracks coming from the L1CTT. Field programmable gate arrays are used to perform combinatorial logic on roughly 60,000 muon channels and up to 480 tracks from the L1CTT for every bunch crossing. The muon system (and also L1Muon) is divided into north, south and central regions. Each region is further divided into eight ϕ octants. The L1Muon matches central tracks to muon scintillator hits and muon track stubs (scintillator confirmed tracks) in wire chambers. Timing information in the

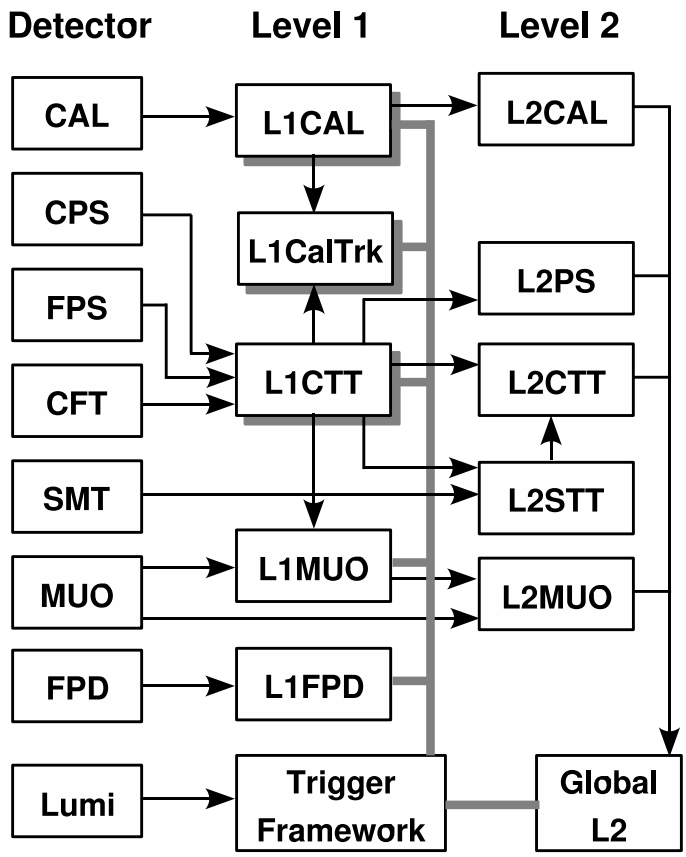

Figure 2.15: Block diagram of the DØ L1 and L2 trigger systems. The arrows show the flow of trigger-related data.

scintillators is also used to reject cosmics, the requirement being that the time stamp of a hit in the scintillator be within a window with respect to the beam crossing. In total L1Muon can form 256 trigger terms and sends 32 of them to the TFW.

The L1Cal (Level 1 calorimeter trigger) [25] inputs consist of electromagnetic (EM) and hadronic (H) trigger tower energies made up from analog electronic sums in depth and transverse coordinates ($\Delta\eta \times \Delta\phi = 0.2 \times 0.2$) in the calorimeter. There are 1280 EM towers and 1280 H towers: forty slices in η covering the region $|\eta| < 4$, and thirty-two slices in ϕ covering the full 2π azimuthal angular range. Due to overlapping collisions, which complicate the forward environment, only the region $|\eta|<3.2$ is used for triggering. Local maxima are searched for using a sliding window algorithm [25]. The algorithm looks for regions of interest in 2×2 windows for H towers and 1×1 towers for the EM (trigger tower clusters) in $\eta \times \phi$ and

then the jet object is defined by the E_T sum in a 4×4 window for the hadronic jets and a 2×1 towers window for EM objects around the trigger tower clusters. When the E_T sum is over a defined threshold a triggering occurs.

The L1CalTrk is functionally similar to L1Muon and it matches L1CTT tracks over a certain range of momenta and isolation with L1Cal objets. The matching has an important role in reducing the trigger rates.

Level 2 trigger

The Level 2 trigger gets inputs from the L1 Trigger, the detectors included in the L1 trigger decision and from the SMT. It is the first layer of triggering that tests for correlations in physics signatures across detector subsystems. The L2 trigger system was handles input rates up to 2 kHz with a maximum accept rate of 1 kHz. The L2 preprocessors (in general one for each detector subsystem) collect data from the front-ends and L1 trigger system when the L1 trigger fires a pass command. The L2 preprocessors analyze the data received to form physics objects, which are examined for event wide correlations. All this information is passed to the L2Global processor that, based on the 128 L1 selection bits and additional L2 scripts, makes a trigger decision. All events that pass L2 are tagged for full readout and further analysis in the L3 trigger.

Level 3 trigger

The Level 3 trigger (L3) consists of a computer farm of about 300 commercial PCs. Each event that passes L2 is fully read out and distributed to one of the L3 PCs (nodes). A simplified version of the offline reconstruction software is run on the L3 farm nodes and each event is fully reconstructed into physics objects. L3 decreases the 1 kHz input rate from L2 to about 100 Hz, the maximum rate for recording events.

L3 decisions are based on complete physics objects as well as on the relationships between such objects (such as the rapidity or azimuthal angle separating physics objects or their invariant mass). Candidate physics objects, or relations between them, are generated by object-specific software algorithms (filter tools). Tools perform the bulk of the work: unpacking raw data, locating hits, forming clusters, applying calibration, reconstructing electrons, muons, taus, jets, vertices and missing transverse momentum (or energy). Sets of programmable algorithm parameters are input to the tools via the programmable trigger list. These sets define the physics objects precisely, for example the reference sets can be the jet cone size for a jet reconstruction algorithm, electromagnetic fraction for electron identification and so on.

Individual calls to tools are made by filters that define the specific selection

criteria employed by a tool or imposed on its result (for example the requirement for two jets, each with p_T greater than 30 GeV/c). The trigger list programming includes blocks of filter scripts that specify one or more filters and that define the L3 trigger conditions for each L3 trigger or filter bit. Each L3 filter script is associated with an L2 bit, multiple L3 scripts may be associated with each L2 bit. Failure to pass an individual filter terminates the execution of the script. Only when all filters in a script are satisfied, is the trigger satisfied and the event sent to the host cluster to be recorded.

In selecting the data used for this thesis no explicit trigger is required, but due to the requirement of two muons in the event most of the events considered would have passed a single muon trigger or a di-muon trigger. These triggers are formed out of L1, L2 and L3 requirements. At L1 muon triggers use the scintillator and wire hits and sometimes it is required to be matched with a CTT track. The di-muon triggers require the two muon candidates at L1 to be within $|\eta| < 2.0$ while the single muon triggers require a candidate within $|\eta|<1.6$. At L2 some basic cuts on the muon quality are made and at L3 the local muon information is refined and the match with a central track is considered.

The recorded data are stored on tapes. All information in the event is stored as raw data and then is reconstructed by an offline reconstruction process that is described in the next chapter.

Chapter 3

Object identification and reconstruction efficiencies

After an event is written to tape it undergoes a full offline event reconstruction. The basic reconstructed data (tracks, calorimeter clusters, etc) are used to reconstruct physics objects, such as muons, jets, etc in the first analysis step. Besides the recorded data also simulated events go through the same reconstruction algorithm.

In this chapter the algorithms used to construct some of the physics objects and their efficiencies are described in detail.

3.1 Muons

For this analysis one of the most important objects is the muon, at least two of them being required in the final state. In this section the characteristics of the muon reconstruction are described.

Identification

At the base of muon identification stand hits in the central and forward muon drift chambers and scintillators. Track segments are fitted using the drift chamber hits in each separate layer and then these 'stubs' are interpolated between two or three layers of the muon system to form a local muon candidate. The timing information is used for rejecting out-of-time background, like cosmic muons. Additionally, the quality of the muon can be gauged by the existence of a matching track in the central tracker or the lack of matching energy deposit in the calorimeter. Based on this, track isolation and calorimeter isolation criteria can be defined for each muon. In DØ terminology there are 3 types of predefined muons based on their quality: "tight", "medium" and "loose". In this analysis only the "loose" criterion is used for muons.

A "loose" muon candidate with a central track match is required to satisfy at least one of the following criteria:

- at least one A layer scintillator hit and at least two A layer wire hits.
- at least one BC layer scintillator hit and at least two BC layer wire hits;

A "loose" muon candidate without a central track match is required to pass at least two of the following criteria:

- at least two A layer wire hits and at least one A layer scintillator hit;
- at least two BC layer wire hits;
- at least one BC layer scintillator hit.

A detailed description of the muon identification (ID) can be found in [26]. The loose muon ID efficiency can be seen in Figure 3.1; the average muon ID efficiency for loose muons over the full η range ($|\eta| < 2.1$) is 92.1% [27].

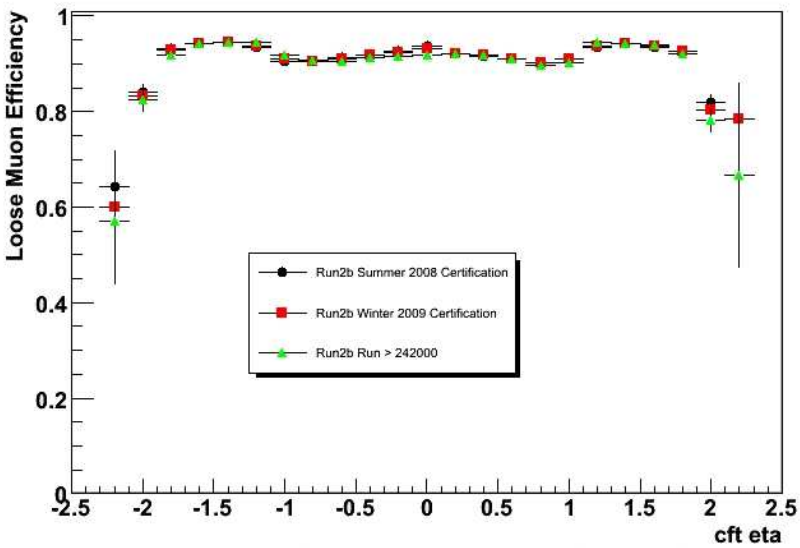

Figure 3.1: Loose muon ID efficiency as a function of the rapidity of the muon in the CFT [27].

3.1.1 Efficiency

The muon efficiencies are estimated using a "tag and probe" method [27, 28]. For this, $Z/\gamma^* \rightarrow \mu^+\mu^-$ events are selected from data. The Z boson production is a well understood and measured process. This type of event is very well suited for efficiency studies due to its clear signature and small background from other processes, hence giving meaningful comparison between simulated MC and real data.

Events with two muons are required for the "tag and probe" method. The "tag" muon should satisfy tight selection criteria. These selection criteria are: muon isolation, track matching, calorimeter isolation, etc. Efficiencies can then be determined by "probing" that there is a second muon in the event passing the looser selection criteria. If also the probe muon passes the "tag" criteria the role of the two muons can be reversed. The efficiency is then given by the number of successful "probes" and the number of "tags":

$$\epsilon = \frac{2 \times N_{tag+tag} + N_{tag+probe}}{2 \times N_{tag+tag} + N_{tag+pass} + N_{tag+fail}}, \tag{3.1}$$

where *tag* and *pass* mean a muon passing the "tag" and "probe" criteria; *fail* corresponds to failing both criteria and *probe* represents the number of probed muons. The tag and probe criteria are usually asymmetric, the probe requirement being usually softer than the tag criteria. In case the tag and probe criteria are identical, the term "$tag + probe$" disappears in the equation above.

The efficiency is measured for a data sample and for a $Z/\gamma^* \rightarrow \mu^+\mu^-$ Monte Carlo sample. Care is taken to avoid biases. These biases could arise if the event was recorded on a trigger that depends on the quantity studied. For example measuring isolation of muons with data triggered on a trigger that included a muon isolation term would push the measured isolation towards higher values. In order to avoid these possible biases the events are selected by having fired a completely independent trigger or by matching the *tag* muon with the trigger requirement.

3.1.2 Muon momentum smearing

Because the measured resolution of the muon transverse momentum in data is different than the one expected from MC simulations, the p_T of each muon candidate in MC events is smeared to obtain better agreement. In order to have better agreement of the MC $Z/\gamma^* \rightarrow \mu^+\mu^-$ distribution in p_T to the one reconstructed from $Z/\gamma^* \rightarrow \mu^+\mu^-$ data events, the following transformation is applied to the initial MC muon p_T:

$$\frac{1}{p_T} \rightarrow \frac{1}{p_T} + AG_1 + \frac{B\sqrt{\cosh\eta}}{p_T}G_2. \tag{3.2}$$

muon type	$A \times 10^{-3}$ [GeV^{-1}]	$B \times 10^{-2}$
μ with SMT hits and $\lvert\eta\rvert < 1.6$	$1.7 \pm 0.1 \pm 0.1$	$1.5 \pm 0.2 \pm 0.4$
μ with SMT hits and $\lvert\eta\rvert > 1.6$	$2.6 \pm 0.3 \pm 0.4$	$1.8 \pm 0.6 \pm 0.7$
μ without SMT hit	$2.5 \pm 0.4 \pm 0.5$	$1.7 \pm 1.0 \pm 1.4$

Table 3.1: Muon momentum smearing coefficients. The statistical and systematic error on the parameters are given in this order.

The smearing is taken dependent of the muon pseudorapidity to account for the multiple scattering dependance on the material crossed by the muon. The two independent variables G_1 and G_2 are considered to have a Gaussian distribution with a width of 1 and mean 0. This smearing introduces an additional resolution term

$$\frac{\sigma(1/p_T)}{1/p_T} = \sqrt{A^2 p_T^2 + B^2 \cosh\eta}. \tag{3.3}$$

The values A and B are given in Table 3.1. For more details see [29].

3.2 Jets

3.2.1 Jet finding algorithm

The hadronization of particles gives rise to jets. Jets are defined as clusters of particles or energy deposits.

Jets are reconstructed in DØ using the "Improved Legacy Cone Algorithm". This algorithm has 3 steps as discussed in some more detail below: clustering, addition of midpoints, and merging and splitting [30]. The algorithm can be carried out using either Monte Carlo particles, leading to "particle jets", or using energy deposits in the detector leading to "detector jets". The jet is enclosed in a cone that has radius R_{cone} in the $\eta \times \phi$ plane.

The jet reconstruction algorithm starts with a number of "seeds". The seeds correspond to the most energetic particles in the event. As seeds, calorimeter towers over a threshold energy are used. A calorimeter tower (as explained in Section 2.2.3) consists of all calorimeter cells having the same $\eta \times \phi$ coordinates and covers a space of $\Delta\eta \times \Delta\phi = 0.1 \times 0.1$. E_T-weighted centroids are computed for each of the seed cones and are used as centers for new cones.[1] The iteration

[1] E_T is defined as $E \times \sin\theta$. In order to determine θ vertex coordinates are needed, because of the long interaction region. Hence in the full DØ reconstruction algorithm, track and vertex

cone size R_{cone}	0.5
seed threshold p_T	1.0 GeV
split merge fraction f	0.5
jet threshold E_T	8 GeV

Table 3.2: Cone jet algorithm specifications.

is continued until the jet axis corresponds with the E_T-weighted centroid. These stable jets are named protojets.

Seed based jet algorithms suffer from some problems in the reconstruction of jets. A jet algorithm should be collinear safe and infrared safe. Problems of collinear safety arise when the energy of one particle is shared between two detector towers. In this case these two towers might both fail to pass the request to become seed for a jet even if the original particle would pass this requirement. Also in some cases the ordering of the seeds can be affected by this and hence the cone algorithm can fail to reconstruct all the particles in a jet. Using seed thresholds of E_T>1 GeV the DØ jet algorithm was found to be fully collinear safe for jets with E_T>20 GeV.

Infrared safe problems arise because only towers that pass the seed energy limit are taken into account. In principle soft radiation between two particles belonging to a single jet can be below this threshold energy and not taken into account. Hence, instead of a single jet being reconstructed the algorithm will reconstruct two jets. This is overcome by adding a starting seed for clustering at the mid-point position of two protojets that are separated by less than $\Delta R < 2.0 \times R_{cone}$.

The protojets can still share calorimeter towers between them. A final procedure recombines or splits these protojets. First the protojets are arranged in descending E_T and tested for calorimeters towers shared with other jets. Protojets sharing one or more towers are merged if the shared E_T is larger than a given fraction f of the total energy of the lowest energy jet. If the shared E_T is smaller than f, the shared towers are assigned to the closest protojet. The procedure is repetead with the newly obtained protojets until there is no more overlapping of the protojets. Once all the jets are final the jets falling below a certain E_T threshold are discarded. The parameters for the cone algorithm used in DØ are listed in Table 3.2.

reconstruction are performed first.

3.2.2 Noise reduction

In order to suppress calorimeter noise the T42 algorithm is implemented [31, 32, 33]. The T42 algorithm (Threshold 4–2 σ) rejects all calorimeter cells with less then 4σ energy above threshold, or with less than 2σ if there is an adjacent cell that has at least 4σ energy above threshold. Between 30% and 60% of the cells in an event are rejected by this algorithm. While in the central region the number of rejected cells corresponds to the expected number of noisy cells, in the forward region the number of rejected cells is higher, which is due to pile-up effects. This algorithm is applied before jet clustering.

3.2.3 Jet identification

The jets found using the jet finding algorithm are required to pass further quality criteria in order to remove fake jets:

- The total number of calorimeter towers that contain 90% of a jet's energy has to be larger than one, to reduce noise jets coming from a single hot cell;
- The ratio of the highest to next-to-highest E_T cell has to be smaller than 10 in order to remove jets clustered from hot cells.
- Reduction of electromagnetic and noise-like jets is obtained by requiring that the fraction of the energy deposited in the electromagnetic calorimeter is between 5% and 95%.
- Because of the higher noise in the coarse hadronic layers compared to the other layers of the calorimeter, the energy fraction in this layer is required to be less than 40% of the jet energy.

3.2.4 Jet energy scale

The previous section presented the algorithm for jet reconstruction. Each jet obtained has a measured energies, E_{meas}, which consists of the sum of all energy recorded in calorimeter cells within ΔR of the jet axis (with the specification that the cells have to pass the requirements mentioned above). This measured energy is not exactly the energy of the initial particle that produced the jet and a calibration is needed. This calibration is provided by the Jet Energy Scale correction [34].

The correction from the measured energy of the jet E_{meas} to the original particle energy E_{corr} is of the form:

$$E_{corr} = \frac{E_{meas} - O}{R \times S}, \tag{3.4}$$

where O is the offset energy, R the calorimeter response and S the showering correction.

The energy offset term O represents the additional energy in the calorimeter cells due to the underlying event, energy pile-up in the calorimeter and noise from the detector. The magnitude of the energy offset O is determined in "minimum bias" events, where the trigger is based on the luminosity detectors and no extra triggering requirements.

The calorimeter response R can vary for different partons or different calorimeter regions due to dead material, inhomogeneous instrumentation and non-linear response to the particle energies. The calorimeter response is determined by the examination of QCD Compton events (for example $qg \rightarrow q\gamma$). The photon's electromagnetic energy can be reconstructed with high accuracy. This can be achieved due to the electromagnetic energy scale calibration in the $Z \rightarrow e^+e^-$ peak. In the QCD Compton events the transverse jet energy is estimated as being equal with the transverse photon energy, in events where the jet and photon are back to back.

Showering corrections S take into account the fact that some of the particles produced by the initial parton can be bent out of the jet cone due to the interaction with the magnetic field and hence their energies are not taken into consideration.

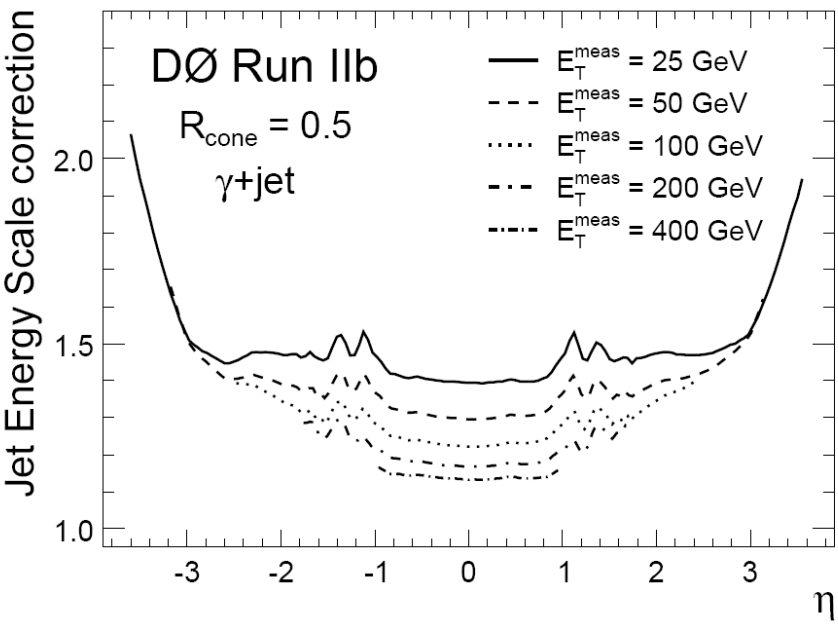

Figure 3.2: Jet energy scale corrections as a function of the jet pseudorapidity.

The JES corrections are dependent on the p_T of the initial parton and detector η. Due to differences between MC and data a different MC JES correction is applied to MC events. The JES corrections as a function of η can se seen in Figure 3.2.

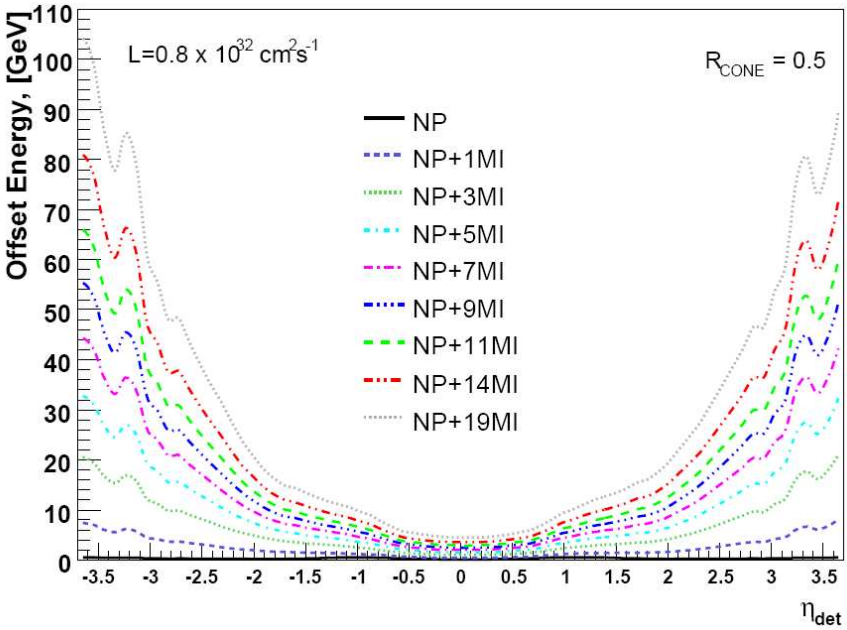

Figure 3.3: Offset energy corrections as a function of the jet pseudorapidity. NP stands for contributions for noise and pile-up and MI stands for multiple interactions.

3.2.5 Jet energy resolution

The jet energy resolution (JER) is determined in di-jet events where the two jets are back-to-back ($|\Delta\phi - \pi| < 5$ degrees). The jet p_T resolution is directly related to the asymmetry resolution of the two jets $|A| = |p_T^{\text{jet1}} - p_T^{\text{jet2}}|/(p_T^{\text{jet1}} + p_T^{\text{jet2}})$. The jet resolution is fitted with the following function [35]:

$$\frac{\sigma_{p_T}}{p_T} = \sqrt{\left(\frac{N}{p_T}\right)^2 + \left(\frac{S}{\sqrt{p_T}}\right)^2 + C^2}, \tag{3.5}$$

where N, S and C are the contributions from noise, statistical sampling fluctuations and, respectively, calibration errors.

The jet energy resolutions as a function of jet p_T as well the parameters N, S and C can be seen in Figure 3.4.

3.2.6 Shifting, smearing and removing of simulated jets - JSSR

The jet shifting, smearing and removing (JSSR) procedure [36] is applied only to MC events and it simulates the biases from jet reconstruction inefficiency and

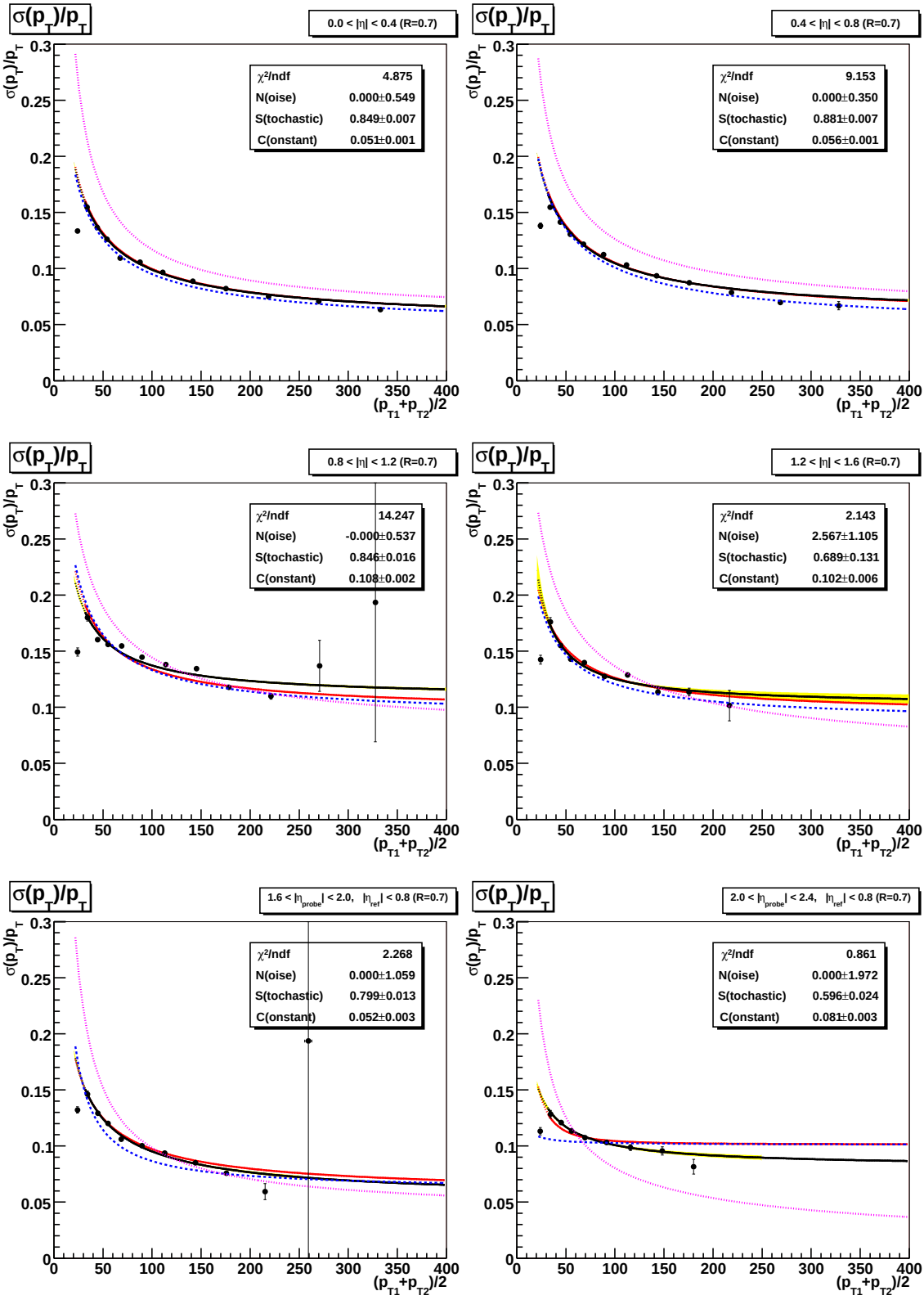

Figure 3.4: Jet resolution in different pseudorapidity bins after soft radiation corrections and particle imbalance corrections, for jets with cone size $R = 0.7$ is shown in black [35]. Statistical error bands (yellow) are shown as well.

resolution between data and MC. JSSR smears MC jets using a gaussian width $\sigma^2_{Smear} = \sigma^2_{Data} - \sigma^2_{MC}$ and then shifts their energies. Also jets are randomly removed to reproduce resolution and reconstruction efficiencies in data.

3.3 Missing $\boldsymbol{E_T}$

Particles that do not interact with the detector (such as neutrinos) do not leave directly any information. However, this information can be accessed indirectly via the missing transverse energy. The Tevatron being a hadronic collider, the conservation of energy and momentum can be exploited only in the transverse plane. In the beam direction conservation of energy and momenta cannot be exploited as the interacting partons sample their energy from the incoming hadron based on the parton distribution function. The transverse missing energy is calculated from the negative vector sum of the transverse energy contents of all calorimeter cells with an energy content of at least 100 MeV over the individual cells threshold. If muons are reconstructed in the event, their contribution is added to the visible energy in the calorimeter. A detailed description of the missing transverse energy calculation can be found in [37, 38].

3.4 Tracks

The hits in the tracking detector are used to reconstruct tracks. For the reconstruction two track finding algorithms are used and one algorithm that propagates tracks through the full detector to reconstruct the track parameters.

One of the track finding algorithms starts the search from seeds of 3 hits in the SMT or CFT [39, 40]. These hits are then propagated through the SMT and CFT and at each layer a new seed track is created for every hit within the predicted trajectory. The other algorithm is based on the Hough transform to find tracks [41]. In this way a collection of candidate tracks is obtained. All the candidate tracks that pass minimum quality criteria are kept and ranked based on these quality criteria. These tracks are then fitted using the third algorithm (based on a Kalman Track Fitter) and in this step in the propagation of the tracks variations in the magnetic field, energy loss and multiple scattering are taken into account [42, 43].

3.5 Primary Vertices

There are two kinds of vertices that are of interest. Primary vertices correspond to the hard scatter in the event and secondary vertices correspond to the decays

of long lived particles.

All the tracks in the event passing some quality criteria are extrapolated back to a common point of origin along the z-axis. The Adaptive Primary Vertex algorithm [44] is used to find these points that constitute the primary vertices. In order to minimize the contribution of long lived particles decay tracks to the primary vertex, the track errors are re-weighted according to their χ^2 contributions to the vertex. All tracks are fitted using the Kalman Filter algorithm with the constraint that they belong to the same primary vertex and the weight of each track in this fitting is initially set to 1. At the following iterations the track is weighted based on its contribution to the vertex fit χ^2. This algorithm is repeated until convergence of the tracks weights is achieved.

In order to separate the primary vertex from all the vertices identified in the procedure above, a probabilistic approach is used [45]. Because of the differences in the p_T spectra of tracks originating from the primary vertex or a minimum bias vertex, a probability that a vertex comes from a minimum bias vertex can be assigned.

3.6 B-tagging

Secondary Vertices are produced by the decay of long lived particles. The hadronization of B-hadrons produces secondary vertices which play an important role in finding the jets that correspond to b-quark decays. The search for secondary vertices is performed within the track jets. At first, all possible 2 track (tracks corresponding to the primary vertex are discarded in this procedure) vertices are considered and then tracks are added to these candidate vertices with an algorithm that takes into account the increase in the χ^2 value of the vertex fit due to the addition of the new track. A full description of the secondary vertex finding procedure can be found in [46, 47].

The presence of these secondary vertices and the fact that the tracks in this vertices do not point to the primary vertex when extrapolated back can be used to evaluate the b-likeliness of jets. This process is called b-tagging. Within DØ several b-tagging algorithms were developed: the jet lifetime impact parameter tagger (JLIP) [48], the counting signed impact parameter tagger (CSIP) [49] and the secondary vertex tagger (SVT) [50]. The JLIP tagger combines all track impact parameters to estimate the probability that all tracks in a jet originated from a primary vertex. The CSIP tagger counts the number of tracks in a jet with a large impact parameter significance with respect to the primary vertex. The SVT uses tracks with large impact parameter significance to reconstruct secondary vertices. Outputs of these algorithms are fed into a more powerful tool: a Neural Network based b-tagger [51].

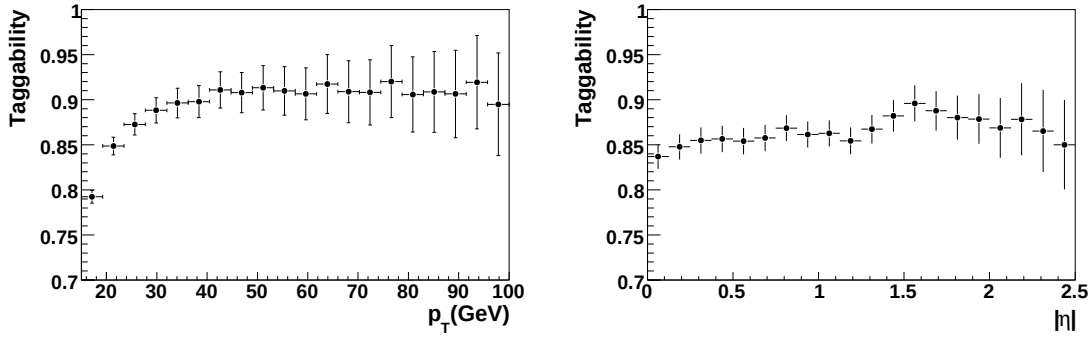

Figure 3.5: Jet taggability as a function of the jet p_T and $|\eta|$.

Track jets are clustered from tracks. In DØ only tracks that have at least 2 SMT hits are considered for track jets. A track seed is considered that has p_T>1 GeV and the algorithm searches for tracks that are within 0.5 in ΔR with respect to the cone centroid. A track jet has to have at least two tracks with p_T>0.5 GeV. Track jets are used to reduce the number of fake jets due to calorimeter noise by requiring that calorimeter jets match a track jet and are also used in finding secondary vertices.

In order to be considered for b-tagging jets have to be taggable, that is to be matched with a track jet within a distance ΔR<0.5. Taggability is introduced because all algorithms described before are based on tracks and vertices present within the considered jet. Also the introduction of taggability introduces a separation between tracking and vertexing efficiencies and the efficiencies of the tagging algorithms. All further b-tagging algorithm efficiencies refer to taggable jets. The taggability of jets in data can be seen in Figure 3.5.

The neural network (NN) tagger combines the following seven input variables:

- the decay length significance of the secondary vertex selected by the tagger (if there are more secondary vertices present in a track jet the neural network tagger select the one with the highest impact parameter significance),
- the weighted combination of the impact parameter significances of all the tracks in the jet as calculated by the CSIP algorithm,
- the JLIP probability that all the tracks in the jet originated from the primary vertex,
- the χ^2/d.o.f of the fit constraining all the tracks in the jet to the selected secondary vertex,
- the number of tracks used by the SVT algorithm to reconstruct the selected secondary vertex,

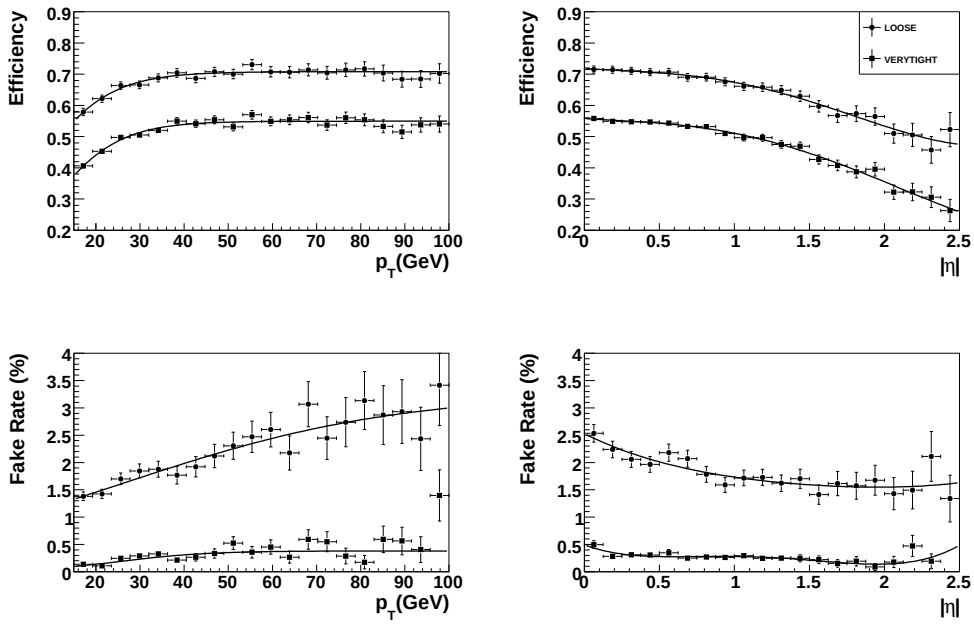

Figure 3.6: Efficiencies and fake rates for the Loose and Very Tight NN operating points as a function of the jet p_T and $|\eta|$ [52].

- the invariant mass of the tracks the selected secondary vertex,
- the number of secondary vertices found by the SVT algorithm within a cone of ΔR<0.5 around the jet.

The NN tagger was trained on $b\bar{b}$ and QCD di-jet MC events (see Section 4.2). The efficiency of the NN tagger was measured in data, in a sample with jets containing muons and scaled to be applicable to inclusive jet samples using a MC correction factor [52]. Tag Rate Functions (TRFs) give the probability to tag b-jets, c-jets as well as the fake rate (the probability to tag a jet not coming from heavy quarks). The TRFs are parameterized as a function of the jet transverse momentum p_T and pseudorapidity η. Twelve operating points of the NN tagger are defined based on cuts on the NN tagger output.

In this analysis two operating points were used:

Loose with a NN output cut of 0.45,

Very Tight with a NN output cut of 0.85.

The performance of the tagger for the Loose and Very Tight operating points can be seen in Figure 3.6. The fit function used is the same as the one used for deriving the TRFs [51].

Chapter 4

Event selection and Monte Carlo description

In this chapter the selection of events from the data recorded is presented. Also the preselection of the simulated events and corrections applied to them are presented. We end this chapter presenting the procedure for splitting the sample we selected into two orthogonal samples based on the b-tagged jet multiplicities.

4.1 Data

The data for this analysis were collected with the DØ detector between July 2006 and December 2008. The data are selected from a subset of the full dataset, where 2 muons with $p_T > 10$ GeV are required in the event. There is no explicit trigger required as we wanted to retain the highest possible efficiency for the signal. The data is filtered by the CafeDataQualityProcessor [53] using definition `dq_defs/2008-12-11`, which removes bad runs and luminosity blocks based on the quality definitions of the SMT, CFT, Calorimeter and Muon groups. After this data quality selection the total luminosity is estimated to be 3.1 ± 0.2 fb^{-1}. The luminosity measurement is performed using the standard luminosity measurement tool on an unprescaled trigger. In the determination of the luminosity the same data quality definition was used.

4.2 Monte Carlo

Data events are simulated using Monte Carlo (MC) simulations. The MC simulation includes the simulation of the hard scatter, initial state radiation, final state radiation, hadronization. The two generators used for the analysis presented in this thesis are PYTHIA [54] and ALPGEN [55]. PYTHIA generates the hard

scatter using a leading order (LO) generator and uses parton shower modeling in order to account for radiation in the final state. The parton showering includes the real corrections to the Next to Leading Order cross section and hence the total cross section computed by PYTHIA is a Leading Log (LL) cross section. The parton showering provides a good simulation of the jet structure, but the modeling of multi-jet events is not very good. ALPGEN has a better modeling of multi-jet evens as it is a matrix element LO generator. Because ALPGEN lacks a good description of the underlying event and the jet structure it is interfaced with PYTHIA for the parton shower and hadronization modeling. In order to avoid double counting of ALPGEN interfaced with PYTHIA events the MLM Matching Scheme [56] is used to eliminate events in which partons generated in the hard scatter are not matched with jets. The DØ MC produced with PYTHIA use the CTEQ6L1 [57] parton distribution functions (PDF's) and "Tune A" for the underlying event [58].

All simulated events are processed through the DØ detector simulation `d0gstar` [59] based on the detector material simulation package GEANT3 [60]. Then these events are passed through the electronics simulation `d0sim` and after this stage they are treated in offline reconstruction in the same way as real data events.

The Z+jets and $t\bar{t}$ backgrounds are simulated using ALPGEN for the hard scatter and then the simulated event is interfaced to PYTHIA for the hadronization and showering part. The WW, WZ and ZZ backgrounds together with the ZH signal are simulated by PYTHIA. The background Monte Carlo samples considered and the number of events used are given in Table 4.1.

Because the ALPGEN+PYTHIA samples used are generated in bins of heavy and light parton multiplicity, a flavor skimming procedure was used to insure that the Z+nlp sample contains only light (u,d,s) quark jets, the Z+cc sample contains only c-quark jets coming from the hard interaction and the Z+bb sample contains only b-quark jets coming from the hard interaction. In the following we will call Z+bb and Z+cc the Z+HF (Heavy Flavor) sample, the Z+nlp the Z+jets sample, and WW, WZ and ZZ the diboson sample.

4.3 Event selection

To keep a high efficiency for the signal events selection, the criteria for selecting events are kept as loose as possible. The motivation for this is not to lose signal and to let the Boosted Decision Trees, which will be discussed in the next chapter, make optimal use of all information available.

First, we ask for events with at least two muons, as from them we would later construct a Z boson candidate. The selection criteria for these two muons are as follows:

Process	Mass(GeV)	$\sigma\times$ BR(pb)	Generator	Events
$Z/\gamma^* + 0lp \to \mu\mu$	>15GeV	472.873	ALPGEN+PYTHIA	3655227
$Z/\gamma^* + 1lp \to \mu\mu$	>15GeV	81.586	ALPGEN+PYTHIA	1577609
$Z/\gamma^* + 2lp \to \mu\mu$	>15GeV	20.1124	ALPGEN+PYTHIA	1157743
$Z/\gamma^* + 3lp \to \mu\mu$	>15GeV	5.9134	ALPGEN+PYTHIA	1003145
$Z/\gamma^* + 2b + 0lp \to \mu\mu$	>15GeV	0.92994	ALPGEN+PYTHIA	637274
$Z/\gamma^* + 2b + 1lp \to \mu\mu$	>15GeV	0.39118	ALPGEN+PYTHIA	416002
$rmZ/\gamma^* + 2b + 2lp \to \mu\mu$	>15GeV	0.11792	ALPGEN+PYTHIA	371570
$Z/\gamma^* + 2c + 0lp \to \mu\mu$	>15GeV	5.08442	ALPGEN+PYTHIA	638726
$Z/\gamma^* + 2c + 1lp \to \mu\mu$	>15GeV	1.50593	ALPGEN+PYTHIA	497408
$Z/\gamma^* + 2c + 2lp \to \mu\mu$	>15GeV	0.44469	ALPGEN+PYTHIA	374148
$ZZ \to 2j2l$		0.226	PYTHIA	105325
$WZ \to 2j2l$		0.275	PYTHIA	273344
WW (inclusive)		12.35	PYTHIA	675814
$tt \to 2b2l2\nu + nlp$		0.54	ALPGEN+PYTHIA	1483272
$ZH \to llbb$	100	0.0137	PYTHIA	308876
$ZH \to llbb$	105	0.0116	PYTHIA	270059
$ZH \to llbb$	110	0.0096	PYTHIA	309248
$ZH \to llbb$	115	0.00797	PYTHIA	270624
$ZH \to llbb$	120	0.00653	PYTHIA	311331
$ZH \to llbb$	125	0.00501	PYTHIA	270488
$ZH \to llbb$	130	0.00375	PYTHIA	311184
$ZH \to llbb$	135	0.00274	PYTHIA	270588
$ZH \to llbb$	140	0.00188	PYTHIA	309076
$ZH \to llbb$	145	0.00123	PYTHIA	270064
$ZH \to llbb$	150	0.00075	PYTHIA	306021

Table 4.1: Monte Carlo samples and their corresponding cross sections. Here l stands for any of the charged leptons e, μ, τ and lp stands for "light-partons" and indicates the number of hard jets at the parton level. The kinematic mass of the generated Z/γ^* and the Higgs boson's hypothesized mass are also indicated.

- the p_T of the muons must be larger than 10 GeV,
- they must pass the loose muon ID requirement,
- they must be matched to a central track,
- their distance of closest approach must be <0.2 cm (0.02 cm) for tracks with zero (≥ 1) SMT hits,
- their detector pseudorapidity must be $|\eta| < 2.0$,
- the distance to the primary vertex must be $\Delta z(\text{primary vertex}, \mu)$<2 cm.

Also one should notice that the muon p_T in data is corrected using the primary vertex information for each event if the muon track has no associated SMT hits. The leading muon and the second leading muon transverse momentum distribution are shown in Figure 4.1.

From the muons that pass these cuts Z boson candidates are reconstructed. The standard DØ Z reconstruction from `wz_cafreco` is used [61]. The requirements for the two muons to be considered as a Z candidate are:

- the dimuon invariant mass must be between 70 and 130 GeV,
- the two muons must pass an anti-cosmic cut asking that the pseudo-acolinearity, defined as $(\pi - \Delta(\phi_1, \phi_2))^2 + (\pi - (\theta_1 + \theta_2))^2$, is bigger than 0.05,
- the muons must have opposite sign charge,
- the product of scaled isolation must be smaller than 0.03. [1]

The di-muon invariant mass distribution can be seen in Figure 4.2.

Events in the 2-jet sample are required to have at least 2 jets that pass the following constraints:

- the leading jet $p_T > 20$ GeV;
- all other jets $p_T > 15$ GeV;
- all jets $|\eta| < 2.5$;
- at least 2 tracks associated with the jet should be matched with the primary vertex.

[1] The scaled isolation for a single muon is defined as iso $= (p_T^{\text{cone}} + E_T^{\text{calorimeter}})/p_T^{\text{muon}}$

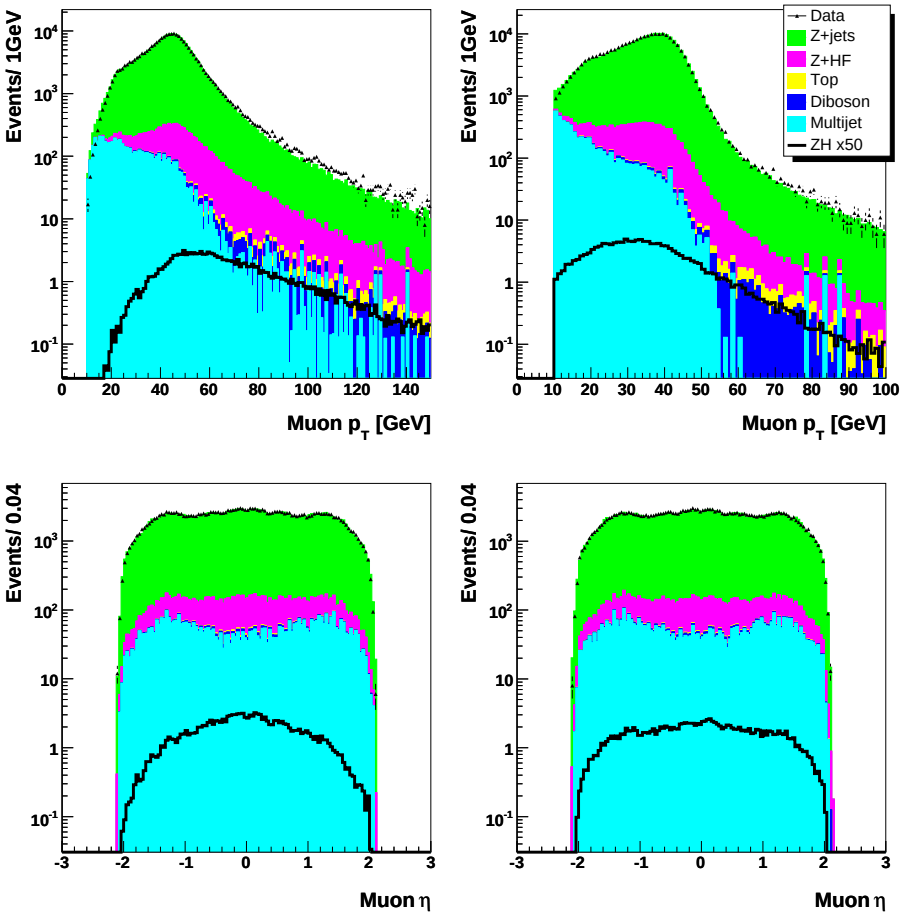

Figure 4.1: The leading muon (left) and second leading muon (right) p_T and rapidity distributions in the inclusive sample.

4.4 Corrections to MC

Because some of the variables in the Monte Carlo are known not to describe the data well, correction factors are applied. These are standard corrections applied in all similar analyses in DØ.

4.4.1 Z+jets cross section

The inclusive Z cross-sections determined by ALPGEN are Leading Log (LL) calculations and have been scaled to the Next to Next to Leading Order (NNLO) calculation [62]. Since the scale factor is not the ratio of a Leading Order to NNLO cross section, it is not a true k-factor, and we refer to it as a k' factor. The calculated ratio between NNLO inclusive Z cross-section to ALPGEN LL inclusive

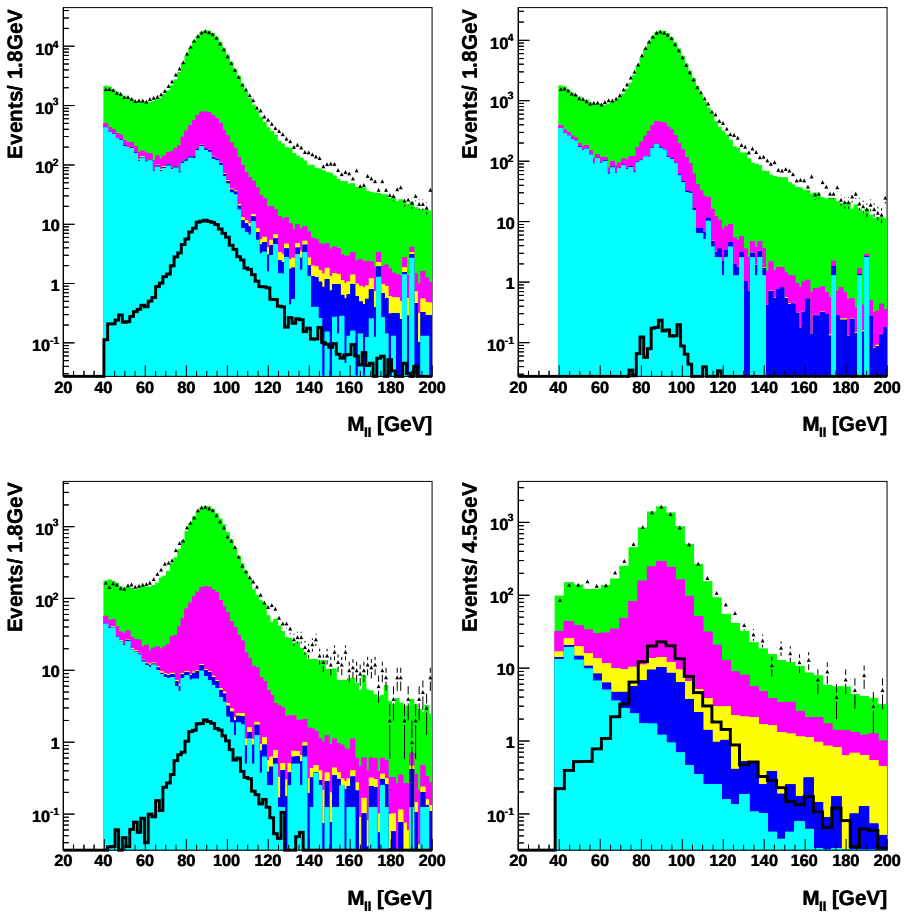

Figure 4.2: The di-muon invariant mass distribution for the inclusive, 0-jet, 1-jet and 2-jet sample after all MC corrections have been applied. The legend is the same as in Figure 4.1.

Z cross-section is

$$k' = 1.30. \tag{4.1}$$

This factor is then used to scale all the ALPGEN Z+light jets samples and an uncertainty of 10% is quoted due to variations of factorization scale, PDFs and generator cuts [63].

Using MCFM [64], a k-factor (NLO/LO) for Z+b$\bar{\text{b}}$ and Z+c$\bar{\text{c}}$ can be calculated. Taking the ratio of the MCFM k-factor for Z+heavy flavor jets versus the MCFM k-factor for Z+light jets gives an HF-factor. The ALPGEN Z+heavy flavor jets cross-sections are scaled by this additional factor for a total scaling of

$$k' * HF_{b\bar{b}} = 1.30 * 1.52 = 1.96, \tag{4.2}$$
$$k' * HF_{c\bar{c}} = 1.30 * 1.67 = 2.15. \tag{4.3}$$

4.4.2 Luminosity reweighting

The instantaneous luminosity profile of the minimum bias events overlayed in Monte Carlo is known not to be the same as the one of the data sample. The standard `LumiReweighting` processor is applied to all MC samples. The instantaneous luminosity profile for data and Monte Carlo can be seen in Figure 4.3.

4.4.3 Primary vertex reweighting

The distribution of the primary vertex position along the z direction is also not well modeled in Monte Carlo and the standard primary vertex reweighting has been applied. The z distribution of the primary vertex can be seen in Figure 4.3.

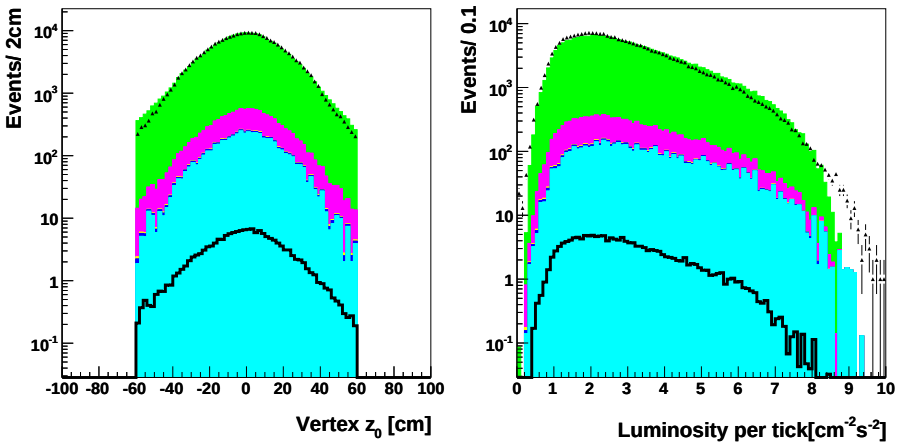

Figure 4.3: The z position distribution of the primary vertex and the instantaneous luminosity per tick profile (one tick is equal to 132 ns) after all MC corrections have been applied. The legend is the same as in Figure 4.1.

4.4.4 Z p_T reweighting

The Z p_T distribution is poorly modeled by both the PYTHIA and ALPGEN Monte Carlo generators, for events with $p_T(\mathrm{Z}) \lesssim 100$ GeV [65, 66]. The discrepancy between data and simulation is corrected using the jet multiplicity dependent reweighting functions derived from measurements in Z $\rightarrow$ ee data and seen in Figure 4.4. The Z p_T distributions can be seen in Figure 4.5 [66].

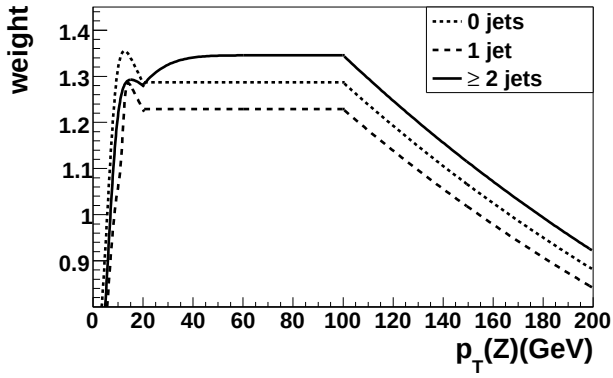

Figure 4.4: The jet multiplicity dependent Z p_T reweighting functions.

.

4.4.5 Jet corrections

To account for data and Monte Carlo efficiency differences, in Monte Carlo jets are smeared and removed using the standard JSSR processor [36]. Because there is no explicit ΔR cut between the jets and the muons of the Z candidate, one of the two muons can be inside one of the jets in the event. These muons are not considered for the JES corrections.

4.5 Multijet background

The multijet background is not well modeled in simulation and we derive this background from data. In this multijet sample no isolated Z candidate (or any di-muon resonance) can be present in the events.

The sample of multijet events is selected by reversing the muon isolation criteria, that is by requiring that the product scaled isolation of the two muons forming the Z candidate is >0.03. It is not sufficient just to have an enriched multijet sample, but one also needs to get the normalization factor corresponding to the number of multijet events passing the signal isolation cuts. We obtain this normalization factor by fitting template histograms in dilepton invariant mass 40 GeV $<$ $\mathrm{M_{ll}}$ $<$ 200 GeV for the multijet sample ($S_i^{multijet}$), all Z SM background processes (S_i^Z), and all non-Z SM processes (S_i^{Other}) and comparing them to the observed data distribution D_i. Minimizing

$$\chi^2 = \sum_{i=1}^{nbins} (\alpha S_i^{multijet} + \beta(S_i^Z + S_i^{Other}) - D_i)^2/D_i \tag{4.4}$$

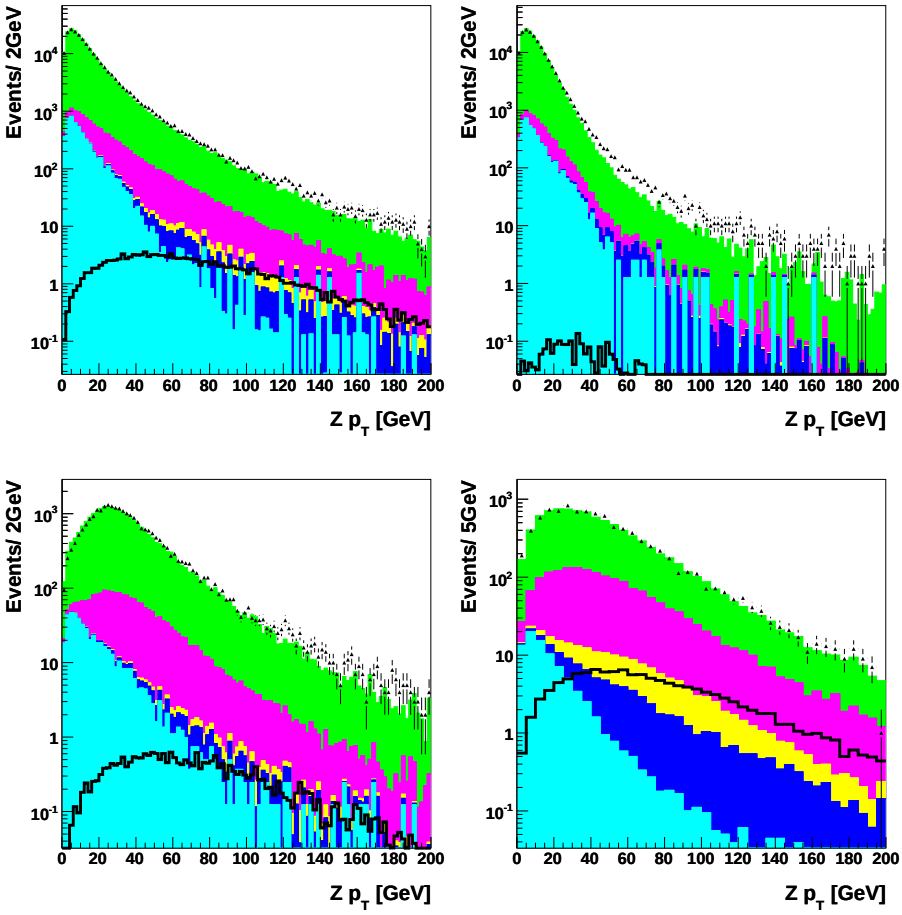

Figure 4.5: The Z transverse momenta distributions for the inclusive, 0-jet, 1-jet and 2-jet sample. The legend is the same as in Figure 4.1.

we find the normalization parameter α and β in the 0-jet exclusive, 1 jet exclusive and 2-jet inclusive samples. The parameters are summarized in Table 4.2.

If one applied directly the b-tagging to this selection of multijet background, the b-tagged samples would suffer from very limited statistics. To maximize the available multijet statistics, instead of directly applying b-tagging to data, light flavor TRFs were applied to the 2-jet pre-tag sample. In this way the shapes for the 1VT and 2L b-tagged samples were obtained. Even so the limited statistics in the data sample does not allow for a template fit in the b-tagged samples. Instead a sideband normalization procedure is constructed in the invariant dilepton mass region $40 - 70$ GeV. The β parameter is kept unchanged as the b-tagged samples could in principle be signal contaminated. For the two b-tagged samples (1VT and 2L), $N_{40-70}^{multijet}$ is defined as the sum of the weighted MC events (N_{40-70}^{MC}) subtracted

0 Jets		1 Jet		2 Jets	
α	β	α	β	α	β
1.31 ± 0.07	0.958 ± 0.003	0.16 ± 0.02	0.887 ± 0.006	0.010 ± 0.002	0.90 ± 0.01

Table 4.2: Multijet and background normalization parameters.

from the b-tagged data (N^{b-tag}_{40-70}) in the $40 < M(\mu\mu) < 70$ GeV mass window. The number of multijet events in the TRF weighted sample (N^{TRF}_{40-70}) is scaled by the factor α_{HF} so that it is equal to $N^{multijet}_{40-70}$:

$$N^{multijet}_{40-70} = N^{b-tag}_{40-70} - N^{MC}_{40-70}, \tag{4.5}$$

$$\alpha_{HF} * N^{TRF}_{40-70} = N^{multijet}_{40-70}. \tag{4.6}$$

This scaling factor is then applied to the light-jet TRF weighted multijet sample in the $70 < M(\mu\mu) < 130$ GeV mass window to estimate the multijet background in the b-tagged signal region. The α_{HF} values found for the 1 Very Tight tag is 14.6 ± 0.4 and for the 2 Loose tag is 15.0 ± 0.3. In this way a sample of multijet events is selected and the corresponding weight factors that need to be applied to this sample to account for jet multiplicity and b-tagging have been determined.

Any of the specific reweighting procedures described below have a small impact on the determination of the multijet background because of its small size.

4.6 Specific reweightings

4.6.1 Trigger modeling

Although no explicit trigger requirement is made, corrections for trigger acceptance effects still have to be made. It was noticed that when applying an explicit single muon OR trigger (i.e. that the event passes at least one of the single muon triggers) requirement on data and applying the corresponding trigger turn-on curves to Monte Carlo, there was good data to Monte Carlo agreement.

A correction is derived on data in the zero-jet bin as the ratio between the yields in the no trigger requirement case and in the case of the single muon OR requirement. The correction function is parameterized as a function of muon detector eta, Z rapidity, and $\Delta\eta$ between the Z candidate muons. The correction is binned in all of these variables with a bin width 0.1 and is not smoothed. This

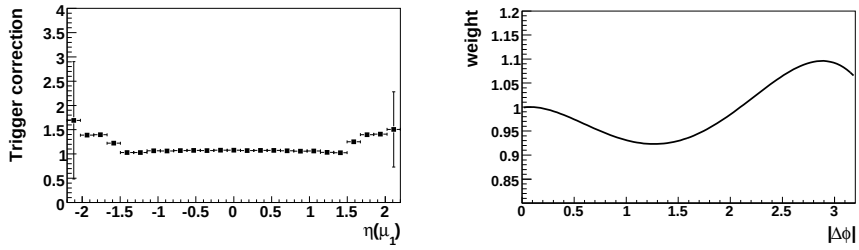

Figure 4.6: Projection on the leading muon p_T of the trigger correction function (left) and the $\Delta\phi$ reweighting applied to ALPGEN Monte Carlo(right).

correction function is applied to the Monte Carlo in addition to the single muon OR turn-ons. The projection of the trigger correction function can be seen in Figure 4.6. Distributions of the muon detector eta are found in Figure 4.1 and the Z rapidity and $\Delta\eta$ between the Z candidate muons are found in Figure 4.7.

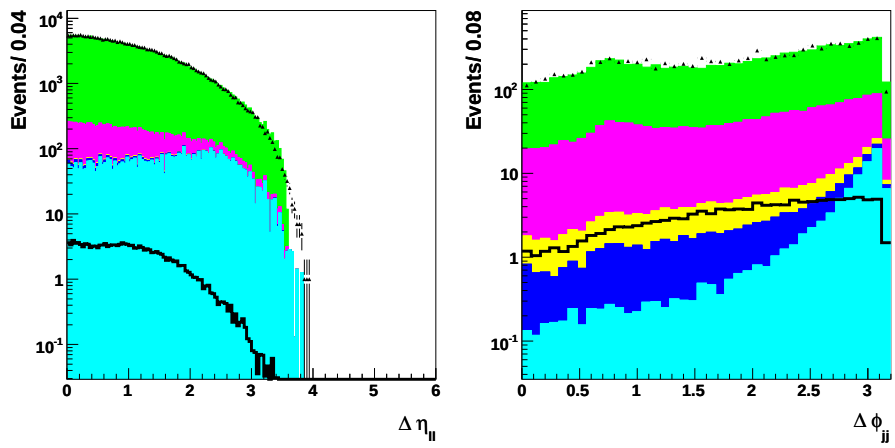

Figure 4.7: Di-lepton $\Delta\eta$ (left) and di-jet $\Delta\phi$(right) distributions. The legend is the same as in Figure 4.1.

4.6.2 Leading jets $\Delta\phi$ reweighting

After applying all previous corrections it was noticed that there is a disagreement in the leading 2 jets $\Delta\phi$ distribution between data and Monte Carlo. This type of disagreement was observed in the other vector boson plus jets channels. The difference is assumed to be due to the poor modeling of the jet $\Delta\phi$ distribution in ALPGEN Z Monte Carlo. The ratio between the data and Monte Carlo is fitted with a 4th order polynomial and then this reweighting is applied to the Z Monte

Carlo. The agreement of the data and Monte Carlo after applying this correction can be seen in Figure 4.7.

4.7 B-tagging

We are interested in identifying final states that have the same signature as a low-mass Higgs boson in our data. Hence we are interested in the properties of the candidate di-b-jet system in each event. We split our data sample into two orthogonal samples: a sample with at least 2 Loose NN b-tags and a second sample with exactly one VeryTight b-tag and no other Loose tag. This is done because one of the two b-jets can fail the b-tag, but in this manner we recover some of the lost acceptance due to double b-tagging. If only one of the jets is b-tagged in data we take as the second jet the highest-p_T untagged jet. If we encounter more than 2 tagged jets we form the dijet system out of the two highest-p_T tagged jets.

In data we tag directly the jets using the NN b-tagger. In MC we do not directly tag the jets but we allow for the possibility that any jet in the event can be tagged. In each MC event we can choose which jets we want to consider as tagged and apply the corresponding TRF-based weight. We consider all combinations of 2 jets in an event and weigh each combination with the probability of that combination falling into the desired b-tag bin: 2 Loose or 1 Very Tight.

Two-Loose inclusive combinations

We define L_i to be the probability that jet i is tagged loose inclusively. The probability of a pair of jets (i, j), where the jets have been ordered in p_T and $1 \leq i<j \leq n$, to be two-loose tagged inclusively is given in Table 4.3 and can be summarized by the formula :

$$p(i,j) = \frac{L_i L_j}{(1-L_i)(1-L_j)} \prod_{k=1}^{j} (1-L_k) \tag{4.7}$$

One-Tight exclusive combination

We define L_i as above and T_i as the probability that jet i is tagged tight. The probability of an event to have one and only one tightly tagged jet and all other jets in the event not to be loose tagged is given in Table 4.3 and can be summarized by the formula:

$$p(1,j) = \left(\prod_{k=1}^{n} (1-L_k)\right) \left(\frac{T_j}{1-L_j} + \delta_{j1} \cdot \frac{T_1}{1-L_1}\right) \tag{4.8}$$

	Combination	Two-Loose Probability	One-Tight Probability
2-jet	12	$L_1 L_2$	$T_1(1-L_2)+(1-L_1)T_2$
3-jet	12	$L_1 L_2$	$T_1(1-L_2)(1-L_3)+(1-L_1)T_2(1-L_3)$
	13	$L_1(1-L_2)L_3$	$(1-L_1)(1-L_2)T_3$
	23	$(1-L_1)L_2 L_3$	0
4-jet	12	$L_1 L_2$	$T_1(1-L_2)(1-L_3)(1-L_4)+(1-L_1)T_2(1-L_3)(1-L_4)$
	13	$L_1(1-L_2)L_3$	$(1-L_1)(1-L_2)T_3(1-L_4)$
	14	$L_1(1-L_2)(1-L_3)L_4$	$(1-L_1)(1-L_2)(1-L_3)T_4$
	23	$(1-L_1)L_2 L_3$	0
	24	$(1-L_1)L_2(1-L_3)L_4$	0
	34	$(1-L_1)(1-L_2)L_3 L_4$	0

Table 4.3: The probability that the considered combination of two jets falls withing one of the b-tagging bins.

	pre-selection	Z mass cut	1 tight b-tag	2 loose b-tags
Data	9304	8004	217	161
Background	9072±39	7922±37	229.5±1.3	148.8±1.0
ZH(115)	2.542±0.020	2.361±0.019	0.6114±0.0051	0.8560±0.0079
Multijet	83.86±0.68	12.71±0.27	1.831±0.044	1.866±0.035
Zjj	7285±38	6435±36	35.36±0.20	27.34±0.14
$Zb\bar{b}$	465.4±3.9	422.0±3.7	112.3±1.1	66.44±0.93
$Zc\bar{c}$	1032±8.1	915.0±7.5	63.92±0.63	32.59±0.39
ZZ	47.63±0.67	43.25±0.63	3.41±0.10	3.72±0.14
WZ	51.38±0.97	47.20±0.92	1.844±0.058	0.793±0.029
WW	12.25±0.82	4.95±0.52	0.149±0.024	0.072±0.014
$t\bar{t}$	94.39±0.52	41.87±0.35	10.735±0.092	15.97±0.15

Table 4.4: The numbers of events and statistical uncertainties in the dimuon sample in the inclusive sample, after the Z mass cut (60 GeV $< M_{\mu\mu} <$ 130 Gev) and in the 1T and 2L tag samples for data, various background processes and ZH signal, where the mass of the Higgs boson is $M_H = 115$ GeV.

We apply the weights above to each MC event and end up with the 2 orthogonal MC samples. The event yields for the inclusive sample and after applying b-tagging are found in Table 4.4. In the next chapter we will construct variables based on the event kinematics and use a multivariate technique to increase the Higgs signal to background discrimination.

Chapter 5

Analysis

In the previous chapter we have established a good agreement between MC and data. This chapter describes methods of improving the discrimination between the Higgs signal and backgrounds. In Section 5.1 a kinematic fit procedure is described that takes advantage of the kinematic constraints in the ZH channel. In Section 5.2, two variables are introduced that take advantage of spin correlations in the final states. Finally, in Section 5.3 we construct a discriminant that includes as inputs a set of variables characterizing the event and that is trained to increase the signal to background separation. All these steps are necessary in order to 'squeeze out' the most information from the available data.

5.1 Kinematic fit

In the DØ detector, the lepton energies are better modeled than those of hadron jets. As well, the ZH system's boost is moderate for the vast majority of events. As seen in Figure 5.1, we can assume that the missing transverse energy in the events is largely due to jet energy miss-measurements.

Because of these points a kinematic fit by χ^2 minimization is used, allowing the energies and angles of the leptons and jets to fluctuate. The form of the χ^2 that is minimized is:

$$\chi^2 = \sum_i \left(\frac{x_i - x_{i0}}{\sigma(x_i)} \right)^2 + \sum_j \lambda_j C_j \tag{5.1}$$

where x_i represent the energy, ϕ and η of the muons and jets (i=1,4), x_{i0} are the fitted values and σ_{x_i} the corresponding resolutions described below; λ_j the corresponding Lagrange multipliers for the sums of momenta on the transversal directions and the difference between the dilepton invariant mass and Z boson mass.

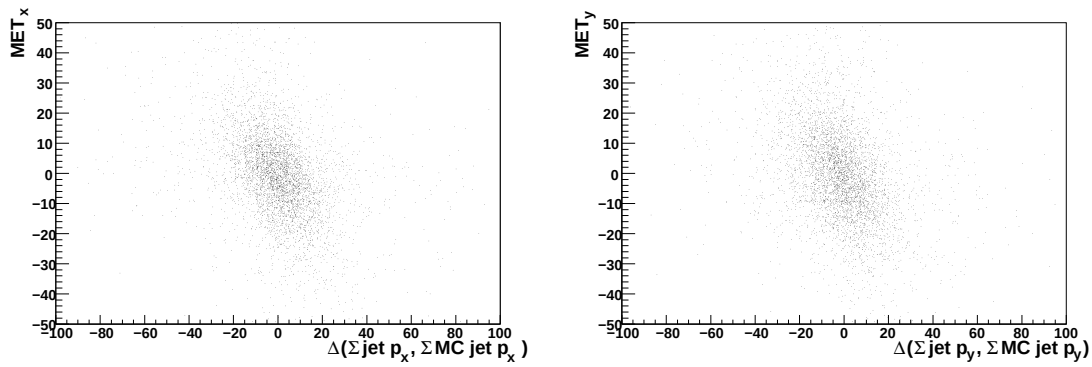

Figure 5.1: $\not{E}_T$ plotted against the difference between the reconstructed and MC truth momentum of the jets in ZH Monte Carlo events with $M_H = 115$ GeV. The x-axis projection is on the left, the y-axis projection on the right

	σ_η	σ_ϕ
Muon	0.002	0.001
Jet	0.08	0.08

Table 5.1: Muon and Jet angular resolutions.

The resolution of the angles as listed in Table 5.1 is considered to be constant as a function of η, ϕ and p_T and was measured in ZH Monte Carlo.

The muon momentum resolution function is a function of muon p_T and η_{det} [67], with the coefficients listed in Table 5.2:

$$\frac{\sigma_{p_T}}{p_T} = \begin{cases} \sigma_0 + \frac{\sigma_1}{p_T} & |\eta| \leq 1.28, \\ \sqrt{\left(\sigma_0 + \frac{\sigma_1}{p_T}\right)^2 + \left(\left(c_0 + \frac{c_1}{p_T}\right) * (|\eta| - 1.28)\right)^2} & |\eta| \geq 1.28. \end{cases} \tag{5.2}$$

The jet resolution is a function of p_T and given in bins of rapidity with the following parametrization

$$\frac{\sigma(p_T)}{p_T} = \sqrt{C^2 + S^2/p_T + N^2/p_T^2}, \tag{5.3}$$

	with SMT hit	without SMT hit
c_0	0.0024	0.0025
c_1	0.0102	0.0044
σ_0	0.0068	0.0092
σ_1	0.0484	0.0231

Table 5.2: Muon p_T resolution function coefficients, corresponding to the parameterizations in formula 5.2.

where $N = 2.0673$ GeV and the other parameters used depend on η and are given in Table 5.3.

It can be seen in Figure 5.2 that the kinematic fit pushes the signal towards higher di-jet invariant mass, while the background is pushed towards lower di-jet invariant mass.

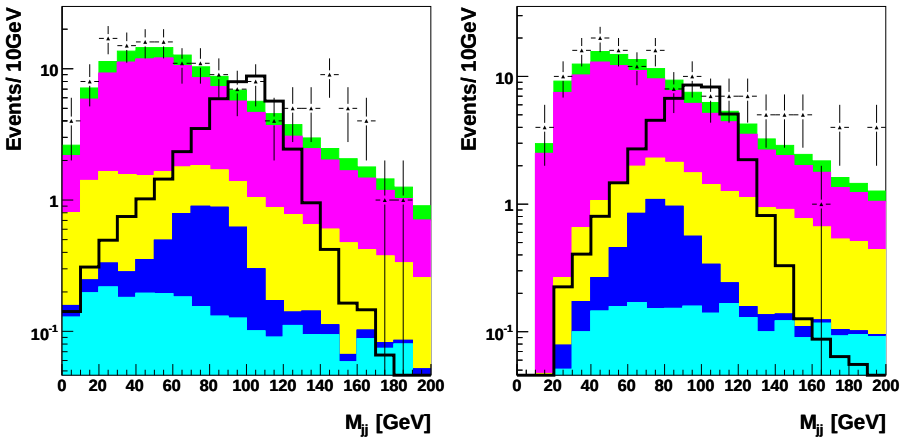

Figure 5.2: Di-jet invariant mass distribution before the kinematic fit (left) and after the kinematic fit (right) in the 2-Loose b-tags sample. The legend is the same as in Figure 4.1.

5.2 Spin related variables

Since the main background to the ZH signal is Zb$\bar{\text{b}}$ production, where the b$\bar{\text{b}}$ comes from the splitting of an off mass shell gluon, the two processes have different spin

	S $\mathrm{GeV}^{-1/2}$	C
$\lvert\eta\rvert < 0.4$	0.7029	0.0577
$0.4 < \lvert\eta\rvert < 0.8$	0.7829	0.0615
$0.8 < \lvert\eta\rvert < 1.2$	0.8884	0.0915
$1.2 < \lvert\eta\rvert < 1.6$	0.6263	0.1053
$1.6 < \lvert\eta\rvert < 2.0$	0.5850	0.0706
$2.0 < \lvert\eta\rvert < 2.4$	0.4691	0.0713
$2.4 < \lvert\eta\rvert < 2.8$	0.4873	0.0746
$2.8 < \lvert\eta\rvert < 3.2$	0.4005	0.0773
$3.2 < \lvert\eta\rvert < 3.6$	0.3740	0.0801

Table 5.3: Jet p_T resolution function coefficients for slices in η.

correlations. We applied the method suggested in [68] for differentiating between the WH and $Wb\bar{b}$ production at the Tevatron and successfully applied at DØ in the WH search [69]. In the rest frame of the Z (Figure 5.3) we define the angle χ_Z between the Z spin vector $\hat{s}_Z$ and one of the charged leptons. The separation between background and signal in this variable can be seen in Figure 5.13.

5.3 Boosted decision trees

5.3.1 Why use decision trees

Until recently, the standard for the use of multivariate discriminating techniques within High Energy Physics was the Artificial Neural Network (ANN). ANNs suffer when the number of input variables is large and adding noise deteriorates the performance. It was shown previously that Boosted Decision Trees (BDT) perform better than ANNs and that in the case of many input variables they are more robust [70, 71]. BDTs have performed very well in previous DØ searches [72] and we decided to use them to improve the performance of this search.

5.3.2 What are decision trees

A decision tree is a binary tree classifier. One example of such a classifier is shown in Figure 5.4. The tree is structured in nodes and leafs. The nodes contain a set of

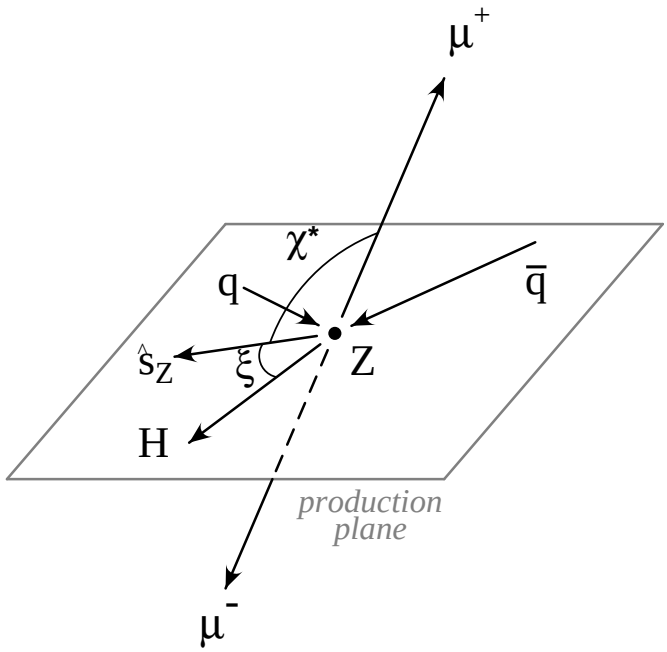

Figure 5.3: Definition of the $\chi^\star$ angle in the Z rest frame.

events and an associated cut in one of the variables characterizing the event. This cut splits the node into two lower nodes. A node that is not split further is called a leaf. The decision of not splitting the node is made based on assumptions that are going to be presented later. In this way the decision tree splits the events in the root node (the set of all events that are input to the DT) into leafs that are signal-like or background-like. The Boosted Decision Tree is an extension of the simple decision tree, where a series of trees are derived from the same training sample by reweighting events that were misclassified. This set of trees are combined into a single classifier, the output of each individual tree being weighted and all outputs summed together.

5.3.3 Training

The training is the process that defines the splitting criterion for each node. The splitting begins at the root node and then continues at subsequent nodes until the number of events in a node reaches a user defined number where the splitting of nodes stops. At every node the split is determined by finding the variable and the corresponding cut value that maximizes the signal and background separation. The criterion chosen for defining the separation between signal and background

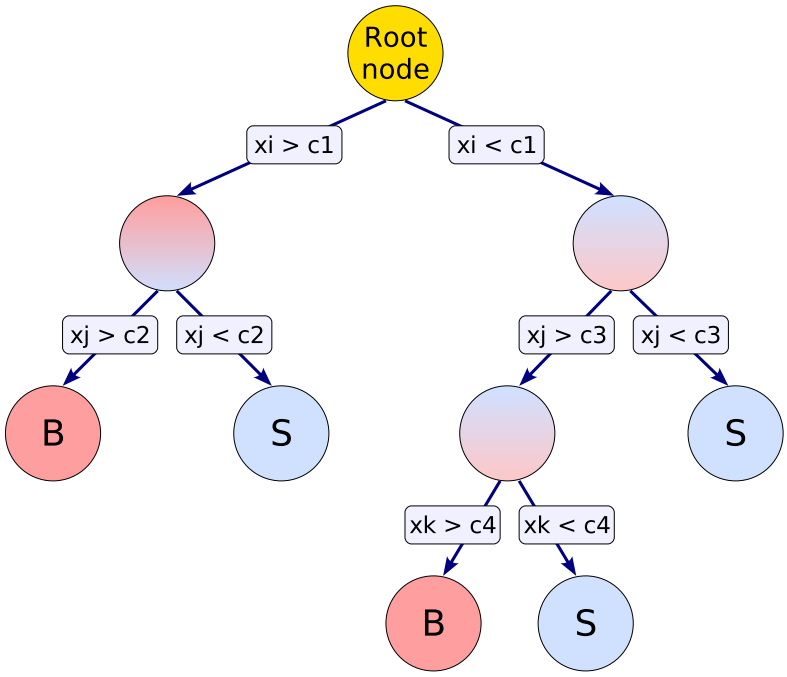

Figure 5.4: Schematic view of a decision tree.

was the Gini index defined by

$$\text{Gini index} = p(1-p), \tag{5.4}$$

where p is the purity. The Gini index is maximum at $p = 0.5$, when the samples are fully mixed, and falls to zero when the node consists of only one sample.

The training procedure selects the input variable and cut value that maximizes the decrease in the separation index between the parent node and the sum of the separation indices of the two daughter nodes properly weighted with respect to the fraction of events. This procedure is tried for each input variable in a set of equidistant points within the variable's range of values. For this analysis the number of points evaluated for each variable is set to 20.

5.3.4 Pruning

The splitting of nodes can in principle be continued until each leaf contains only signal or background events. This would be an over-trained tree. In order to make the decision tree stable with respect to statistical fluctuations of the training data set a pruning procedure is applied. Pruning is the process of cutting from bottom up the tree after it was built to its maximum size. In this way statistically

insignificant nodes are removed and the over-training of the tree is reduced.

For pruning we use the Cost Complexity algorithm that takes into account misclassification in a node when not split and compares it with the misclassification in the subtree starting from that node. A cost estimate is defined for each node as $R = 1 - \max(p, 1-p)$, while for a tree R it is computed using the purity p in the leafs of the tree. The cost complexity (ρ) for each node is defined as :

$$\rho = \frac{R(\text{node}) - R(\text{subtree below that node})}{\#nodes(\text{subtree below that node}) - 1}. \tag{5.5}$$

The node with the smallest ρ value is recursively pruned away as long as ρ is smaller than a predefined value ρ_0 (also known as prune strength). For this analysis $\rho_0 = 0.05$.

5.3.5 Boosting

A single tree has limited discrimination power and it is highly susceptible to over-training. One way to overcome this problem is to reweight all misclassified events in the training sample and to retrain a new tree. The name of this procedure is called boosting and it is not specific to decision trees but can be applied to all classifiers. For boosting we used the algorithm called AdaBoost [73]. Events that were misclassified during the training of a tree are given a higher event weight in the training of the following tree. The weight given to all misclassified events is

$$\alpha = \frac{1 - err}{err}, \tag{5.6}$$

where err is the misclassification rate of the tree considered.

In this way starting from a single tree a series of trees (or a forest) is subsequently constructed. If we consider an event to be characterized by the vector of variables x and the output of a single tree to be $h_i(x)$, the output of the forest is

$$y_{BDT}(x) = \sum_{i \in \text{forest}} \ln(\alpha_i) \cdot h_i(x), \tag{5.7}$$

where i is the tree number in the forest or the boost order and α_i is the weight in Equation 5.6 of the boost i. For our analysis we have chosen the output of the individual tree $h_i(x)$ to be the training signal purity of the leaf in which event x is classified.

It is worth noting here that the pruning is performed after the boosting parameter is computed, and hence the error fraction is computed on the unpruned tree.

For this analysis forests containing 100 trees were used.

5.3.6 Implementation of BDTs for the search

We used the package TMVA [74] for implementation of the BDTs. Great care was taken to minimize the over-training of the BDT. The training was done only on Monte Carlo events. We considered all backgrounds, except the multijet one, and trained separately against every mass Higgs signal mass sample (see Table 4.1). At each Higgs mass point a BDT was trained for the single b-tag sample and one BDT for the double b-tag sample. The Monte Carlo events were split in 3 samples. Two quarters of the events are used, one for training and one for testing the BDTs. The remaining half is used in building the histograms used for the search of the signal.

The BDT parameters and the variables used for training were chosen after optimization studies were carried out. These studies concentrated on finding the best parameters for the construction of the discriminant and using a number of input variables that would give the best discriminant within a reasonable computing time.

From the technical point of view the BDT that was chosen was one that resulted from 100 boosting cycles using the AdaBoost algorithm. The minimal number of events in a node is 20 and pruning was done using a Cost Complexity cut-off with a value of 0.05. The output of the tree is in terms of the ratio of Signal to Background events in the final leaf. The choice of these parameters was a combination of the TMVA recommendations, previous experience with the BDT in this search and tests that optimized the BDT for speed in training and evaluation, stability, and sensitivity. There is an interplay between these parameters and hence an absolute best BDT is hard to identify. But we noticed that, for example, the improvement between 100 boosting cycles and 500 boosting cycles is negligible in sensitivity, while the training and testing time is increased about four-fold.

Regarding the input variables, we started with a list of approximately 40 variables. The original list of variables included highly correlated ones, for example the same variable before and after the kinematic fit was performed. This number was considered excessive, both for training speed reasons and also having in mind that only one of the highly correlated variables was desired to remain in the final list. An iterative procedure was used for eliminating variables that were ranked as low performing in the BDT. At first a BDT with 5 boost cycles was used and the worst 5 performing variables were eliminated. The procedure used to evaluate the performance of the variables is the one implemented in TMVA. The ranking of variables is determined by counting how often the variables are used to split tree nodes, and by weighting each splitting by the separation gain-squared achieved and by the number of events in the node. The procedure described above was repeated increasing the number of boost iterations. After 10 variables were eliminated a crosscheck was made by training a 100 boost cycles BDT with all the

variables and only the variables that were not eliminated in the previous steps. Only variables that were in both cases in the 10 least performing variables were eliminated for good. On the remaining set of variables the procedure was repeated until a number of variables that was considered manageable (25) was achieved. This optimization was done on the 2 Loose sample and a signal sample with a Higgs mass of 115 GeV. The assumption that it holds for all other relevant Higgs mass points and the 1 Very Tight sample was made. A comparison between a set of BDTs with different boosting cycles and variables can be seen in Figure 5.5.

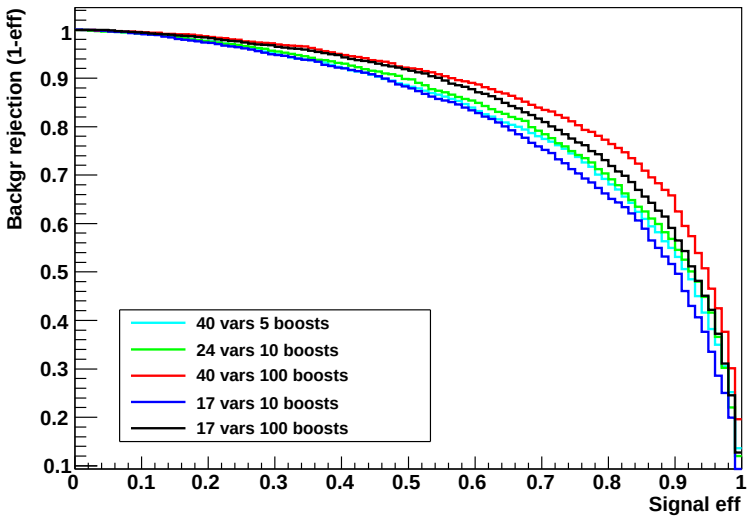

Figure 5.5: Background rejection rate plotted versus the signal acceptance efficiency for several Boosted decision tree configurations. The configurations correspond to successive steps in the optimization of the list of inputs used in the BDT.

So far this optimization was done only on Monte Carlo. A last step of optimization looked at the data to MC agreement and the correlation among the input variables. The data to MC agreement was assessed in the 2 jet sample before tagging, and the variables that showed relatively large disagreement were eliminated. Due to limited statistics it was assumed that the agreement between data and MC is hard to asses in the b-tagged samples; hence the choice for the pre-tagging sample. After this step only one of the highest performing variable in a set of highly correlated ones was kept. In this way the final list of 17 input variables was obtained, all of them showing good data to MC agreement. Plots of these 17 variables in the 2 jet sample before tagging, 1 Very Tight sample and 2 Loose b-tag sample can be seen in Figures 5.6-5.14.

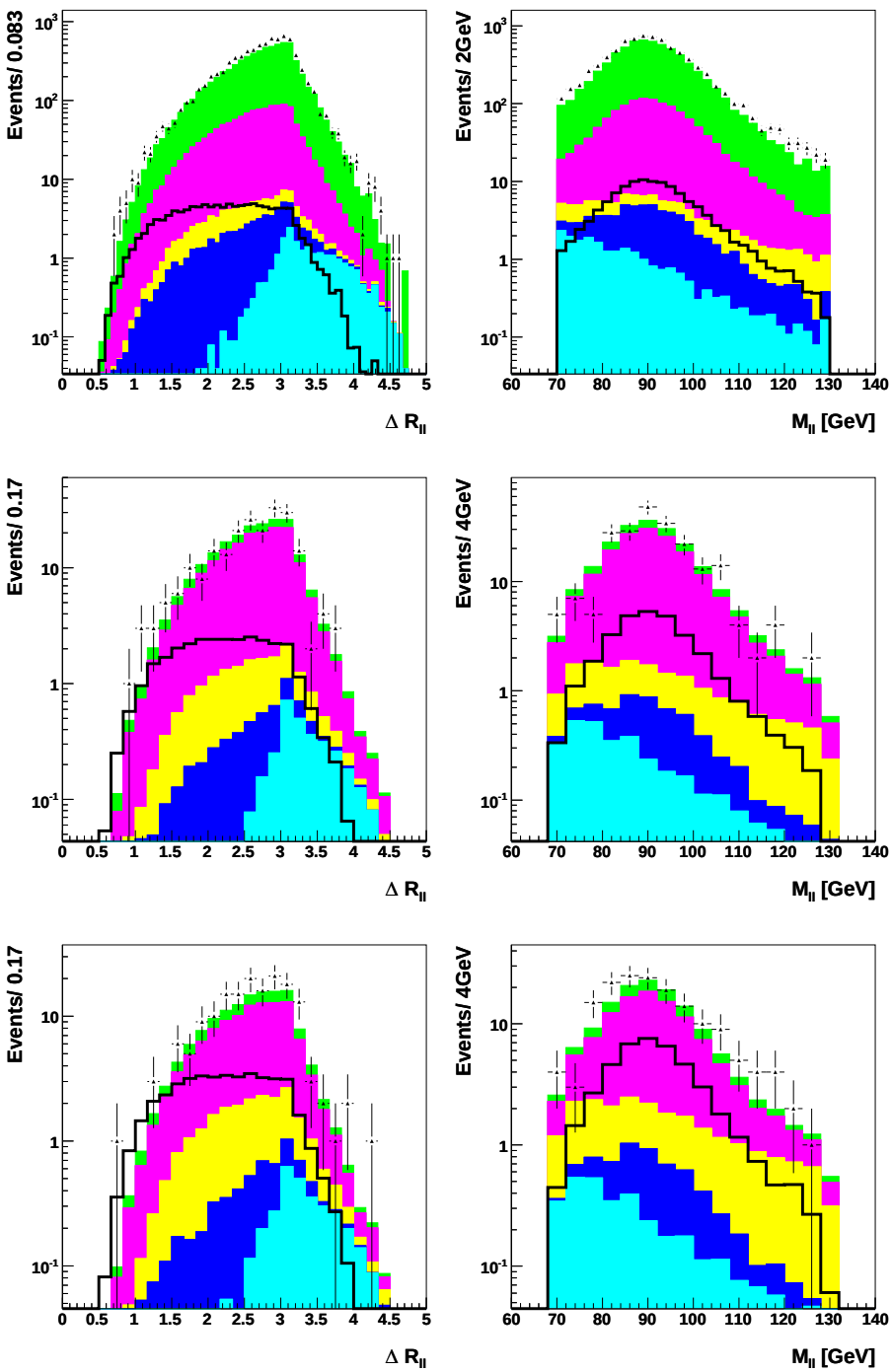

Figure 5.6: The di-muon ΔR (left) and invariant mass (right) in the 2-jets before tagging (top), 1 Very Tight b-tag (middle) and 2 Loose b-tags (bottom) sample. The legend is the same as in Figure 4.1.

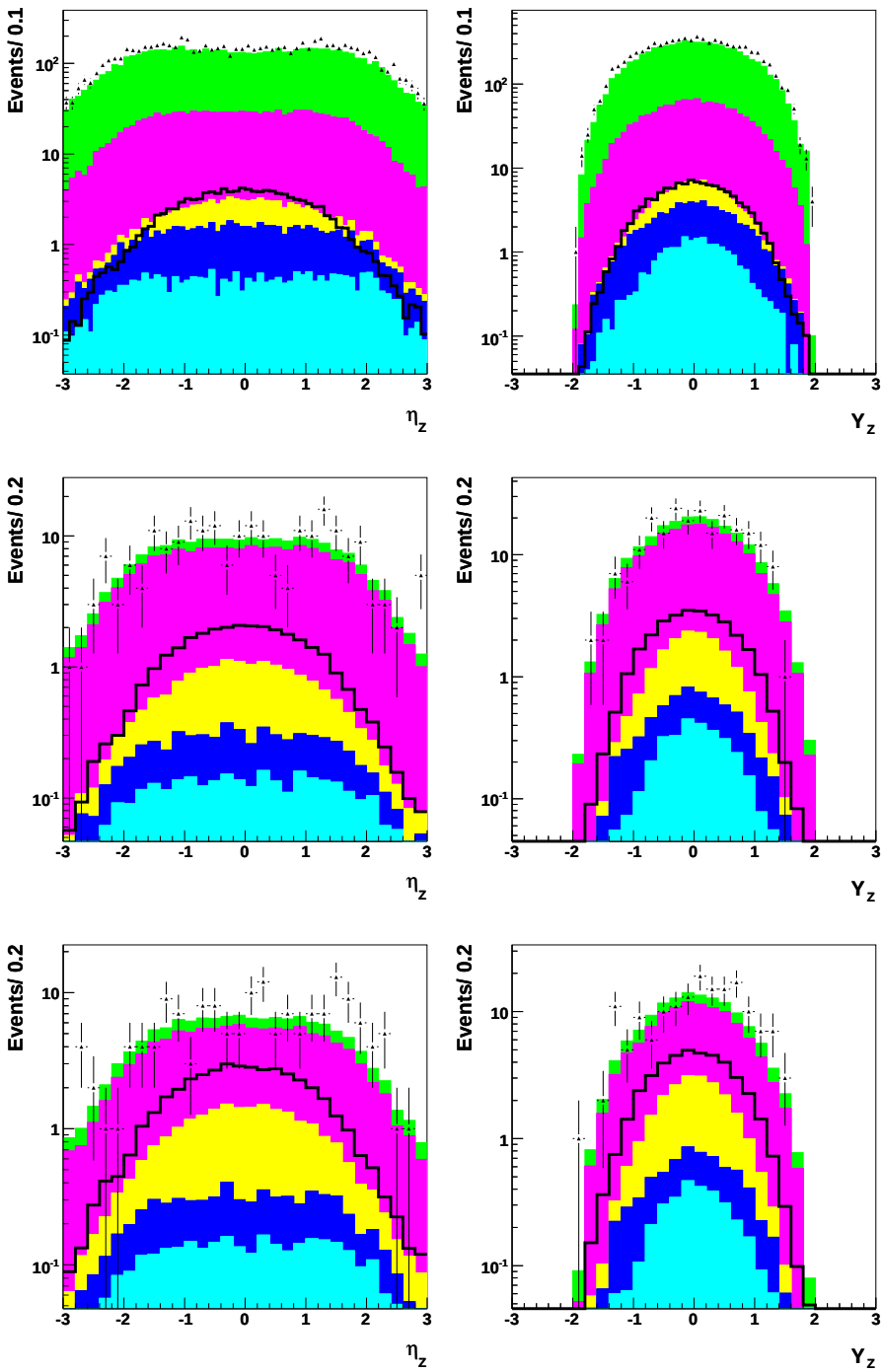

Figure 5.7: The di-muon pseudo-rapidity (left) and rapidity (right) in the 2-jets before tagging (top), 1 Very Tight b-tag (middle) and 2 Loose b-tags (bottom) sample. The legend is the same as in Figure 4.1.

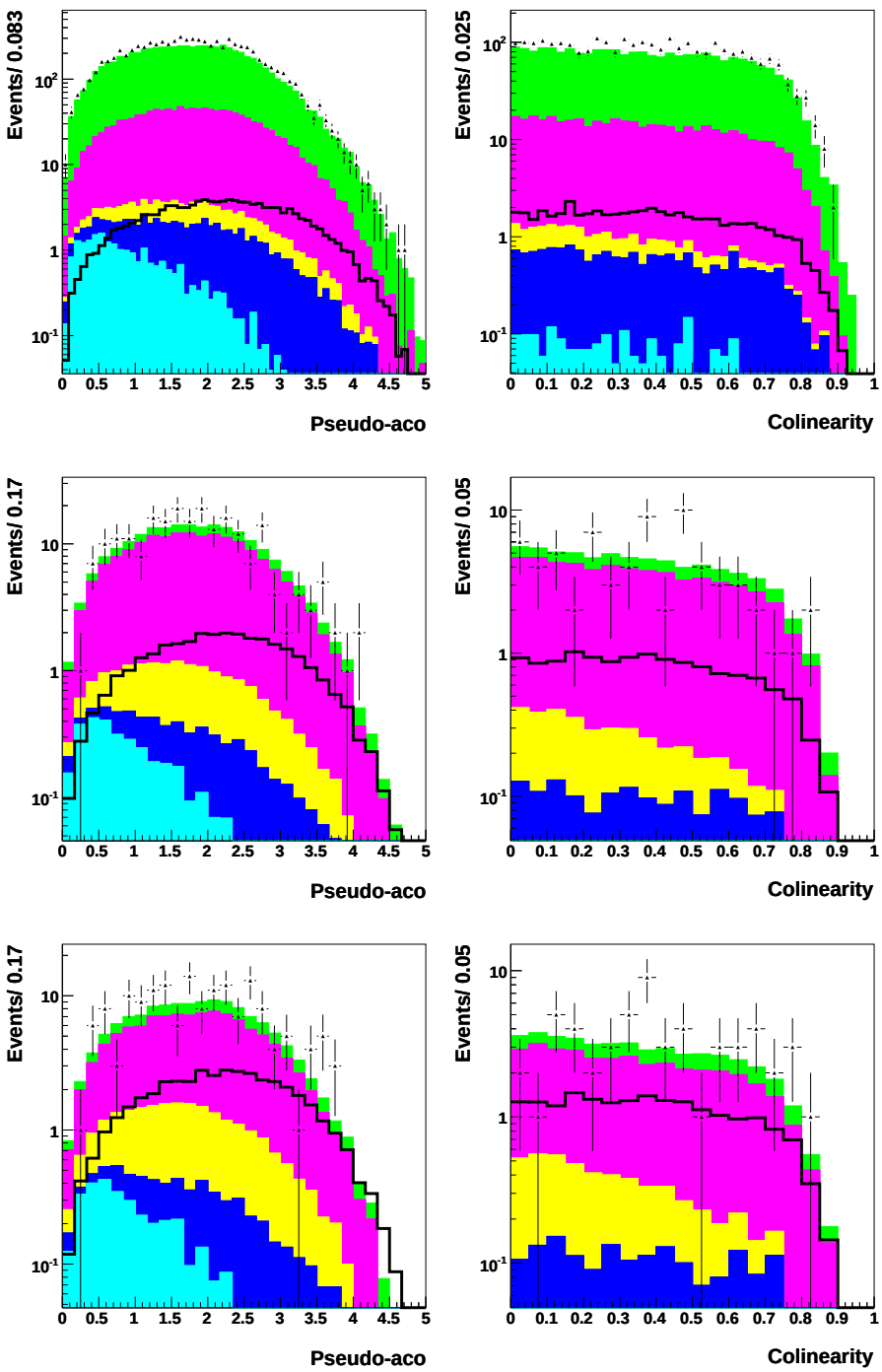

Figure 5.8: The di-muon pseudo-acoplanarity (left) and collinearity, defined as $\overrightarrow{p_1} \cdot \overrightarrow{p_2}/\sqrt{p_1^2 \cdot p_2^2}$, (right) in the 2-jets before tagging (top), 1 Very Tight b-tag (middle) and 2 Loose b-tags (bottom) sample. The legend is the same as in Figure 4.1.

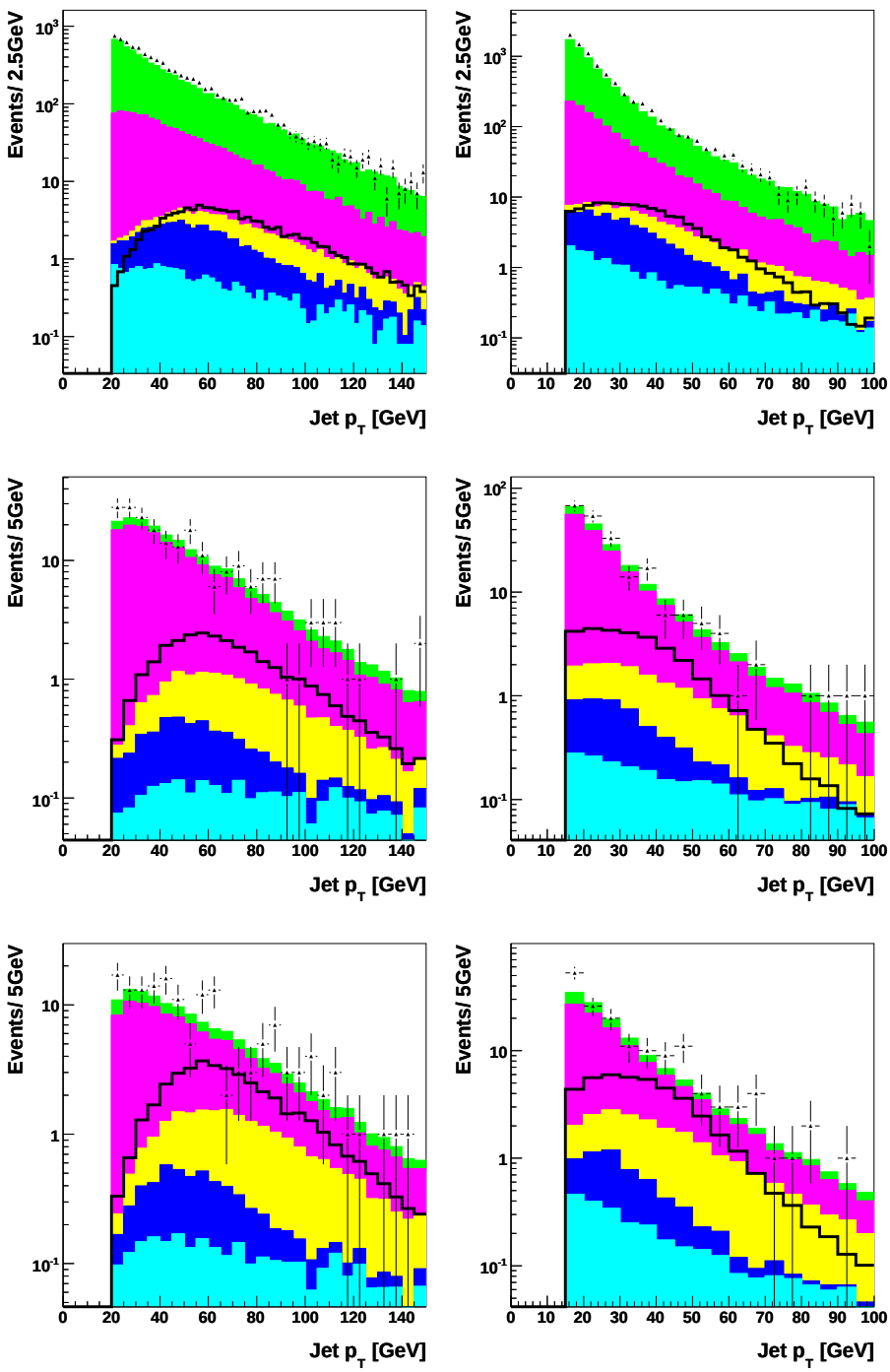

Figure 5.9: The leading jet p_T (left) and second leading jet p_T (right) in the 2-jets before tagging (top), 1 Very Tight b-tag (middle) and 2 Loose b-tags (bottom) sample. The legend is the same as in Figure 4.1.

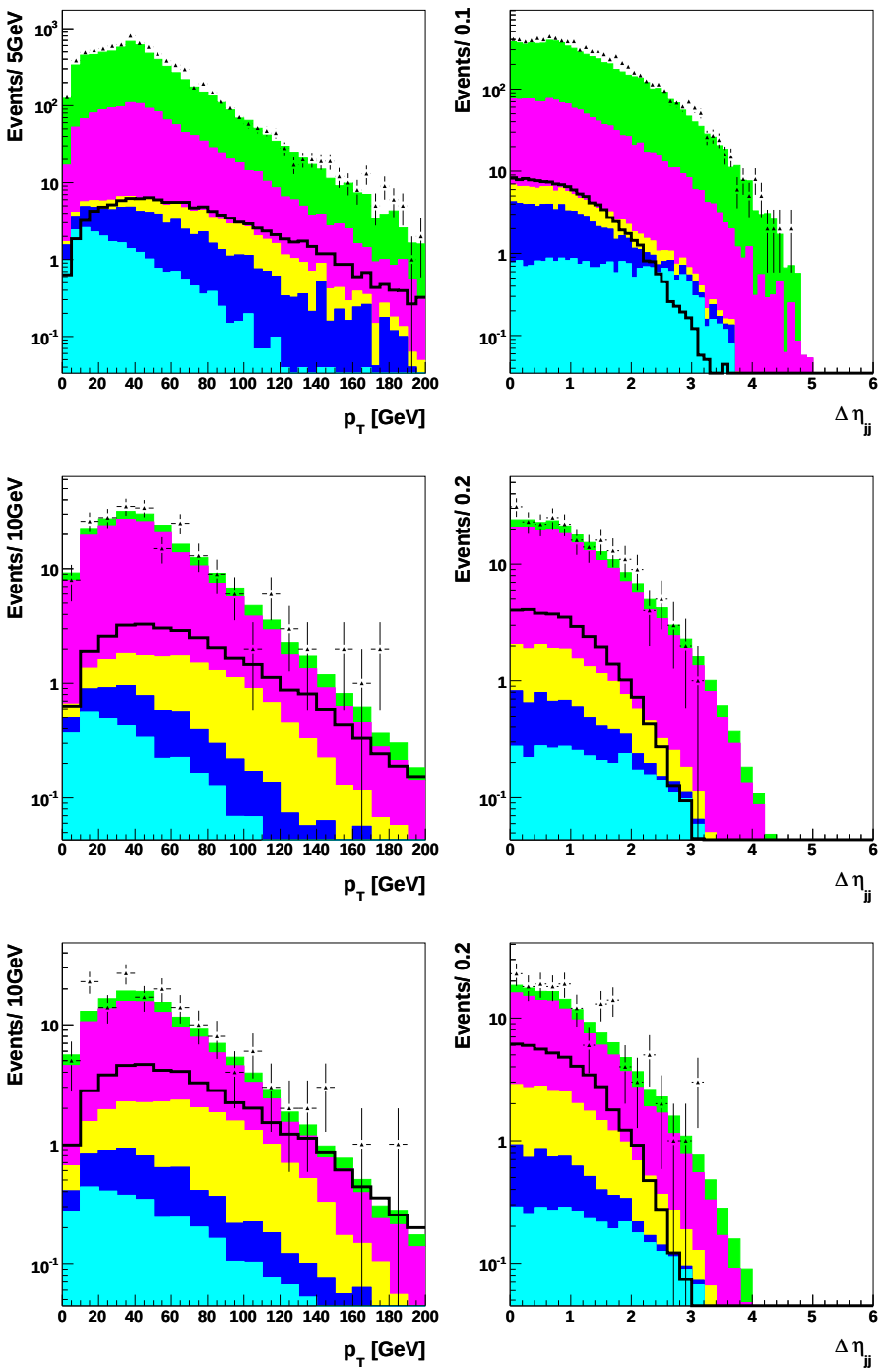

Figure 5.10: The di-jet system p_T (left) and di-jet $\Delta\eta$ (right) in the 2-jets before tagging (top), 1 Very Tight b-tag (middle) and 2 Loose b-tags (bottom) sample. The legend is the same as in Figure 4.1.

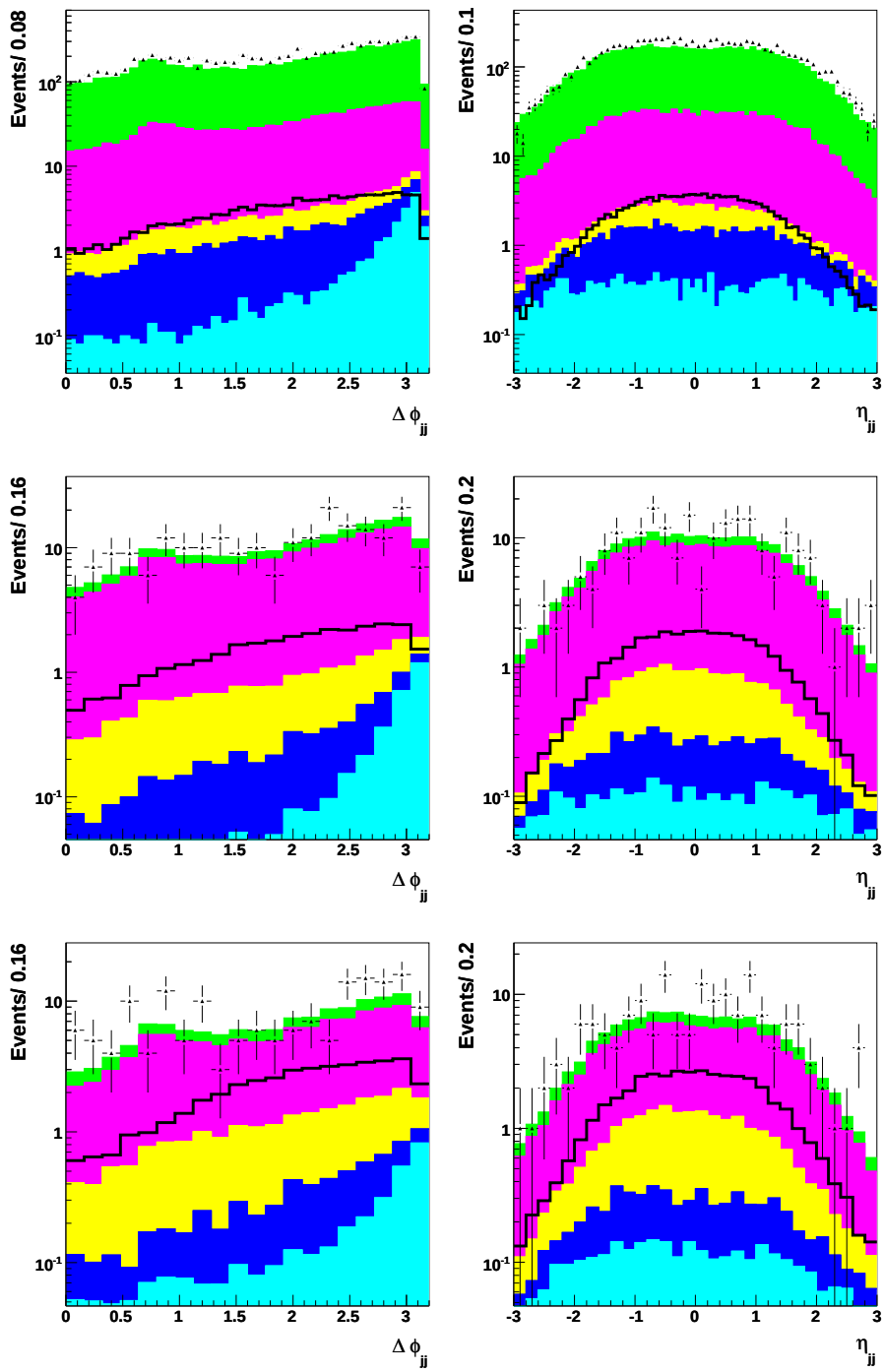

Figure 5.11: The di-jet $\Delta\phi$ (left) and di-jet system η after the kinematic fit (right) in the 2-jets before tagging (top), 1 Very Tight b-tag (middle) and 2 Loose b-tags (bottom) sample. The legend is the same as in Figure 4.1.

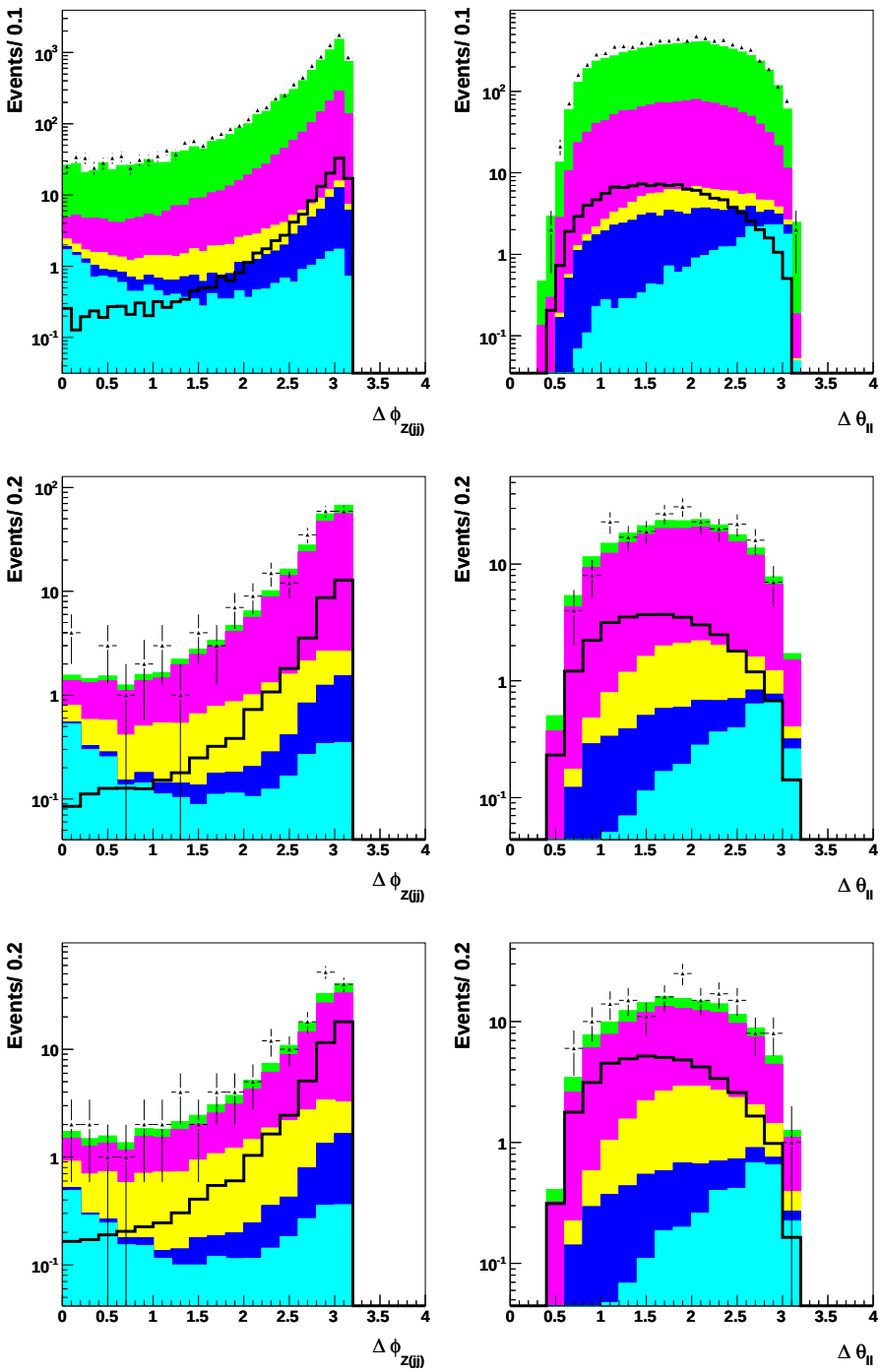

Figure 5.12: The $\Delta\phi$ between the Z candidate and the di-jet system (left) and the dilepton $\Delta\theta$ (right) in the 2-jets before tagging (top), 1 Very Tight b-tag (middle) and 2 Loose b-tags (bottom) sample. The legend is the same as in Figure 4.1.

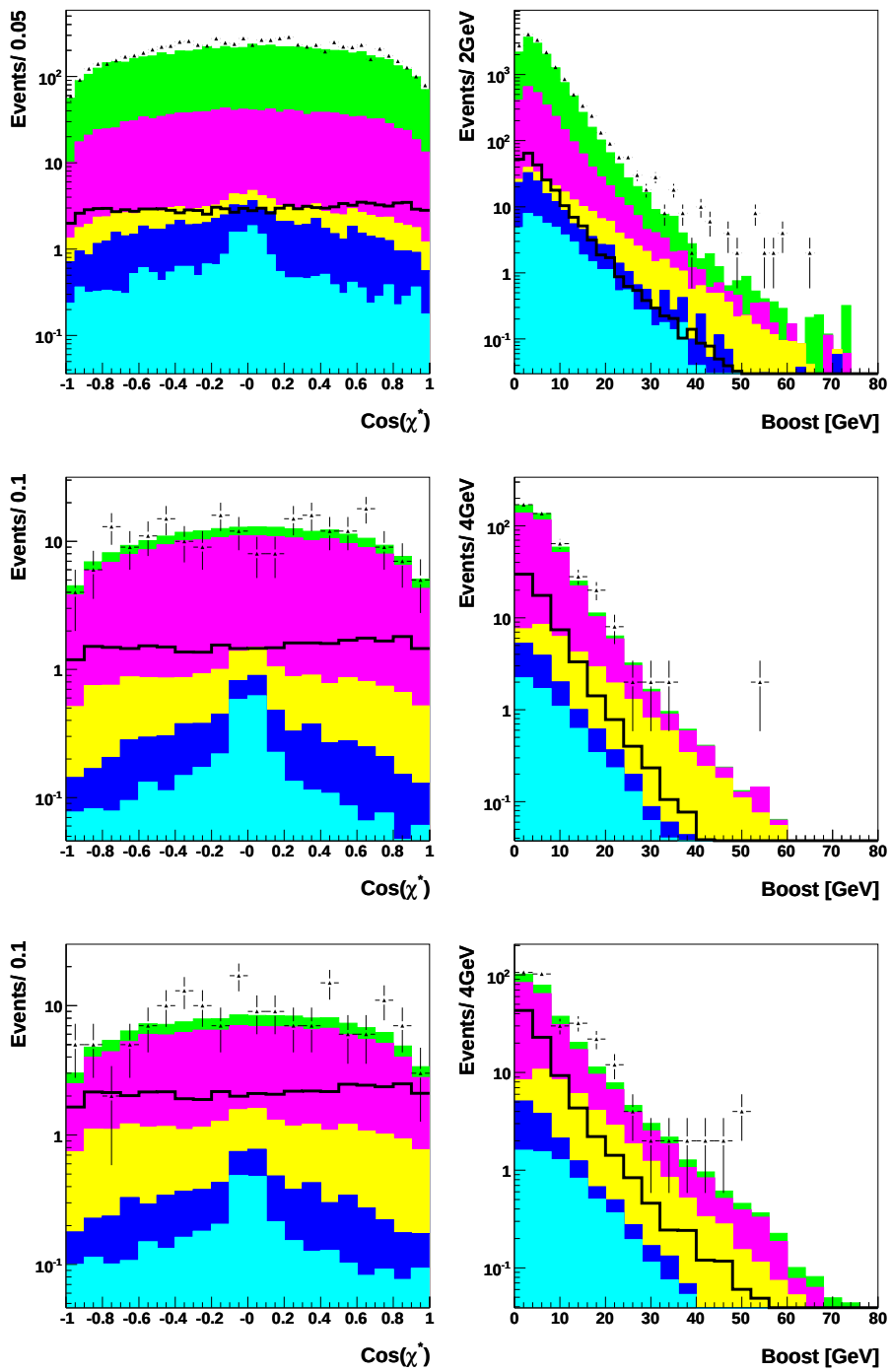

Figure 5.13: The $\cos\chi^{\star}$ (left) and perpendicular boost after the kinematic fit of the ZH candidate system(right) in the 2-jets before tagging (top), 1 Very Tight b-tag (middle) and 2 Loose b-tags (bottom) sample. The legend is the same as in Figure 4.1.

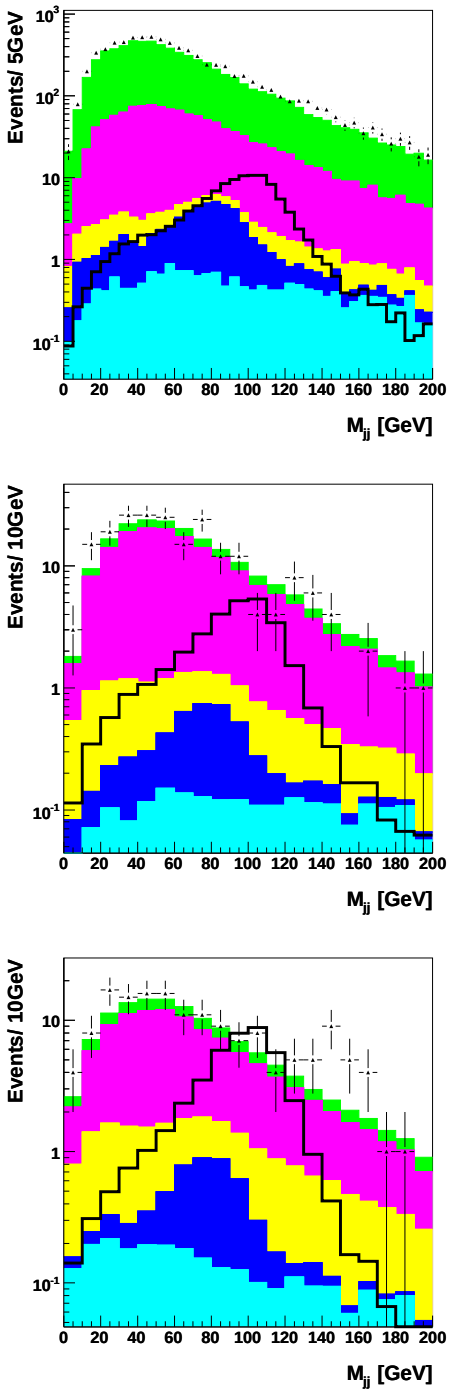

Figure 5.14: The massless dijet invariant mass after the kinematic fit in the 2-jets before tagging (top), 1 Very Tight b-tag (middle) and 2 Loose b-tags (bottom) sample. The legend is the same as in Figure 4.1.

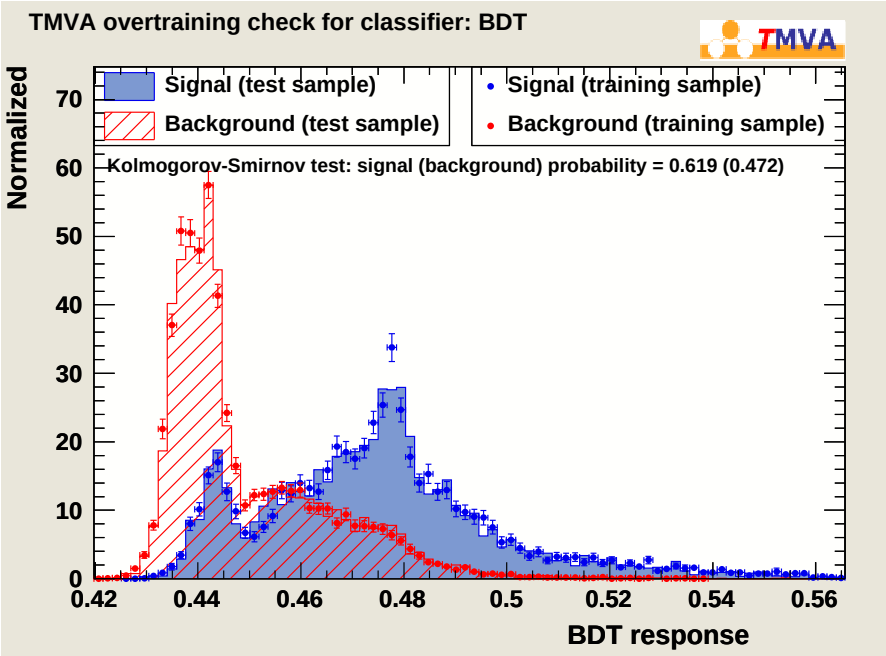

Figure 5.15: The Boosted decision tree output for the testing and training samples for a Higgs signal of 115 GeV and background Monte Carlo samples in the 2 Loose b-tags sample. The signal and background samples have been normalized to the same integral.

The output for the BDT discriminant for a 115 GeV Higgs and in the 2 Loose b-tag sample can be seen in Figure 5.15. It can be seen that the BDT does not exhibit over-training, i.e. the test sample reproduces the distribution of the training sample both for the signal and background. Due to the fact that some bins in the BDT output have limited statistics a transformation is applied to the BDT output. This transformation maps the output to the interval [0-1] and rebins the distribution from right to left such that the relative statistical uncertainty on the signal and the sum of backgrounds is less that 10% in every bin. The BDT discriminant for 3 Higgs masses can be seen in Figure 5.16. No significant excess over the expected background is observed in any of the mass bins.

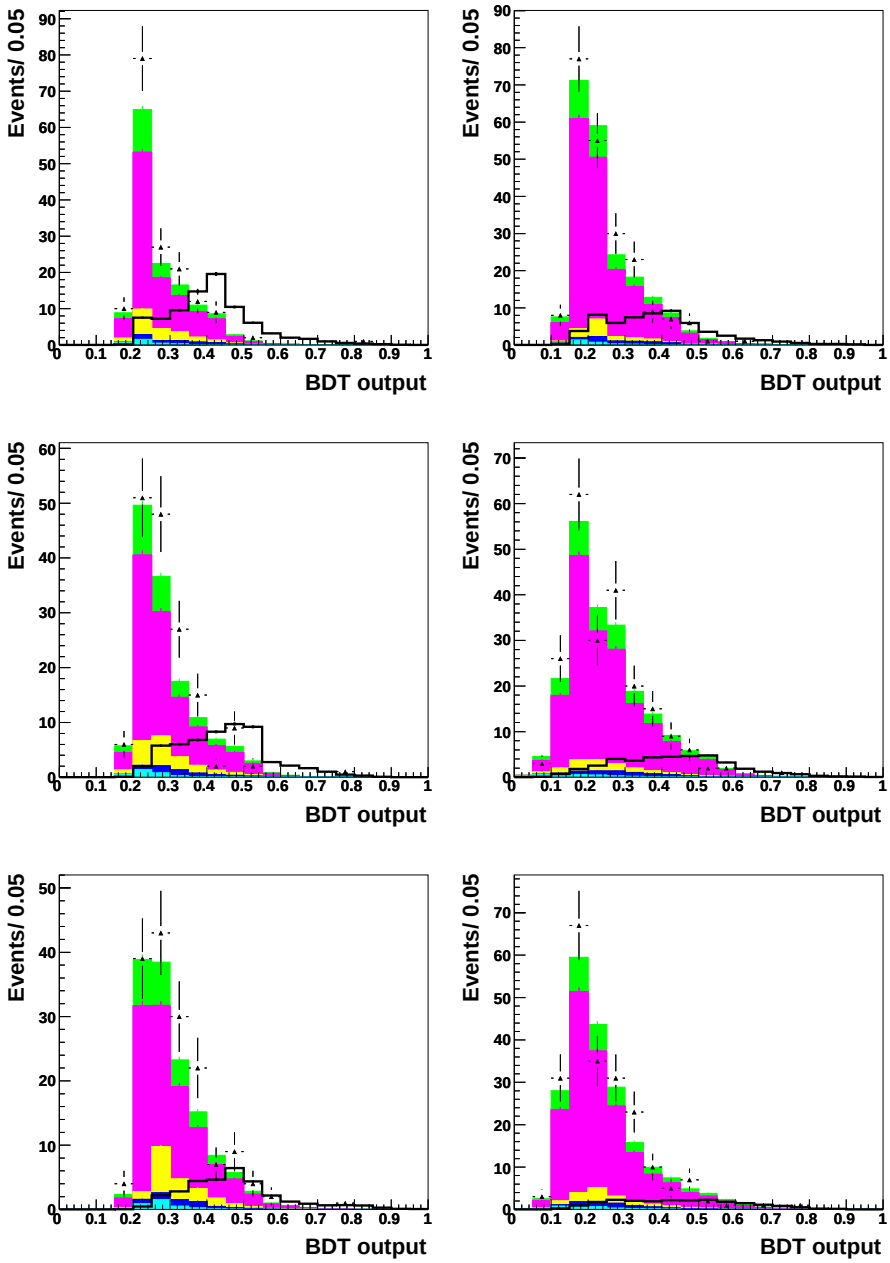

Figure 5.16: Boosted decision tree outputs for the 2 Loose b-tag sample (left) and 1 Very Tight b-tag sample (right) for the 115 GeV (top), 125 GeV (middle) and 135 GeV mass Higgs hypothesis. The legend is the same as in Figure 4.1 but in these plots the ZH cross-section is multiplied by a factor of 100.

Chapter 6

Limits on Higgs production

As seen in the previous chapter no excess of data over the expected background was observed. Under these conditions limits for the SM Higgs production can be set. The way these limits are computed is described in the first part of this chapter. The second part covers the systematic uncertainty sources that were considered in this analysis and the last part presents the limits obtained.

6.1 Limit setting procedure

In this section the DØ limit setting procedure is outlined. The procedure is a modified semi-Frequentist confidence level method, also known as the LEP method[75]. A full description of the procedure can be found in [76, 77, 78].

We use a likelihood ratio as the statistic method and it is defined for a single bin i as

$$Q = \frac{P(data|s+b)}{P(data|b)}, \tag{6.1}$$

where $P(data|s+b)$ is the likelihood that the data is consistent with the $s+b$ hypothesis (also called the test hypothesis) and $P(data|b)$ is the likelihood that the data is consistent with the background-only hypothesis (the null hypothesis). For a single bin experiment this likelihood depends on the prediction of the number of events for that bin, the number of observed events and systematic uncertainties. The likelihood can be expressed in terms that are of direct interest and in terms of so-called nuisance parameters. Nuisance parameters are parameters that are not of immediate interest to the test, but they are needed to estimate the parameters of interest. It is common for an experiment to determine the best fit model relative to the nuisance parameters values. In such cases the hypothesis can be evaluated such that the likelihood is maximized over the space of nuisance parameters.

Given a set of predicted and observed numbers of events and nuisance parameter values, a model that represents the best fit to the data observation within the constraints of the nuisance parameters can be defined. This fit is performed by minimizing the following:

$$\chi^2 = -2\ln\left(\frac{\mathcal{L}^P}{\mathcal{L}_0^P} \times \frac{\mathcal{L}^G}{\mathcal{L}_0^G}\right), \tag{6.2}$$

with the following definitions:

$$\mathcal{L}^P = \prod_i^{Nbins} \frac{p_i^{d_i} e^{-p_i}}{d_i!}, \tag{6.3}$$

$$\mathcal{L}_0^P = \prod_i^{Nbins} \frac{d_i^{d_i} e^{-d_i}}{d_i!}, \tag{6.4}$$

$$\mathcal{L}^G = \prod_i^{NPar} \left(\frac{1}{\sigma_k\sqrt{2\pi}}\right) e^{-\frac{(\theta_k-\theta_k^0)^2}{2\sigma_k^2}}, \tag{6.5}$$

$$\mathcal{L}_0^G = \prod_i^{NPar} \left(\frac{1}{\sigma_k\sqrt{2\pi}}\right), \tag{6.6}$$

where $\mathcal{L}^P$ is the Poisson likelihood over all bins ($Nbins$) of the predicted (p_i) and observed (d_i) number of events. $\mathcal{L}_0^P$ corresponds to the situation when $p_i = d_i$. $\mathcal{L}^G$ is the likelihood function that reflects the constraints on the nuisance parameters and is assumed to be Gaussian. $NPar$ is the number of nuisance parameters (systematic uncertainties), θ_k^0 is the predicted value of the nuisance parameter, σ_k is the uncertainty on the nuisance parameter and θ_k is an alternative value of the nuisance parameter k.

The nuisance parameters can be written as

$$\theta_k = \theta_k^0(1 + R_k \times \beta_k), \tag{6.7}$$

where $\beta_k = \sigma_k/\theta_k^0$ and $R_k = (\theta_k - \theta_k^0)/\sigma_k$.

The χ^2 function can be written in terms of R_k :

$$\chi^2(\vec{R}) = 2\sum_i^{Nbins}\left(p_i(\vec{R}) - d_i\right) - d_i \ln\left(\frac{p_i(\vec{R})}{d_i}\right) + \sum_k^{NPar} R_k^2, \tag{6.8}$$

with

$$p_i(\vec{R}) = \sum_{j=1}^{Ns} p_{ij}(\vec{\theta}^0)\left(1 + \sum_{k=1}^{NPar} R_k\sigma_{ijk}\right), \tag{6.9}$$

where p_{ij} is the contribution of event source j to bin i, Ns is the total number of event sources, and

$$\sigma_{ijk} = \sigma_k \frac{\partial p_{ij}(\vec{\theta})/\partial\theta_k}{p_{ij}(\vec{\theta^0})} \tag{6.10}$$

defining the fractional change in the number of events for the specified nuisance parameter k and for the specified event source j.

We can now express the negative log-likelihood ratio of the maximized likelihoods in terms of the hypotheses for $s+b$ and b

$$\eta_d = -2\ln(Q(data,\theta)) = -2\ln\left(\frac{\mathcal{L}(data|s+b,\theta_{s+b})}{\mathcal{L}(data|b,\theta_b)}\right) \tag{6.11}$$

$$= \chi^2(s+b,\theta_{s+b}) - \chi^2(b,\theta_b), \tag{6.12}$$

where θ_{s+b} represents the set of nuisance parameters that maximizes the likelihood for the $s+b$ hypothesis and θ_b represents the set of nuisance parameters that maximizes the likelihood for the b hypothesis.

The confidence level for the signal+background hypothesis is given by

$$CL_{s+b} = P_{s+b}(\eta \leq \eta_d) = \int_{-\infty}^{\eta_d} \frac{dP_{s+b}}{d\eta} d\eta, \tag{6.13}$$

where the probability distribution function (PDF) P_{s+b} is defined by the distribution of η_d. The η_d distribution is found by running many pseudo-experiments to simulate the outcome of repeated experiments using the value of d. The value η_d is calculated for each pseudo-experiment to get the distribution.

Because the CL_{s+b} estimator can lead to exclusion of signals even when there is no sensitivity, a modified Frequentist confidence level CL_s is used, defined as:

$$CL_s = CL_{s+b}/CL_b, \tag{6.14}$$

where CL_b is the confidence level for the background only hypothesis [79]. The signal hypothesis is excluded at 95% confidence level if CL_s<5%.

6.2 Systematics

The systematic uncertainties are determined by varying the sources of the uncertainties and looking at the resulting output distributions of the Boosted Decision Tree. We take into consideration two types of systematics: scale systematics and shape dependent systematics. For the scale systematics the variation of the uncertainty changes the event yield but does not change the output value of the BDT. The shape systematics change both the yield and the shape of the BDT output.

Systematic	Variable Uncertainty (%)	Total Background Uncertainty (%)
Luminosity	6.1	6.1
μ identification (each)	1.4	0.75
$Z + lp\ \sigma$	10	9
$Z + hf\ \sigma$	30	20
Top σ	10	0.5
Diboson σ	10	0.9
HF Scale	12	6
Multijet $\mu\mu$	50	2

Table 6.1: Systematics uncertainties for scale systematics with the error quoted as a percentage of the individual variable in the second column and the effect on the total background prediction in the third column.

6.2.1 Scale systematics

All sources of scale systematics are summarized in Table 6.1 and the overall effect on the acceptance or scaling is listed as a percentage. The uncertainty on the measurement of the luminosity is 6.1% [80] and it is applied to all samples. The uncertainty for the multijet background is taken from the uncertainty on the multijet scale factor and is estimated to be 50% for the dimuon sample. Uncertainties of 10% are assigned to the theoretical cross sections for $\mathrm{Z + lp}$ [63] and $\mathrm{t\bar{t}}$ processes, 7% for diboson processes, and 30% for $\mathrm{Z + b\bar{b}/c\bar{c}}$ processes.

6.2.2 Shape systematics

All shape systematics are summarized in Table 6.2 as a percentage of change in all of the samples. The shape systematic uncertainties were fluctuated individually in the analysis and the shape of the BDT output was used as the error on that systematic.

The way these systematics are obtained is the following:

- Separate values for fluctuating the Jet Energy Scale (JES) by $\pm 1\sigma_{JES}$, the jet resolution $\pm 1\sigma_{RES}$ and jet reconstruction efficiency $-1\sigma_{JetReco}$ (the reconstruction efficiency in data cannot be higher than in MC) were computed and used as input for the BDT.

- The Tag Rate Function (TRF) uncertainties were used to reweight the tag-

Sample	JES	Jet ID	TRF b/c	TRF lp	B Frag	Zp_T	VCJ SF	$\Delta\phi(j,j)$	Triger	m_{jj}
ZH (115)	11	1.4	1.0	0	1.0	0	3.0	0	0.1	0
Total	10	0.6	9.7	4.7	0.5	3.5	3.0	0.8	0.1	0.7
Z+lp	19.0	0.1	0	21	0	4.2	3.0	1.0	0.05	1.0
Z+bb	7.5	0.1	11	0	0.8	3.9	3.0	1.0	0.1	1.0
Z+cc	8.3	1.8	15	0	0.1	3.7	3.0	1.0	0.1	1.0
tt	0.0	1.4	4.9	0	0.8	0	3.0	0	0.1	0
WZ	6.7	1.0	0	11	0.4	0	3.0	0	0.1	0
ZZ	3.8	1.0	0	11	0.4	0	3.0	0	0.1	0

Table 6.2: Shape dependent systematic uncertainties. The table lists the percentage change in the predicted number of events for each background sample and each shape dependent systematic.

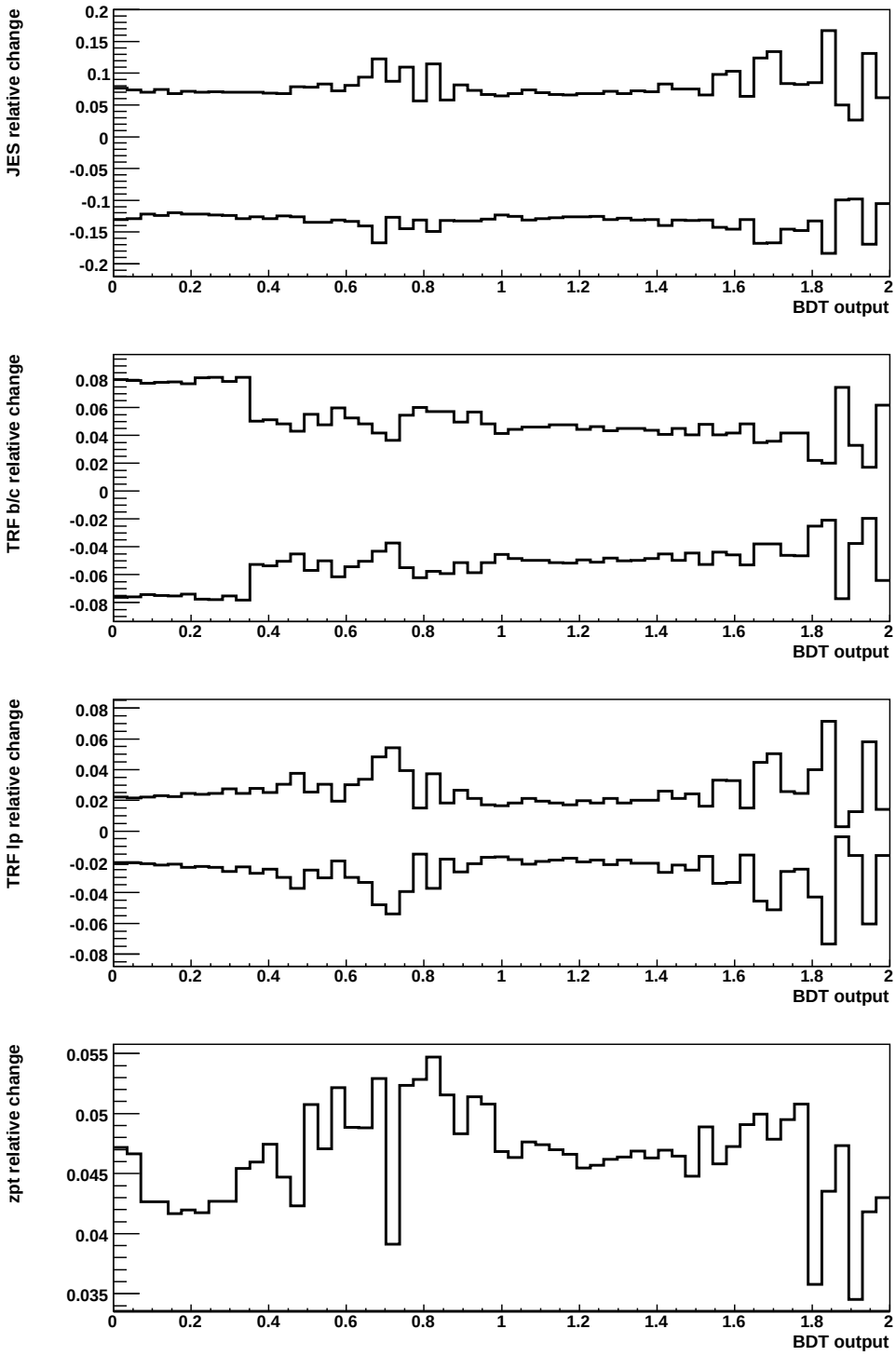

Figure 6.1: Relative change per BDT output bin when floating the shape systematic source by $\pm 1\sigma$. Plots are for a Higgs mass of 115 GeV. Bins from 0 to 1 correspond to the 2 Loose b-tag sample output and bins 1 to 2 correspond to the 1 VeryTight b-tag sample output.

ging probabilities for each jet individually. The TRF was fluctuated separately for the light and heavy quark contributions as these parameterizations have different uncertainties depending upon jet p_T and η;.

- The taggability was applied directly to the MC but the event weights were fluctuated using the data taggability error as measured for each jet and parameterized in p_T and η.

- The covariance matrix for the Z-p_T reweighting parametrization was used to determine the uncertainty on the N_{jet} dependent Z p_T reweighting described in Chapter 4.

- The uncertainty on the PDF (parton distribution function) was evaluated based on the 40 PDF error sets in CTEQ6M [57] and used to estimate the uncertainty on the acceptance and normalization.

- For the $\Delta\phi$ reweighting of the jets the covariance matrix of the reweighting function was used.

- The trigger parametrization was varied by going to a more restrictive trigger list.

- The systematic on the reweighting of the b-fragmentation was determined by changing the tune from the Aleph-Opal-Delphi tune (AOD) to the SLD fragmentation tune.

- The dijet invariant mass distribution for the ALPGEN samples was found not to agree with the more precise Sherpa [81] calculations for this distribution. In order to estimate the systematic uncertainty from this discrepancy, the invariant mass distributions were shifted up and down based upon the difference between ALPGEN and Sherpa.

In Figure 6.1 the relative changes with respect to the nominal BDT output are presented for the largest shape systematic sources.

6.3 Results

The confidence level is calculated given the BDT output distributions for data, signal and background. If the CL_s is greater than 5%, the signal is multiplied by a factor until $CL_s < 5\%$. This factor is the ratio of the upper limit of the Higgs production cross section to the predicted cross section $\sigma^{limit}/\sigma^{predicted}$, where $\sigma^{predicted}$ is the cross section used to generate the signal distribution. All upper

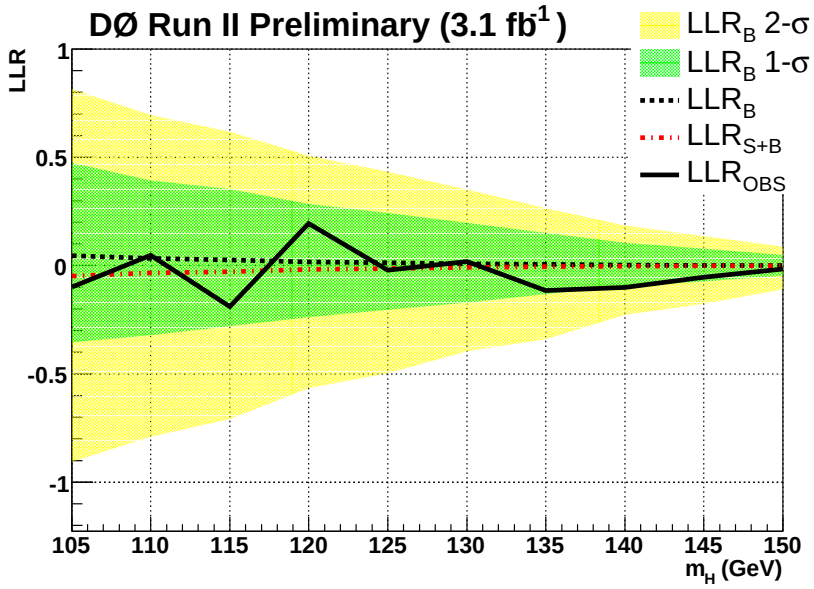

Figure 6.2: Log-likelihood ratio for the ZH $\rightarrow \mu\mu b\bar{b}$ analysis.

limits are calculated using 10^5 pseudo-experiments and requiring that $4.9\% \leq CL \leq 5.1\%$.

Figure 6.2 shows the log-likelihood ratio η_d (LLR) for each Higgs mass point considered and having the single-tag and double-tag samples combined. Included in the figure are the LLR for the signal+background hypothesis LLR_{s+b}, background-only hypothesis LLR_b, and the observed data LLR_{obs} are shown. Also the 68% and 95% CLintervals for LLR_b are indicated by shaded bands.

The LLR plot gives the following information on the characteristics of the analysis:

- The separation between LLR_b and LLR_{s+b} provides a measure of the overall power of the search. This is a measure of the ability of this analysis to discriminate between the signal+background and background-only hypotheses where the signal+background hypothesis assumes the Standard Model Higgs production cross section.

- The width of the LLR_b distributions (shown in these plots as 1 and 2 sigma deviations from the mean) provides an estimate of how sensitive the analysis is to a signal-like fluctuation in data, in the presence of statistical and systematic uncertainties.

- The value of LLR_{obs} relative to LLR_{s+b} and LLR_b indicates whether the data distribution is more signal+background like or background like. The significance of any departure of LLR_{obs} from LLR_b can be evaluated in terms of the width of the LLR_b distribution.

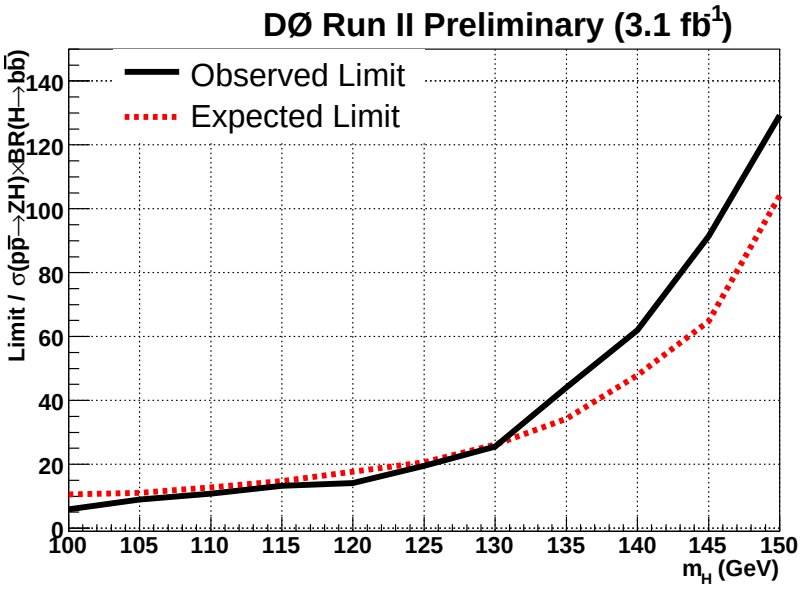

Figure 6.3: Expected (median) and observed 95% CL cross section ratios for the ZH $\rightarrow \mu\mu b\bar{b}$ in the $m_{\mathrm{H}} = 100 - 150$ GeV mass range.

$\mathrm{M_H}$(GeV)	100	105	110	115	120	125	130	135	140	145	150
Exp/SM	9.29	11.1	12.8	14.7	17.7	20.7	26.2	34.2	47.9	64.9	104
Obs/SM	7.7	9.0	10.9	13.3	14.2	19.5	25.6	44.1	62.0	91.5	129.3

Table 6.3: Measured and expected limit on the Standard Model Higgs production cross-section in the ZH $\rightarrow \mu\mu b\bar{b}$ channel after combining the 1 Very Tight and 2 Loose b-tag samples.

Figure 6.3 shows the ratio of the cross section limit times branching ratio $\sigma(\mathrm{ZH}) \times B(\mathrm{H} \rightarrow b\bar{b})$ to the Standard Model expectation for the ZH $\rightarrow \mu\mu b\bar{b}$ for the combined single-tag and double-tag samples. In Table 6.3 the ratios for the 11 Higgs mass points are given.

Chapter 7

Conclusions and outlook

We finished the previous chapter presenting the results for a SM like Higgs boson in the ZH $\rightarrow \mu\mu b\bar{b}$ channel in 3.1 fb^{-1} of data collected using the DØ detector. The search presented here in this channel is not sensitive enough to probe the existence of the Higgs mechanism. However it does improve compared to previous searches performed at DØ in the same channel [82, 83]. The improvement is due to the good performance of the Boosted Decision Trees as a discriminant and the inclusion of new powerful variables as inputs to the BDTs.

Looking into Table 6.3 the search presented here would be sensitive to a SM like Higgs with a cross-section 6 to 100 times higher than the one expected from theory. However as mentioned in Section 1.4 this is not the only channel in which the Higgs boson can be produced at the Tevatron. The method for setting upper limits described in Section 6.1 can be applied to more than one channel and all the channels studied can be combined. In this way the search sensitivity at the Tevatron is maximized and the limits that are finally set on the SM Higgs boson production are more stringent in comparison to any single channel analysis.

The similar channels are first combined and then there is the combination with the other channels. In the same "family" as the channel presented here are the analysis where the Z boson is reconstructed from :

- two electrons [84];
- one muon and a second muon whose reconstruction in the detector is an isolated track [85];
- one electron and an intercryostat detector electron candidate [86].

While the sensitivity of the di-electron channel is of the same order as the sensitivity of the di-muon channel, the other two channels have a weaker sensitivity, but still quite good compared with other channels considered in the full combination. All four channels are combined for setting a common limit on SM Higgs

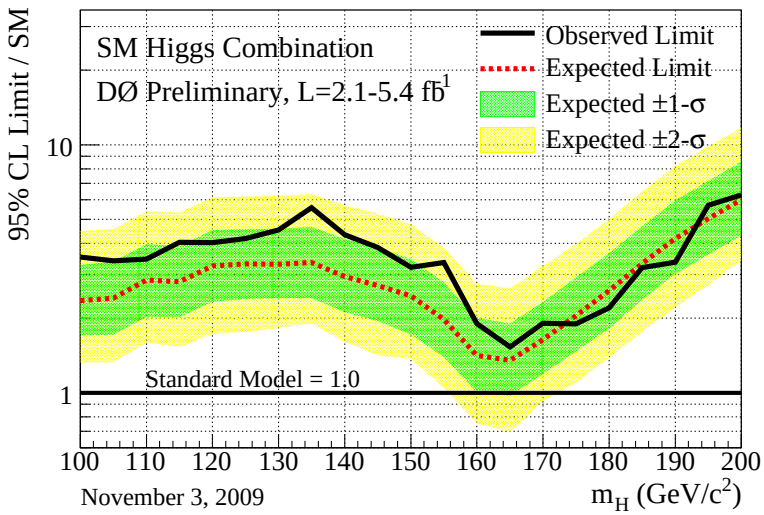

Figure 7.1: Expected and observed 95% CL upper limits on the ratios to the SM cross section, as a function of the Higgs boson mass for the combined DØ analysis.

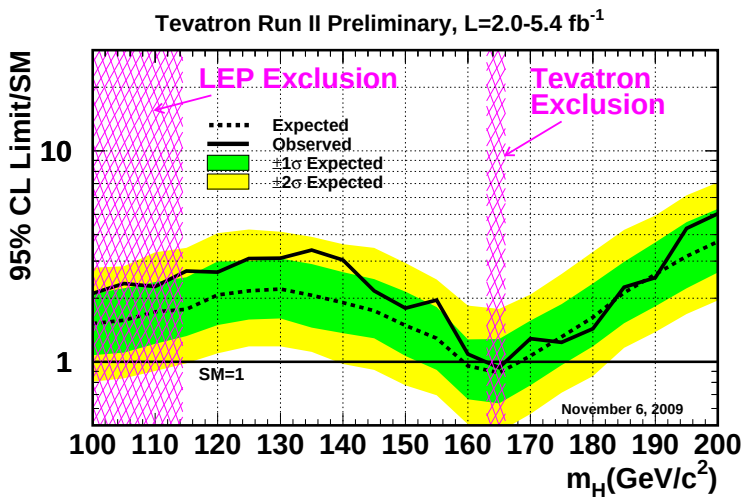

Figure 7.2: Expected and observed 95% CL upper limits on the ratios to the SM cross section, as a function of the Higgs boson mass for the combined CDF and DØ analysis. A SM like Higgs with a mass of 163 to 166 GeV is excluded at 95% CL.

production [87] using up to 4.2 fb^{-1} of available data. The expected limit coming from this combination (9.1 times the SM Higgs cross section for a 115 GeV mass

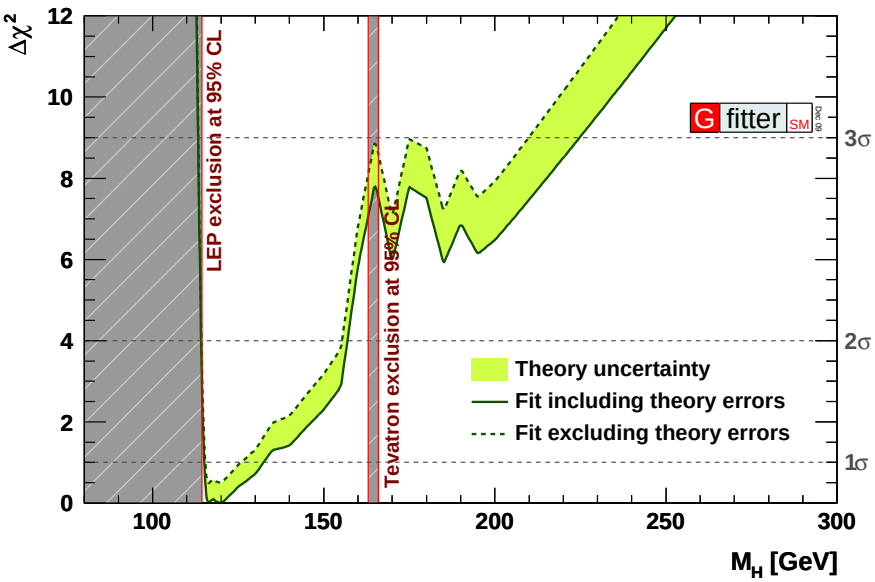

Figure 7.3: $\Delta\chi^2$ of the fit including direct searches. The solid (dashed) lines give the results when including (ignoring) theoretical errors [89].

Higgs [87]) is at the same level as the limit set in the WH channel in 5.0 fb^{-1} of data (6.9 times the SM Higgs cross section for a 115 GeV mass Higgs [88]), a channel that has a much higher cross-section at Tevatron (see Figure 1.4). The increase in sensitivity between the channel presented here and the combination of all ZH channels is about 30%.

The combination of Higgs search channels is continued for all search channels at DØ and a combined limit on the Higgs production is obtained [90]. This limit can be seen in Figure 7.1. Combining the results of DØ and CDF gives the Tevatron limit [91] and this limit can be seen in Figure 7.2. One notices that a Higgs of mass between 163 and 166 GeV is by now excluded at 95% CL. Maintaining the same sensitivities as today for the analyses, if no Higgs boson exists with such a mass, the region of Higgs mass exclusion will grow with the growth of data available.

The LLR for the Tevatron searches can be included in a modified version of the electroweak fit procedure presented in Section 1.3.2 including also the LEP direct Higgs boson search information [92]. The new $\Delta\chi^2$ obtained can be seen in Figure 7.3. We notice that this fit favors a SM Higgs boson with a mass of $116^{+15.6}_{-1.3}$ GeV, which falls in a region in which the Tevatron's sensitivity to the Higgs searches is not maximal and more integrated luminosity is needed in order to probe the SM Higgs boson cross section.

However the Tevatron is expected to run another two more years until 2011 and deliver up to a total of 11 to 12 fb^{-1} per experiment. Experiments are expecting

to further improve the search sensitivity. For example in the ZH $\rightarrow l^+l^-b\bar{b}$ channel the following improvements are foreseen: a) addition of discriminating variables to the list previously presented and b) the use of Random Forests, which have proven to be a better discriminant than the BDTs. With all these improvements the exclusion of SM Higgs mass intervals will grow at the Tevatron over the next years. Evidence of the SM Higgs is also possible depending on whether a Higgs boson exists and where the Higgs mass lies.

Bibliography

[1] E. Noether, *Invariante Variationsprobleme*, *Nachr. d. König. Gesellsch. d. Wiss. zu Göttingen, Math-phys. Klasse* (1918) 235–257.

[2] M. Kaku, *Quantum field theory: A Modern introduction.* 1993.

[3] M. E. Peskin and D. V. Schroeder, *An Introduction to quantum field theory.* 1995.

[4] P. W. Higgs, *Broken symmetries and the masses of gauge bosons*, *Phys. Rev. Lett.* **13** (1964) 508–509.

[5] A. Djouadi, *The Anatomy of electro-weak symmetry breaking. I: The Higgs boson in the standard model*, *Phys. Rept.* **457** (2008) 1–216, [hep-ph/0503172].

[6] K. Riesselmann, *Limitations of a standard model Higgs boson*, [hep-ph/9711456].

[7] ALEPH Collaboration *et al.*, *Precision Electroweak Measurements and Constraints on the Standard Model*, [0911.2604].

[8] O. Brein, A. Djouadi and R. Harlander, *NNLO QCD corrections to the Higgs-strahlung processes at hadron colliders*, *Phys. Lett.* **B579** (2004) 149–156, [hep-ph/0307206].

[9] A. Djouadi, J. Kalinowski and M. Spira, *HDECAY: A program for Higgs boson decays in the standard model and its supersymmetric extension*, *Comput. Phys. Commun.* **108** (1998) 56–74, [hep-ph/9704448].

[10] C. Gatusso *et al.*, *Accelerator Concepts*, 2006. http://www-bdnew.fnal.gov/operations/rookie_books/Concepts_v3.1.pdf.

[11] J. Morgan, *The Antiproton Source Rookie Book*, 2006. http://www-bdnew.fnal.gov/operations/rookie_books/Pbar_V1_1.pdf.

[12] *Tevatron Rookie Book*, 2006.
http://www-bdnew.fnal.gov/operations/rookie_books/Tevatron_v1.pdf.

[13] E. McCrory, V. Shiltsev, A. J. Slaughter and A. Xiao, *Fitting the luminosity decay in the Tevatron*, *Proceedings of Particle Accelerator Conference (PAC 05), Knoxville, Tennessee, 16-20 May 2005.*

[14] *DØ Run II Coordination. DØ Operation Webpage*, 2009.
http://www-d0.fnal.gov/runcoor/.

[15] **DØ** Collaboration, S. Abachi *et al.*, *The DØ Detector*, *Nucl. Instrum. Meth.* **A338** (1994) 185–253.

[16] **DØ** Collaboration, V. Abazov *et al.*, *The Upgraded DØ Detector*, *Nucl. Instrum. Meth. A* **565** (2006) 463.

[17] **DØ** Collaboration, R. Angstadt *et al.*, *The Layer 0 Inner Silicon Detector of the DØ Experiment*, [0911.2522].

[18] R. Lipton, *Lifetime of the DØ Silicon Tracker*, *DØNote* **4077** (2003).

[19] A. Khanov and F. Rizatdinova, *The effect of losing the inner silicon layer on b-tagging performance in Run IIA*, *DØNote* **4199** (2003).

[20] S. Ahmed, R. Lipton, B. Wijngaarden, S. Duensing, A. Naumann and S. de Jong, *DØ SMT Radiation Protection System*, *DØNote* **3915** (2001).

[21] S. Ahmed, R. Lipton, B. Wijngaarden, S. Duensing, A. Naumann and S. de Jong, *DØ SMT Radiation Monitoring System*, *DØNote* **4022** (2002).

[22] DØ Collaboration, *Test Beam Studies of the DØ Calorimeter with 2-150 GeV Beams*, *DØNote* **1466** (1992).

[23] S. Klimenko, J. Konigsberg and T. M. Liss, *Averaging of the inelastic cross sections measured by the CDF and the E811 experiments*, *Fermilab Note* **741**.

[24] B. Casey, Y. Corcoran, M. Enari, M. Prewitt and G. Snow, *Determination of the D0 RunIIb Luminosity Constants*, *DØNote* **5559** (2007).

[25] M. Abolins *et al.*, *Design and Implementation of the New DØ Level-1 Calorimeter Trigger*, *Nucl. Instrum. Meth.* **A584** (2008) 75–97 [0709.3750].

[26] C. C. Clement, F. Deliot, T. Golling, K. Haganaki, B. Leonhardt, M. Mulders, E. Nurse, S. Soldner-Remboldt and J. Stark, *MuonID Certification for p14*, *DØNote* **4350** (2004).

[27] S. Cho, F. Deliot, M. Eads, D. Hedin, H. Lee, B. Tuchming and Y. Yatsunenko, *Muon ID Certification for p20 data*, *DØNote* **5824** (2008).

[28] P. Calfayan, T. Gadfort, G. Hesketh, V. Lesne, M. Owen, R. Stroehmer, V. Sharyy and B. Tuchming, *Muon ID Certification for p17 data*, *DØNote* **5157** (2006).

[29] M. Arthaud, F. Deliot, B. Tuchming, V. Sharyy and D. Vilanova, *Muon Momentum Oversmearing for p20 Data*, *DØNote* **5449** (2007).

[30] U. Baur, R. K. Ellis and D. Zeppenfeld, *QCD and weak boson physics in Run II. Proceedings, Batavia, USA, March 4-6, June 3-4, November 4-6, 1999*, *Prepared for Physics at Run II: QCD and Weak Boson Physics Workshop: Final General Meeting, Batavia, Illinois, 4-6 Nov 1999.*

[31] U. Bassler and G. Bernardi, *Towards a Coherent Treatment of Calorimetric Energies: Missing Transverse Energy, Jets, E.M. Objects and the T42 Algorithm*, *DØNote* **4124** (2003).

[32] J.-R. Vlimant, U. Bassler, G. Bernardi and S. Trincaz-Duvoid, *Technical description of the T42 algorithm for the calorimeter noise suppression*, *DØNote* **4146** (2003).

[33] G. Bernardi, E. Busato and J.-R. Vlimant, *Improvements from the T42 Algorithm on Calorimeter Objects Reconstruction*, *DØNote* **4335** (2004).

[34] K. DeVaughan, G. Golovanov, U. Heintz, S. Jabeen, A. Kupco, M. Padilla, V. Parihar and A. Tanasijczuk, *Jet Energy Scale Determination for DØ Run IIb*, *DØNote* **5801** (2008).

[35] M. Voutilainen and C. Royon, *Jet pT resolution using v7.1 JES for p17 data*, *DØNote* **5381** (2007).

[36] N. Makovec and J.-F. Grivaz, *Shifting, Smearing and Removing Simulated Jets*, *DØNote* **4914** (2005).

[37] S. Trincaz-Duvoid and P. Verdier, *Missing ET Reconstruction in p17*, *DØNote* **4474** (2004).

[38] S. Calvet, P. Verdier and E. Kajfasz, *Towards MissingET Certification and Unclustered Energy Studies*, *DØNote* **4927** (2005).

[39] G. Borissov, *Status of DØ track reconstruction. Talk at All DØ Meeting, 14 February 2003.*

[40] G. Borissov, *Ordering a chaos or ... technical details of AA tracking. Talk at All DØ Meeting, 23 February 2003.*

[41] A. Khanov, *HTF: histograming method for finding tracks. The algorithm description*, *DØNote* **3778** (2000).

[42] H. Greenlee, *The DØ Kalman track fit*, *DØNote* **4303** (2003).

[43] H. Greenlee, *The DØ interacting propagator*, *DØNote* **4293** (2003).

[44] A. Schwartzman and C. Tully, *Primary Vertex Reconstruction by Means of Adaptive Vertex Fitting*, *DØNote* **4918** (2005).

[45] A. Schwartzman and M. Narain, *Probabilistic Primary Vertex Selection*, *DØNote* **4042** (2002).

[46] A. Schwartzman and M. Narain, *Secondary Vertex Reconstruction using the Kalman Filter*, *DØNote* **3908** (2001).

[47] Y. Peters, H. Greenlee, A. Haas and A. Schwartzman, *Optimization of the Secondary Vertex Tagger in p17*, *DØNote* **5265** (2006).

[48] D. Bloch and B. Clement, *Update of the JLIP b-tagger Performance in p14/pass2 with JES 5.3*, *DØNote* **4824** (2005).

[49] R. Demina, A. Khanov, F. Rizatdinova and E. Shabalina, *Measurement of b-tagging efficiency and mis-tagging rates with CSIP method*, *DØNote* **4133** (2003).

[50] Y. Yvonne Peters, H. Greenlee, A. Haas and A. Schwartzman, *Optimization of the Secondary Vertex Tagger in p17*, *DØNote* **5265** (2006).

[51] T. Scanlon, *A Neural Network b-tagging Tool*, *DØNote* **4889** (2005).

[52] T. T. Gadfort, A. Haas, D. Johnston, D. Lincoln, T. Scanlon and S. Schlobohm, *Performance of the DØ NN b-tagging Tool on p20 Data*, *DØNote* **5554** (2007).

[53] *DØ Data Quality Coordination*, . `http://www-d0.fnal.gov/computing/data_quality/`.

[54] T. Sjostrand, S. Mrenna and P. Skands, *PYTHIA 6.4 Physics and Manual*, *JHEP* **05** (2006) 026 [`hep-ph/0603175`].

[55] M. L. Mangano, M. Moretti, F. Piccinini, R. Pittau and A. D. Polosa, *ALPGEN, a generator for hard multiparton processes in hadronic collisions*, *JHEP* **07** (2003) 001, [hep-ph/0206293].

[56] S. Hoche *et al.*, *Matching parton showers and matrix elements*, [hep-ph/0602031].

[57] D. Stump *et al.*, *Inclusive jet production, parton distributions, and the search for new physics*, *JHEP* **10** (2003) 046, [hep-ph/0303013].

[58] **CDF** Collaboration, R. Field and R. C. Group, *PYTHIA tune A, HERWIG, and JIMMY in Run 2 at CDF*, [hep-ph/0510198].

[59] Y. Fisyak and J. Womersley, *D0gstar DØ GEANT Simulation of the Total Apparatus Response*, *DØNote* **3191** (1997).

[60] M. Goossens *et al.*, *GEANT, detector description and simulation and simulation tool. GEANT users's guide*, *CERN* (1994).

[61] G. Hesketh *wz_cafreco*. DØWiki https://plone4.fnal.gov/P1/D0Wiki/comp/caf/wz_cafreco/.

[62] J. Hobbs, T. Nunnemann and R. Van Kooten, *Study of the* $\mathrm{p\bar{p}} \to \mathrm{Z}/\gamma^* \to \mathrm{ee}$ *and* $\mathrm{p\bar{p}} \to \mathrm{Z}/\gamma^* \to \mu\mu$ *Event Yields as a Luminosity Cross Check*, *DØNote* **5268** (2006).

[63] J. M. Campbell, R. K. Ellis and D. L. Rainwater, *Next-to-leading order QCD predictions for W + 2jet and Z + 2jet production at the CERN LHC*, *Phys. Rev.* **D68** (2003) 094021, [hep-ph/0308195].

[64] J. M. Campbell and R. K. Ellis, *An update on vector boson pair production at hadron colliders*, *Phys. Rev.* **D60** (1999) 113006, [hep-ph/9905386]. See also: http://mcfm.fnal.gov.

[65] S. Calvet, A. Duperrin, J.-F. Grivaz and E. Kajfasz, *Reweighting of Alpgen's* Z^0 *transverse momentum in multijets topologies with 1* fb^{-1} *of RunIIa data*, *DØNote* **5367** (2007).

[66] M. Shamim and T. Bolton, *Generator Level Reweighting of* pT *of Z Boson*, *DØNote* **5565** (2008).

[67] E. Barberis, G. Cerminara, G. Hesketh, J. Hobbs, E. Strauss, T. Wyatt and D. Wood, $\mathrm{ZZ} \to \mathrm{l^+l^-}\nu\bar{\nu}$ *production in* $\mathrm{p\bar{p}}$ *collisions at* $\sqrt{\mathrm{s}} = 1.96\mathrm{TeV}$, *DØNote* **5574** (2008).

[68] S. J. Parke and S. Veseli, *Distinguishing W H and W b anti-b production at the Fermilab Tevatron*, *Phys. Rev.* **D60** (1999) 093003, [hep-ph/9903231].

[69] G. Bernardi *et al.*, *Search for WH associated production using a Neural Net and Matrix Element approach, with 2.7 fb^{-1} of data*, *DØNote* **5714** (2008).

[70] H.-J. Yang, B. P. Roe and J. Zhu, *Studies of boosted decision trees for Miniboone particle identification*, *Nucl. Instrum. Meth.* **A555** (2005) 370–385 [physics/0508045].

[71] H.-J. Yang, B. P. Roe and J. Zhu, *Studies of stability and robustness for artificial neural networks and boosted decision trees*, *Nucl. Instrum. Meth.* **A574** (2007) 342–349,.

[72] **DØ** Collaboration, V. M. Abazov *et al.*, *Evidence for production of single top quarks and first direct measurement of* |V(tb)|, *Phys. Rev. Lett.* **98** (2007) 181802, [hep-ex/0612052].

[73] Y. Freund and R. Schapire, *A Decision-Theoretic Generalization of On-Line Learning and an Application to Boosting*, *J. of Computer and System Science* **55** (2007) 119–139.

[74] A. A. Hoecker, P. Speckmayer, J. Stelzer, J. Therhaag, E. von Toerne and H. Voss, *TMVA - Toolkit for Multivariate Data Analysis*, [physics/0703039v5].

[75] A. L. Read, *Presentation of search results: The CL(s) technique*, *J. Phys.* **G28** (2002) 2693–2704.

[76] W. Fisher, *Collie: A Confidence Level Limit Evaluator*, *DØNote* **5595** (2008).

[77] W. Fisher, *Calculating Limits for Combined Analyses*, *DØNote* **4975** (2005).

[78] W. Fisher, *Systematics and Limit Calculations*, *DØNote* **5309** (2006).

[79] T. Junk, *Confidence Level Computation for Combining Searches with Small Statistics*, *Nucl. Instrum. Meth.* **A434** (1999) 435–443, [hep-ex/9902006].

[80] **DØ** Collaboration, T. Andeen *et al.*, *The D0 experiment's integrated luminosity for Tevatron Run IIa*, *FERMILAB-TM-2365*.

[81] T. Gleisberg *et al.*, *Event generation with SHERPA 1.1*, *JHEP* **02** (2009) 007, [0811.4622].

[82] **DØ** Collaboration, V. M. Abazov *et al.*, *Search for a Higgs boson produced in association with a Z boson in $p\bar{p}$ collisions*, *Phys. Lett.* **B655** (2007) 209–216, [0704.2000].

[83] D. Collaboration, *A Search for $ZH(\to e^+e^-b\bar{b})$ and $ZH(\to \mu^+\mu^-b\bar{b})$ with the DØ Detector in $p\bar{p}$ Collisions at $\sqrt{s} = 1.96$ TeV*, *DØ Conference Note* **5570** (2008).

[84] B. Calpas, K. Chan, S. Desai, E. Nagy and T. Yasuda, *Search for ZH Production in the $e^+e^-b\bar{b}$ Channel*, *DØNote* **5804** (2008).

[85] L. Ancu, J. BackusMayes, S. Desai, M. Kirby, M. Mulhearn and E. Strauss, *Preselection for the ZH Search in the $\mu^+\mu^-b\bar{b}$ channel using 4.1 fb^{-1} of p17 and p20 data*, *DØNote* **5842** (2009).

[86] B. Calpas and T. Yasuda, *Preselection for the ZH Search in the* $e^+e^-b\bar{b}$ *channel where one of the electrons is in the ICR*, *DØNote* **5840** (2009).

[87] L. Ancu, J. BackusMayes, B. Calpas, K. Chan, S. Desai, M. Kirby, M. Mulhearn, E. Nagy, E. Strauss and T. Yasuda, *Search for* $ZH \to llbb$ *in 4.1 fb^{-1} of p17 and p20 data using a Boosted Decision Tree in dimuon and dielectron events*, *DØNote* **5862** (2009).

[88] D. Collaboration, *Search for WH associated production using neural networks with 5.0 fb^{-1} of Tevatron data*, *DØ Conference Note* **5972** (2009).

[89] A Generic Fitter Project for HEP Model Testing Homepage, *New results of the SM fit using latest results from Tevatron Higgs mass combination using up to 5.4* fb^{-1}, *GFitter SM fit December 2009* (2009). http://gfitter.desy.de/GSM/.

[90] D. Collaboration, *Combined Upper Limits on Standard Model Higgs Boson Production from the DØ Experiment in 0.9-4.2 fb^{-1}*, *DØ Conference Note* **5902** (2009).

[91] The CDF Collaboration, the DØ Collaboration, the Tevatron New Physics and Higgs Working Group, *Combined CDF and DØ Upper Limits on Standard Model Higgs- Boson Production with 2.1 - 5.4 fb^{-1} of Data*, [0911.3930].

[92] H. Flacher *et al.*, *Gfitter - Revisiting the Global Electroweak Fit of the Standard Model and Beyond*, *Eur. Phys. J.* **C60** (2009) 543–583, [0811.0009].

Summary

The Standard Model describes with a very good accuracy all interactions of the, so far, known elementary particles. However the Higgs mechanism, which gives rise to the observed mass of these particles, has not yet been confirmed. The Higgs particle has not yet been observed, and the observation or exclusion is an important test of the Standard Model. The Standard Model does not predict the mass of the Higgs particle, however it does impose some limits on the range in which this mass can lie. In direct searches a Higgs with a mass smaller than 114.4 GeV and within 162 GeV and 166 GeV has been excluded at 95% CL at the LEP and the Tevatron colliders. The analysis presented in this thesis is aimed to search for the $ZH \rightarrow \mu\mu b\bar{b}$ events in 3.1 fb^{-1} of data collected with the DØ detector in $p\bar{p}$ collisions at $\sqrt{s} = 1.96$ TeV.

The analysis relies on good tracking, calorimetry and muon reconstruction. The signature for this search are two muons compatible with the decay of a Z boson and two b-jets. The Higgs mass is reconstructed using either 2 b-jets or one b-jet and the other most energetic jet in the event. Backgrounds considered are $Zb\bar{b}$, $Zc\bar{c}$, Z + light jets, $t\bar{t}$, di-boson backgrounds (WW, WZ, ZZ) and multijet QCD background.

The data used for this analysis is selected using loose criteria in order to have the highest acceptance. There is no explicit trigger requirement that the events have to pass. The events are required to have two isolated muons with $p_T > 10$ GeV and at least two jets, one with $p_T > 20$ GeV and the second one with $p_T > 15$ GeV. The invariant mass of the two muons has to be between 70 GeV and 130 GeV. The backgrounds are reduced by asking that some of the jets in the event are b-tagged. We have considered two orthogonal data samples: one with both jets passing loose b-tagging criteria and one orthogonal sample where only one jet is passing tighter b-tagging criteria while there are no other loose b-tagged jets. Applying b-tagging provides a good rejection of light jet backgrounds and enriches the signal in the sample. The single tagged sample contains 217 events with an expected background of 229.5 ± 1.3 and a signal contribution of 0.611 ± 0.005 events for a 115 GeV mass Higgs. The double tagged sample contains 161 events with an expected background of 148.8 ± 1.0 and a signal contribution of 0.856 ± 0.008

events.

Boosted decision trees are used to improve the separation between signal and background. As inputs for the decision tree a total of 17 variables are used. A kinematic fit of the event is performed and variables computed after this fit are among the input variables to the decision tree. Also variables that distinguish the spin correlations between background and signal events are used as input. The trees are trained on simulated events. Two boosted decision trees are trained for each Higgs mass point hypothesized: one for the single b-tagged sample and one for the double b-tagged sample. The boosted decision tree has proven a powerful tool not only in increasing the separation between signal and background but also in making use of as much information as possible about the events by combining a great number of inputs. The boosted decision tree has been trained with simulated events to assign high output values to signal and low output values to background events. At high boosted decision tree output values the signal to background separation was significantly improved.

The observed data were found to be consistent with background and we set an upper limit on the Higgs production cross section at 95% CL. A modified frequentist method is used to compute the upper limit confidence level $\mathrm{CL_s} = 5\%$. The systematic uncertainties are taken into account by considering perturbations of the predicted signal and background contributions. The impact of systematics is reduced by performing fits to the signal+background hypothesis and background-only hypotheses. By choosing separately the best fit for the background prediction outside the expected signal region in the two hypotheses the fluctuations due to the systematics are constrained.

The observed upper limit ranges from 7.7 times the SM prediction for a 100 GeV mass Higgs to 129.3 times the SM prediction for a 150 GeV mass Higgs. The result of this analysis was combined with the analysis where the Z boson decays to electrons giving an upper limit of 9.1 times the expected SM cross section for a 115 GeV mass Higgs. Other channels are explored at DØ (WH, $\mathrm{H} \to \mathrm{WW}$, $\mathrm{ZH} \to \nu\nu\mathrm{b\bar{b}}$, $\mathrm{H} \to \gamma\gamma$) and can be all combined into a single DØ upper limit. The current upper limit for a 115 GeV Higgs is 4.05 times the SM cross section prediction. In combination with the other Tevatron experiment, CDF, the current upper limit for a 115 GeV Higgs is 2.7 times the SM cross section prediction. In order to exclude a 115 GeV Higgs, a better sensitivity has to be gained. This can be achieved by higher integrated luminosity and improvements in the discriminant algorithms used. The Tevatron is expected to deliver $10 - 12\ \mathrm{fb}^{-1}$ to the experiments and a 3σ evidence for a low mass Higgs should become possible.

Samenvatting

Het standaardmodel beschrijft alle tot nu toe bekende elementaire deeltjes en de elektromagnetische, sterke en zwakke kernkracht tussen die deeltjes met zeer grote nauwkeurigheid. Om de theorie intern consistent te maken, is een manier nodig om massa te geven aan de overbrengers van de zwakke kernkracht, de W- en Z-bosonen. Het Higgs-mechanisme, dat verklaart hoe spontane elektrozwakke symmetriebreking deze massa's voortbrengt, is opgenomen in het standaardmodel, maar is nog niet experimenteel bevestigd. Voor dit mechanisme is er een Higgs-veld nodig, en een daarmee geassocieerd deeltje: het Higgs-boson, of kortweg Higgs. Veel eigenschappen van het Higgs-boson liggen al vast, maar de koppeling van Higgs-deeltjes met elkaar – en daarmee zijn eigen massa – is nog niet bekend. Wel is door de LEP- en Tevatron-versnellers met 95% zekerheid uitgesloten dat de massa onder de 114,4 GeV/c^2 of tussen de 162 en 166 GeV/c^2 ligt.

In dit proefschrift wordt de analyse beschreven waarin gezocht wordt naar een Higgs-boson (H) die van een Z-boson (Z) wordt afgestraald, waarbij het Higgs vervalt in twee *bottom*-quarks (b) en Z in twee muonen (μ); in het kort: HZ $\rightarrow$ $\mu\mu$bb. Naar dit kanaal is gezocht door met de DØ-detector te kijken naar proton-antiprotonbotsingen bij een zwaartepuntsenergie van 1,96 TeV, met 3,1 fb^{-1} geïntegreerde luminositeit.

Voor deze analyse zijn in het bijzonder een goede reconstructie van de trajecten van geladen deeltjes, goede energiemetingen met de calorimeter en goede identificatie van muonen van belang. Zo kunnen de karakteristieke eigenschappen van dit kanaal, twee muonen met een gezamenlijke invariante massa van een Z en twee b-*jets*, zo goed mogelijk herkend worden. Achtergronden die vergelijkbare eigenschappen hebben of daarvoor kunnen worden aangezien, zijn Z met twee of meer quarks, twee *top*-quarks, twee W- of Z-bosonen en instrumentele achtergrond door verkeerde meting van QCD-botsingen waarin alleen quarks en gluonen worden geproduceerd. De achtergronden en het Higgs-signaal worden geschat door Monte-Carlosimulaties waarbij in detail de proton-antiprotonbotsingen en de detectorrespons van de resulterende deeltjes worden nagebootst. De instrumentele achtergronden zijn echter niet makkelijk te simuleren en worden uit controleverzamelingen van de data zelf bepaald met correcties uit Monte-Carlosimulaties.

Voor deze analyse zijn geen specifieke *trigger*-eisen gebruikt, zodat zoveel mogelijk gebeurtenissen van de proton-antiprotoninteracties gebruikt kunnen worden. Er wordt geselecteerd op twee geïsoleerde muonen met ieder een impuls loodrecht op de richting van de protonbundel (p_T) hoger dan 10 GeV en een gezamenlijke invariante massa in de buurt van de Z-massa: tussen de 70 en 130 GeV. Ook moeten er twee bundels hadronische deeltjes, *jets*, met hoge p_T bij de gebeurtenis gezien zijn. Zo'n *jet* duidt namelijk op een quark of gluon in de eindtoestand van de interactie. De achtergrond wordt verder verminderd door b-*tagging*, waarbij criteria in verschillende *jet*-eigenschappen worden opgesteld om b-quarks te kunnen onderscheiden van lichtere quarks en gluonen. De eis die we opleggen is dat twee *jets* aan losse b-criteria voldoen óf dat één *jet* aan striktere criteria voldoet waarbij de andere níét aan de losse voldoet. Deze twee mogelijkheden geven orthogonale verzamelingen die we dus onafhankelijk van elkaar in verdere stappen kunnen gebruiken. De verzameling met de enkele b-*tag* bevat 217 gebeurtenissen met een verwachte achtergrond van $229{,}5 \pm 1{,}3$ en een signaalbijdrage voor een 115 GeV Higgs van $0{,}611 \pm 0{,}005$. De verzameling met de dubbele b-*tag* bevat 161 gebeurtenissen met een verwachte achtergrond van $148{,}8 \pm 1{,}0$ en een signaalbijdrage van $0{,}856 \pm 0{,}008$.

Om scheiding tussen signaal en achtergrond te verbeteren, zijn *boosted decision trees* gebruikt. De gesimuleerde achtergronden en het gesimuleerde signaal worden hierbij in de belangrijkste variabelen bekeken door op een van deze variabelen de beste snede te bepalen en vervolgens de verzamelingen onder en boven de snede weer onafhankelijk in de volgende variabele te bekijken om daarop sneden te bepalen. Dit wordt steeds herhaald, waarbij de variabelen in verschillende volgorden aan de orde komen om uiteindelijk een zo goed mogelijke scheiding te krijgen. In iedere volgende iteratie wordt aan gesimuleerde gebeurtenissen die verkeerd zijn ingedeeld meer gewicht toegekend, het '*boosten*'. Na dit trainen is het Higgssignaal te zien als verschil tussen de gemeten data en de gesimuleerde achtergrond bij hoge uitkomsten van de *tree*, oftewel waar in de training veel gesimuleerde signaalgebeurtenissen terecht kwamen. In deze analyse zijn 17 variabelen gebruikt, zoals eigenschappen van de kinematische fit en variabelen die gevoelig zijn voor de spincorrelatie. Voor beide b-*tag*-verzamelingen zijn onafhankelijke *boosted decision trees* getraind.

De systematische fouten zijn berekend door de onzekerheden in de oorspronkelijke parameters door de hele analyse te laten propageren en de verandering in de uiteindelijke signaal- en achtergrondvoorspelling te bekijken. Voorbeelden van parameters waarvan de onzekerheid erop een bijdrage aan de systematische fout levert, zijn de energiemeting van de *jets* en de kansen van verschillende quarks om voor b-*jet* te worden aangezien.

De gemeten data wijkt niet significant af van de achtergrondverwachting en

we bepalen een bovengrens op de botsingsdoorsnede van Higgs-productie, gemeten in de verwachte botsingsdoorsnede (σ_{SM}). Hierbij is rekening gehouden met verwachte fluctuaties van de achtergrond door gebruik te maken van de gemodificeerde frequentistische methode. De gemeten bovengrens varieert van 7,7 tot 129 σ_{SM} voor Higgs-massa's van 100 tot 150 GeV. De resultaten van deze analyse zijn gecombineerd met de analyse waarbij het Z-boson in twee elektronen vervalt, waaruit de bovengrens 9,1 σ_{SM} voor een 115 GeV Higgs komt. Samen met andere bij DØ onderzochte kanalen kan een gecombineerde DØ-bovengrens berekend worden, namelijk 4,05 σ_{SM} bij een Higgs-massa van 115 GeV. Om het Higgs-boson uit te sluiten – dat wil zeggen een bovengrens meten onder 1 σ_{SM} – of het Higgs-boson waar te nemen, moet een betere gevoeligheid worden bereikt. Dit kan bijvoorbeeld door meer geïntegreerde luminositeit en verbeteringen in de gebruikte analyses. Verwacht wordt dat de Tevatron-versneller 10 tot 12 fb^{-1} aan de experimenten levert en met verwachte analyseverbeteringen is dan een bewijs voor, of uitsluiting van een Higgs-boson met lage massa mogelijk.

Acknowledgements

Working on this thesis was a long trip and during it I had many friends around, without whom the experience wouldn't have been so nice.

First of all I would like to thank my supervisors Sijbrand de Jong and Frank Filthaut. Their confidence in me kept me going even when I was losing it myself. Their guidance over the years was really valuable and was there whenever I needed it.

I remember, looking back at my first days in Nijmegen, the warm greeting that I got from everyone in the group. Gemma, Marjo and Annelies always helped me, and because of them moving from one country to another and all the traveling was much easier. Peter and Charles always had a joke ready to lift my moral.

From the first period in Nijmegen I keep a warm memory of the daily lunch at the Refter with Qin, Bram, Miran, Tamas and Gustavo. These lunches, followed by a coffee and long discussion, made the best midday break. I also recall all the support I got from my fellow Romanians Marcela, Ana and Cata, Delia and Calin, Alice and Lucian, Simona and Saco. They all made my move to a different country easier.

Later I moved to Chicago where I joined the Dutch group there. Unfortunately not long after I arrived Miruna, Pieter and Pieter returned to the Netherlands, but not before introducing me to lots of people and making my transition to yet another country (now also a different continent) easier. Luckily for me I had a big overlap with another part of the Dutch group at Fermilab. Sharing a cubicle with Cristina and Mike Kirby was really nice. I am thankful to Cristina for bearing all my small chat during working hours. During the time spent in Chicago Mike Kirby taught me that doing physics is about enjoying what you do, and he also patiently explained to me, over the years, many things that I didn't really understand at first about American culture.

I cannot forget the cubicle on the "other side" where Jeroen and Bob van Eijk were working. I remember the every morning and afternoon getting around in our cubicle for a cup of coffee and some physics talk. Sometimes Marcel Demarteu or Michiel would also join. Bob tried quite often to get me hooked on coffee. He didn't really succeed while he was there. A short time after he and Cristina left

I started brewing myself coffee in the morning. I guess I was missing the nice welcoming smell when arriving at the office.

When thinking about my time at Fermilab I also remember having lunches, movies, parties and playing softball with Ruth, Thomas, Aran and Yiannis. While living in Dorm 2 my life there was made easier by Anne-Fleur, Yunhe and Miguel be it either a small chat or going out in the evenings. During that time I also met Paul Russo, a friend I was always happy to see when returning at Fermilab.

And then it was time to move back to the Netherlands where I shared an office with: Miruna, Caroline, Irene, Eric, Folkert, Melvin. Lunches moved from the Refter, but the group got larger as it became usual to have lunch with people from the theory department: Ronald, Wim,Lisa, Yiannis, Marcel, Gijs, and Thijs.

But it was not all work when coming back to Nijmegen. I have to say that my life was quite full and I was surrounded by friends all the time. At first there were the Friday evening drinks at Pieken or Aesculaaf where it was nice to meet (among others) with Sonja, Andrew, Gleb, Claire and Dan, and Jamie and Heleen. Pieken was the place, if I remember correctly, where I decided to join Andrew, Gleb, Dan and Jamie for Vierdaagse. The event itself was unforgettable (also due to pain), but the most memories I have from all the long training walks together with friends. This way I was fortunate to meet Irene,Maria, Silvia, Eva and Eugene, Peer, Marcel N. and many others. Finally, I want to name here my "new" Romanian friends Andreea, Diana, Georgeta, Luminita, Botond, Mihnea, Adriana and Jasper, Madalina and Dan, Roberta and Nicu. Of course I have to also mention here Kees from Café Allicht where we've spent lots of evenings in a way that can be described only by "gezellig". And then are the friends that, even being far away, were very supportive in all these years: Luca, Raluca, Anna, Silvia, Cristi R., Diana and Ionut, Victor, Doina, Mihaela and Dani.

Last, but not least, I owe a lot to my family without whose support nothing would have been possible.